Scanning Probe Investigations Of Magnetic Thin Films And Nanostructures

by Jonathan Fetting

Reviewers:
Prof. Dr. G. Reiss
Prof. Dr. D. Anselmetti

Department of Physics
University of Bielefeld

October 2012

Declaration

I, Jonathan Fetting, hereby declare that this dissertation has not been submitted as an exercise for a degree at this or any other University. It comprises work performed entirely by myself during the course of my Ph.D. studies at the University of Bielefeld. I was involved in a number of collaborations during that time and where it is appropriate my collaborators are dully acknowledged for their contributions.

—————————
Jonathan Fetting

Abstract

Magnetic thin films and nanostructures, like nanoparticles and molecules, have unique transport properties considering their ability to eject spin polarised currents. In this work, the possibilities to make these properties accessible by means of scanning probe microscopy have been investigated.

In the first part of this thesis magnetic thin films with out-of-plane magnetic anisotropy covered by ultrathin MgO films have been prepared and then investigated with scanning tunneling microscopy, atomic force microscopy and magnetic force microscopy. The investigated Co/Pd and Co/Au multilayer systems showed roughness values between rms: 0.4 nm and rms: 0.8 nm. MFM images showed typical maze domain patterns.

In the second part of this work magnetic molecules have been deposited on MgO covered gold substrates and entities with the size of single molecules could be isolated and AFM images have been taken. A clear phase contrast makes the entities identifiable.

In the third part of this thesis the main focus lies on the measurements of the transport properties of ligand stabilized cobalt nanoparticles deposited on HOPG by means of conducting atomic force microscopy. The current-voltage curves showed gaps corresponding with the band gap of CoO/Co_3O_4 nanostructures.

Contents

METHODOLOGY

RESULTS

Contents

List Of Abbreviations

AES	Auger Electron Spectroscopy
AFM	Atomic Force Microscopy
AGM	Alternating Gradient Magnetometer
Co/CoO/Co_3O_4	Cobalt/Cobalt Monoxide/ Tricobalt Tetraoxide
CoAu	Cobalt Gold (as abbreviation for a multilayer)
C-AFM	Conductive AFM
CoPd	Cobalt Palladium
DSP	Digital Signal Processor
FFT	Fast Fourier Transformation
FPGA	Field Programmable Gate Array
GMR	Giant Magneto Resistance
HOPG	Highly Oriented Pyrolytic Graphite
I-V curves	Current Voltage curves
KFPM	Kelvin Force Probe Microscopy
MFM	Magnetic Force Microscopy
Mg/MgO	Magnesium / Magnesium Oxide
MOKE	Magneto Optical Kerr Effect
SNOM	Scanning Near Field Microscopy
Pd	Palladium
PZT	Lead Zirconate Titanate
RMS	Root Mean Square
Ru	Ruthenium
SEM	Scanning Electron Microscopy
SMM	Single Molecule Magnet
SPM	Scanning Probe Microscopy
STM	Scanning Tunneling Microscopy
TEM	Transmission Electron Microscopy
TMR	Tunneling Magneto Resistance
vdW	van der Waals
XRR	X-Ray Refelction

Contents

Introduction

In this introductory chapter a motivation for the investigation of magnetic thin films and nanoparticles will be given. Additionally this thesis will be outlined.

“Nanotechnology (and nanoscience) is a pervasive technological discipline that allows manufacturers to design the functionality of a product by using the novel dimensional, chemical, material, mechanical and electromagnetic properties found at the nanoscale. As products based on aspects of nanotechnology increasingly enter the commercial marketplace, for example, in sun protection creams or sports equipment, quality control of the manufacturing process is required particularly where product characteristics at the nanoscale are of concern, for example, potential health risks or other performance requirements.”

Quote 1 from Leach, Richard K, Robert Boyd, Theresa Burke, Hans-Ulrich Danzebrink, Kai Dirscherl, Thorsten Dziomba, Mark Gee, et al. “The European nanometrology landscape.” Nanotechnology 22, no. 6 (February 11, 2011).

Traditionally thin films play an important role in nanotechnology and they are already widely used in science and technology. Specially tailored magnetic thin films are used in sensor applications and in spintronic devices (Zutic et al., 2004).
One standard way of preparation of thin films is sputtering: it is fast, reliable and capable of producing high quality films, as needed for e.g. large tunnelling magneto resistances. Recent advances in the field of Tunneling Magneto Resistance and Giant Magneto Resistance (TMR/GMR) sensors (Hayakawa et al., 2006), (Yuasa, 2008) suggest, that sputtered films can already rival the quality of films prepared with molecular beam epitaxy.
The higher speed and the lower cost for high quality thin film production give an opportunity for additional fields of applications, e.g. as substrates for SPM applications as discussed in this work.

Magnetic nanoparticles are another building block for nanotechnology devices and products. A wide variety of possible applications has evolved and is still expanding (Reiss and Hütten, 2005), (Weddemann et al., 2010).
Commercial applications demand analytical methods like Scanning Probe Microscopy (SPM) for quality control and access to the physical properties, like conductivity, surface topology and sticking coefficients. In Figure 1 the lateral and vertical dimensions of different analytical tools are presented.

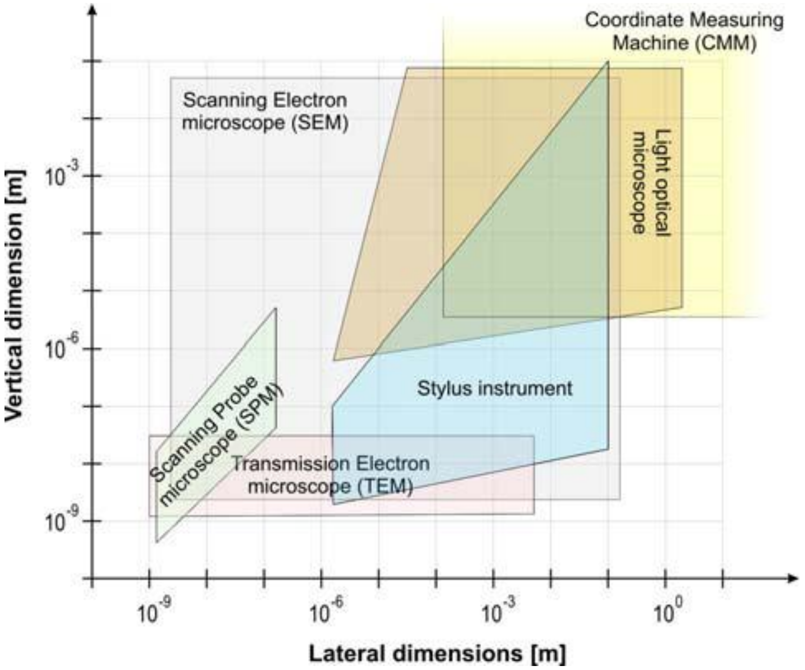

Figure 1 Measurement instruments for dimensional micro and nanometrology. Taken from Hansen, H.N., K. Carneiro, H. Haitjema, and L. De Chiffre. "Dimensional Micro and Nano Metrology." (2006). Used with permission.

As shown in Figure 1 the regime of SPMs is ideal for the investigation of nanoparticles and nanostructures. Speed, stability, accessibility, versatility and usability of SPMs have still potential for improvement and are important properties of SPMs for the future nanometrological tasks in quality control in the next decade (Leach et al., 2011).

SPM has been applied to all the relevant subjects of experimental nanoscience and is an established tool in biology and chemistry. Therefore the choice to apply SPM techniques on magnetic nanostructures and thin films is not unique or special; it is rather an established path for characterisation, which gives access to the nanoscopic properties of a specimen. The ability to have three dimensional information in real time and to manipulate it (the specimen) with e.g. a current at the same time is unique to this technique and opens up a whole new world of possibilities of access to physical properties.
Although there are a lot of commercially available microscopes on the market, the final step from a powerful research tool handled by experts to a standard laboratory inventory with ease of use and access to most of the parameters for SPM is not available – even though there has been a lot of progress recently (e.g. NT-MDT's SOLVER platform (Foster, 2009) or Bruker's Dimension/Innova microscopes).

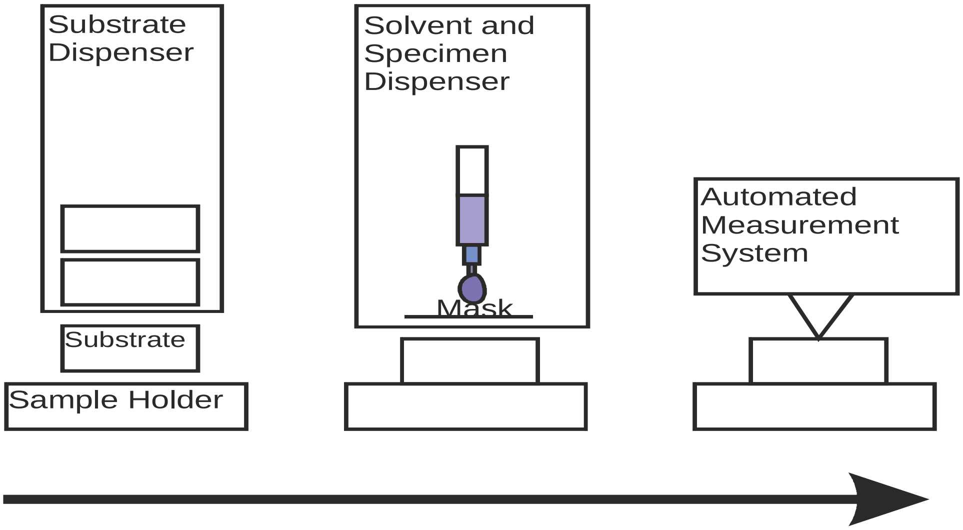

Figure 2 Schematic of an imaginary automated chemical specimen analyser. This work will cover the development of magnetic substrates and the deposition of specimen. Additionally the accessibility of magnetic nanoparticles with SPM is demonstrated in this work.

A SPM tool which operates like a mass spectrometer used in most chemistry and biology laboratories today is still missing: just insert a solvent with the specimen and press start. For such an imaginary machine a choice of substrates and deposition methods should be available. One part is to design the substrates and to test them for their applicability. Another part of this machine would be the deposition of the specimen[1]. A schematic of a possible processing order in such a machine is shown in Figure 2.

While building such a machine is a challenging engineering task, it is from the physicist point of view very interesting to test, if such a machine would be able to provide the desired results. Therefore testing the concepts of using sputtered magnetic substrates for SPM and the access of deposited specimen and their properties on substrates was a fundamental motivation for this thesis.

Additional motivation gave the intriguing idea of having spin polarised substrates with out-of plane configuration at hand, which will not suffer from the Kondo effect (the screening of states of adsorbed molecules by electrons of the metal) due to the MgO coverage.

---

[1] In this work only ex-situ characterisation techniques are discussed. The molecules and particles have also been deposited after film production. Although vacuum might be applied for the drying of the solvent, no in-situ deposition like evaporation, electrospray ionisation are discussed or used.

Chapter 2 and 3 contain the methodology section. Chapter 2 will discuss scanning probe methods and their technological implementations.

In Chapter 3 about thin film production and thin film magnetism a very brief description of the underlying processes will be given. Also in Chapter 3 deposition and self-organisation of specimen will be treated in a short manner in order to cover the observed effects and methods.

In Chapter 4 the obtained results will be presented and discussed. Starting with magnetic multilayers (CoPd, CoAu) covered with ultrathin layers of MgO. The MgO layers will be treated briefly.

MFM, AFM and STM images of the multilayer systems will be presented and their properties will be discussed.

Aging processes of the samples have been investigated with SEM and AFM.

Deposition of single molecules magnets on CoPd multilayer, covered with an ultrathin MgO layer is one topic of the next section. Additionally mask deposition of molecules on substrates using a TEM grid and KPFM measurements on gold covered molecules are presented.

The next section deals with deposited cobalt nanoparticles, how they self-organise on Higly Orientated Pyrolitic Graphite (HOPG). AFM images and SEM images are shown.

The following section will treat electric transport through cobalt nanoparticles on HOPG measured with C-AFM. Current maps, which were simultaneously acquired with the topography and I-V curves applied on HOPG, clusters and single particles are presented. The behaviour of the curves is compared with known properties of cobalt nanostructures and a possible explanation of the observed curves and maps is discussed. Finally some KFPM images of HOPG and nanoparticles on HOPG are shown.

In the last chapter a summary and an outlook on further studies and applications is given.

Finally there is the literature section and the appendix.

METHODOLOGY

General Approach To Scanning Probe Microscopy

In this section I will describe briefly the basics of scanning probe methods used in this work. I will start with a section where the general approach to scanning probe methods is described and will go on with the realisation in hard and software. The end of this chapter will explain the flavours used in this work: STM, AFM, MFM, C-AFM and KFPM. The description of these concepts is inspired by the books of (Wiesendanger, 1995), (Chen, 2007), (Mironov, 2004) *and* (Foster and Hofer, 2006). *Some additionally information has been derived from* (Hartmann, 1999) *and* (Melitz et al., 2011).

Scanning Probe Microscopy is based on the fundamental concept of a local probe brought in contact with a specimen under investigation. The contact is defined by the interaction chosen for the measurement, e.g. a chemical interaction, an electric interaction or a magnetic interaction. Technical requirements for a local probe instrument have been stated by H. Rohrer:

1. Strong distance dependency
2. Close proximity of probe and object
3. Very sharp probe tip (small diameter)
4. Stable positioning device

In addition one might add that the environment where the local probe is applied is of importance, too. Generally there can be distinguished between ambient conditions, a controlled gaseous environment, liquid cells and vacuum. Another significant role plays the temperature.

The interactions of the local probe with the specimen under test can be due to, e.g. forces or electron transport. Furthermore some properties can be probed directly, e.g. with a scanning squid microscopy, a scanning hall probe microscopy, scanning thermal microscopy and SNOM. A lot of combined methods have also evolved, e.g. tip enhanced Raman spectroscopy, FRET combined with AFM and nanomanipulation, nanolithography with dip-pen method and/or nanocapillary in the tip, SEM and AFM combined, and many more.

Physical interactions are dynamic processes or quasi static processes, depending on the time scale and the probe should be chosen with respect to the interaction probed.

Forces occurring in Scanning Probe Microscopy

A local probe brought close to a specimen will experience forces originated by electronic and atomic interactions. These forces can be classified by the range of their interactions and by their origins. In the Appendix a list of force interactions and their main features are tabulated (after (Israelachvili, 2011)). For convenience the forces are divided into macroscopic and microscopic forces. For this work relevant are macroscopic forces, because the measurements have been performed under ambient conditions, where chemical contrasts are hard to obtain.

Macroscopic forces

Van der Waals force

The van der Waals (vdW) force is caused by the electromagnetic interaction of dipoles between probe and sample and is composed of three main components: the dispersion force (or London force), the induction force (or Debye force) and the orientation force (or Keesome force).

The vdW force is mostly attractive and small changes in the distance between probe and sample will cause forces in the range of several nN. The vdW force is not very dependent of the chemical composition of the probe - it can be treated as a long range interaction. As it is most of the time exceeding the chemical forces, it is in many cases the dominating force interaction. For correct calculations all atomic interactions would have to be included. As this is not possible an approximation must be made. Assuming a known potential (V($\mathbf{r}$)) between two atoms with the distance $\mathbf{r}$ separating them, the force can be written:

$$F(r) = -\nabla \cdot V(r)$$

The potential is

$$V(r) = -\frac{C_6}{r^6}$$

where C_6 is a material specific constant. Following the hypothesis of Hamaker the total force between two macroscopic bodies can be calculated through the following integration:

$$F_{vdW} = \rho_1 \rho_2 \int_{v_2} \int_{v_1} F(r) dV_1 dV_2$$

where ρ_1 and ρ_2 are the number densities[2] and V_1 and V_2 are the volumes of bodies 1 and 2 respectively. The constant introduced by Hamaker for the general interaction between two bodies is

$$H = \pi^2 \, C_6 \rho_1 \rho_2$$

It characterizes the resonance interactions between electronic orbitals of two particles.

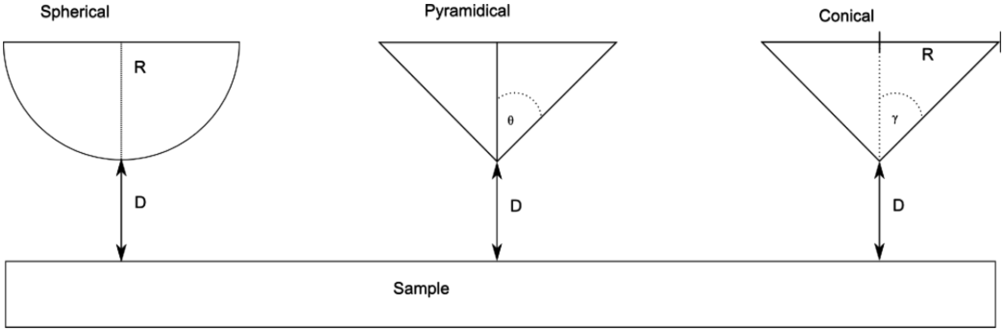

The vdW force is a function of distance for a given tip shape. Three characteristic tip shapes are considered here (for more information see (Israelachvili, 2011)). For a sphere with radius R in a distance D the force is given as:

$$F(D) = -\frac{2HR^3}{3D^2(D+2R)^2}$$

for a pyramidal tip the force is

$$F(D) = -2\,H \frac{\tan^2\theta}{3\pi D}$$

with θ as angle between the rotational axis and the edge of the pyramid. For a conical tip of angle γ and radius R the force equals:

$$F(D) = \frac{HR^2\,(1-\sin\gamma)(R\sin\gamma - D\sin\gamma - R - D)}{6D^2(R+D-R\sin\gamma)^2} - \frac{H\tan\gamma(D\sin\gamma + R\sin\gamma + R\cos 2\gamma)}{6\cos\gamma\,(D+R-R\,\sin\gamma)^2}$$

---

[2] Hamakers Ansatz for Van der Waals interactions between two bodies assumes a continuous medium where each atom occupies a volume dV with a number density ρ.

If the atoms are far enough apart, the time for the electric field to reach the atom can be greater than the period of the dipole interactions. This retardation effect will cause repulsive interaction and a change in the distance dependence.

Image forces

The interaction of a conducting local probe due to polarization by charged atoms of the sample is called image force. Image forces caused by charge distribution are a standard problem in classical electrostatics and calculations can be found in every standard book about electrodynamics e.g.(Jackson, 1998). The image forces introduce an additional energy U_{el} to the system. This energy can then be added to calculations for the total tip-surface force.

Capacitance Force

If two different conducting materials with different work functions are in contact and electron flow is allowed, there will be a contact potential. Although the image force includes the capacitance force, it is still useful to calculate an analytical approximation for macroscopic systems. The electrostatic energy produced by difference of the surface potential of two materials reads:

$$E_{elec} = \frac{1}{2} C U^2(x,y)$$

where C is the probe-sample capacitance and U(x,y) the potential difference. Differentiation with respect to z gives the capacitance force:

$$F(x,y,z) = \frac{1}{2}\frac{dC}{dZ} U^2\,(x,y)$$

In order to evaluate this expression, it is necessary to find a physical expression for C(z) for a real probe shape. With an approximate analytical approach that gives the capacitance of an axisymmetric probe, one obtains:

$$C(z) = \frac{1}{U}\int_{probe} 2\pi \rho_s'\,(z')\sigma_s(z')dz'$$

where ρ_S is the analytical surface equation of the probe and σ_S is the surface charge density. A given spherical shape with radius R would therefore result in:

$$F_c = -\frac{\epsilon\epsilon_0 R U^2}{z}$$

The relevance of this force is crucially dependent on the probe and surface properties and also on the experimental setup. Because only if there is a significant potential difference between the probe and the surface, the capacitance force is an important contribution to the interactions.

Work function anisotropies:

If the surface is rough or has an inhomogeneous work function distribution, the above calculations are not exact anymore and must be modified. Unfortunately there is no analytical way to do this, because some of the needed parameters are unknown. In order to take those effects into account the charge density can be modified and the applied bias in the calculations can be adjusted.

Forces due to probe and surface charging

There are several mechanisms which cause charging effects, e.g. cleaving, sputtering, tribocharging. Charging effects usually occur on insulator surfaces, e.g. on freshly cleaved MgO surfaces or MICA surfaces. The range of this interaction is limited due to the exponential[3] decay of the charge-charge interaction for a neutral surface, where all the charged defects are compensated without atomic displacement. If the charges form dipoles, the dipole interactions have a longer range and can introduce electrostatic contributions to the force.

Magnetic forces

If the probe and the sample are ferromagnets, magnetic forces between them will occur. Therefore a magnetostatic coupling between sample and probe exists. For simplicity a probe in needle form consisting of a ferromagnetic material is assumed. The tip is therefore modeled as a homogeneously magnetized prolate spheroid of suitable dimension. External stray fields of the sample are neglected. Therefore the problem can be treated as a purely magnetostatic one. The potential for any ferromagnetic sample becomes:

---

[3] Assuming e.g. a Buckingham type potential.

$$\phi_S(\boldsymbol{r}) = \frac{1}{4\pi}\left[\int \frac{d^2\boldsymbol{s}'\boldsymbol{M}_s(\boldsymbol{r}')}{|\boldsymbol{r}-\boldsymbol{r}'|} - \int d^3\boldsymbol{r}'\,\frac{\boldsymbol{\nabla}\cdot\boldsymbol{M}_s(\boldsymbol{r}')}{(|\boldsymbol{r}-\boldsymbol{r}'|)}\right]$$

where $\mathbf{M}_s(\mathbf{r}')$ is the sample magnetization vector field and $\mathbf{s}'$ an outward normal vector from the sample surface. The first integral takes the surface magnetic charges into consideration, which are created by magnetization components perpendicular to the surface. Volume magnetic charges from interior divergences of the magnetization vector field are covered by the three dimensional integral. Therefore the stray field is:

$$H_S = -\nabla\cdot\phi_S(\boldsymbol{r})$$

and the magnetostatic energy reads:

$$E(\boldsymbol{r}) = \mu_0\left(\int d^2\boldsymbol{s}'\cdot\boldsymbol{M}_p(\boldsymbol{r}')\phi_S(\boldsymbol{r}') + \int d^3\boldsymbol{r}'\nabla_{r'}\cdot[\phi_S(\boldsymbol{r}')\boldsymbol{M}_p(\boldsymbol{r}')]\right)$$

$\mathbf{M}_p(\mathbf{r}')$ is the magnetization vectorfield of the probe. The force is then:

$$\boldsymbol{F}(\boldsymbol{r}) = -\nabla E(\boldsymbol{r})$$

In the point probe approximation a multipole expansion of E(**r**) gives monopole and dipole moments, which are projected into a fictious probe of infinitesimal size that is located a certain distance away from the sample surface. With this approximation the force acting on the probe, immersed into the near surface sample microfield, is:

$$\boldsymbol{F} = \mu_0(q + \boldsymbol{m}\cdot\boldsymbol{\nabla})\boldsymbol{H}$$

with q and m as monopole and dipole moments.

Capillary forces

Under ambient conditions atmospheric humidity plays an important role for the interactions between the probe and the sample surface. A certain discontinuous behavior in the interaction between probe and sample might occur. For example, the liquid layers will “jump into contact”, and form a meniscus with a large radius between them and probe, and until “hard contact” is reached, this liquid layer will be compressed. Removing the probe will cause the meniscus to stretch until it breaks.

Microscopic forces

Chemical forces dominate the microscopic interactions and are usually much weaker than the macroscopic forces. The forces basically originate in the interaction between nuclei and electrons in the system. A simple classification (Foster & Hofer, 2006) results in:

- *Electrostatic forces:* Coulomb interaction between ions in the tip and sample.
For an ionic surface and an ionic tip the electrostatic force between ions will dominate the microscopic forces in most cases.

- *Polarization forces:* polarization of an electron-cloud by ions.
This is especially relevant for conducting materials, which are highly polarizable, interacting with insulating materials.

- *Van der Waals forces:* the microscopic version of the force discussed in the previous section, generally much weaker than the other forces at this scale, but important in imaging of inert surfaces like Xenon or in considering the physisorption of inert species on surfaces.

- *Chemical bonding:* in the case that the system's materials cannot be approximated as ideally ionic or inert, it becomes important to take chemical bonds into account, which may form between the tip and surface. This is especially important for the consideration of the interactions between reactive tips and surfaces, where the need to saturate dangling bonds results in strong tip–surface bonds and correspondingly large microscopic forces.

- *Magnetic forces:* on the microscopic scale, magnetic forces represent the exchange force between atomic spins in the tip and surface. For a spin polarized tip scanning a magnetic surface, the exchange force will vary according to the spin–state of the atom under the tip.

Electron transport theory in tunneling microscopy

Whenever two conducting electrodes are separated by a small enough potential barrier, electrons will tunnel from one electrode to the other. The transfer-Hamiltonian approach of Bardeen states that the tunneling current I is a measure of the overlap in the separating gap of the wave functions of the two electrodes. In this picture, the current is a function of the separation and of the nature of the electron states involved. A very common tunneling configuration is a conductor-isolator-conductor planar film stack. Following Simmons, one can write the current density at small voltages $V \ll \Phi$ as

$$j = \left(\frac{e^2}{\hbar}\right)\left(\frac{\kappa_0}{4\pi^2 s}\right) \cdot V \cdot \exp(-2\kappa_0 s)$$

with s as effective tunnel distance in Å, κ_0 the inverse decay length of the wave function density outside the surface, V the applied voltage in V, and

$$\kappa_0 = 1.025\sqrt{\Phi(eV)}$$

with Φ as effective barrier height. For an intermediate bias voltage range the current density becomes:

$$j = \frac{e}{4p^2 s^2 \hbar}\left(\left(\phi_0 - \frac{eU}{2}\right)\exp\left[-\frac{2(2m)^{\frac{1}{2}}}{\hbar}\left(\Phi_0 - \frac{eU}{2}\right)^{\frac{1}{2}} * s\right] - \left(\Phi_0 + \frac{eU}{2}\right)\exp\left[-\frac{2(2m)^{\frac{1}{2}}}{\hbar}\left(\phi_0 + \frac{eU}{2}\right)^{\frac{1}{2}} * s\right]\right)$$

High voltage ranges result in the following current density:

$$j = \frac{2.2e^3F^2}{16p^2\hbar\Phi_0}\left\{exp\left[-\frac{4}{2.96\hbar eF}(2m)^{\frac{1}{2}}\Phi^{\frac{3}{2}}\right] - \left(1 + \frac{2eU}{\Phi_0}\right)exp\left[-\frac{4}{2.96\hbar eF}(2m)^{\frac{1}{2}}\Phi^{\frac{3}{2}}\left(1 + \frac{2eU}{\Phi_0}\right)^{\frac{1}{2}}\right]\right\}$$

with F=U/s.

A difference in the work functions of the electrode material leads to an asymmetric potential barrier and the I-V curve becomes polarity dependent.

Simmons also stated that the classic image potential can be approximated by:

$$V_i(z) = -\frac{2.3(\ln(2))e^2}{16\pi\epsilon_0 d} \cdot \left[\frac{z}{d}\left(1 - \frac{z}{d}\right)\right]^{-1}$$

The image potential leads to rounded edges in a rectangular barrier; the thickness of the barrier is reduced and the current flow between the two electrodes is increased. As this approximation does not take quantum mechanics into account, it does have some severe limitations which are discussed in (Wiesendanger, 1995).

Realisation In Hardware And Software

This section deals with the realisation of SPM systems. It will cover the technical aspects and introduces literature for further information. In this work a modified Bruker Nanoscope III controller based multimode microscope was used. For the STM measurements the SECPM addition with universal bipotentiostat has been connected.

In Scanning Probe Microscopy the physical process, that is measured, are the interactions between the probe and the surface, or an interaction "guided" by the probe, e. g. evanescent light waves in SNOM.

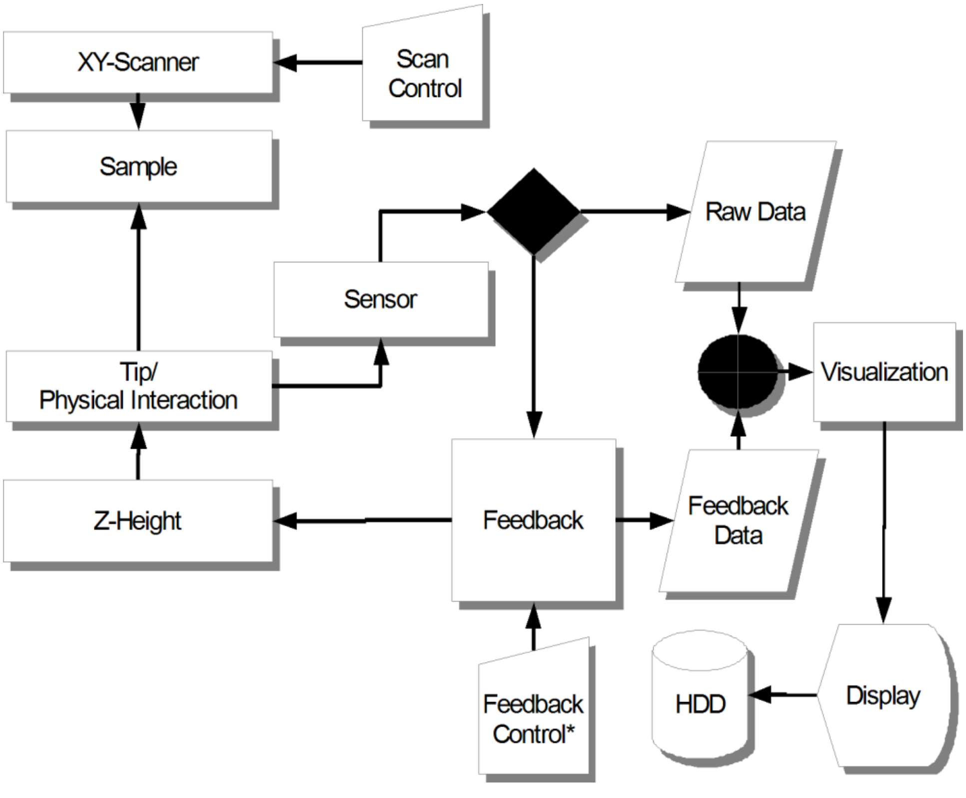

Figure 3 Flowchart of a general simple SPM setup. The feedback data is usually the drive signal of the PID controller. The visualization process describes the mathematical operations on the data in order to make the physical interactions visible. (*) The feedback control can be automatic.

In Figure 3 the general setup of a simple SPM is presented as a flow chart. The shown setup is an open loop system, in order to keep the presentation simple. Systems with sensors for the actuators and with feedback controlled xy-scanners and z-heights are called closed loop systems; they are capable of correcting drift and creep problems of the piezos, used for sample and tip positioning.

The working principle of a simple scanning probe microscope can be described as a probe brought locally in “contact” with the sample, where it is interacting with the surface. The interaction is measured by a sensor. The feedback loop regulates the z-height in order to keep the output of the sensor on a user specified value. The drive signal of the feedback loop is the generated feedback data. During the visualization process of the measured data, the feedback data is processed and/or the raw data and afterwards displayed and saved. The xy-scanner moves to the next position and the process starts over.

Piezoelectric Materials

In order to get a lateral atomic resolution the xy-scanner needs to have subnanometer resolution, which can be achieved with piezo electric materials[4]. This material class has been discovered by Pierre and Jaques Curie in the late 19th century and its applications started in the 20’s of the 20th century. The Heckmann diagram, first developed in 1925, gives an instructive schematic representation of couplings between elastic, electric, and thermal variables. A recent version of the diagram is shown in Figure 4. Following the thermodynamics of an elastic dielectric, one gets linear constitutive equations. Those define the relations of the material dependent coefficients, which are represented by the lines in Figure 4.

In order to keep the description simple the interested reader is recommended to read (Tichý et al., 2010) for further information about the single coefficients. For the following section only the piezoelectric coefficient is important. The treatment of piezoelectric materials is only covered as far as it is helpful for the understanding of the basic principles of SPM.

---

[4] There are other ways to achieve a similar high resolution, e.g. micromechanical springs, but piezo transducers remain the main choice of producers of SPM systems. As the scanners used in this work are all piezo based, the other methods will not be discussed here.

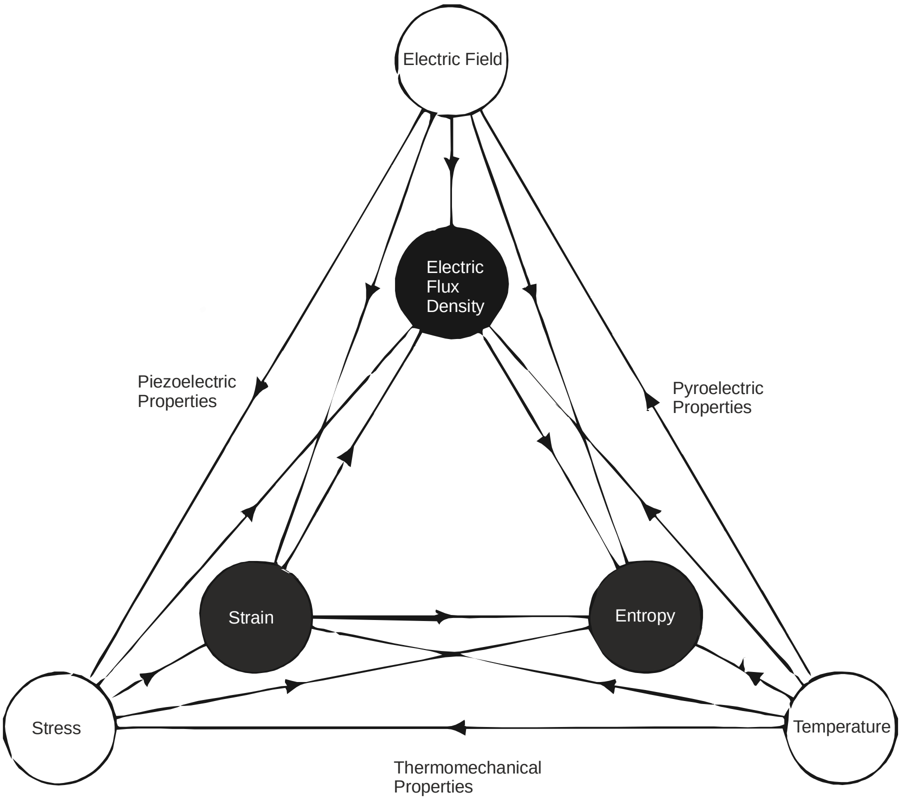

Figure 4 Heckmann's diagram. After J. Tichý, J. Erhart, E. Kittinger, and J. Pívratská, *Fundamentals of Piezoelectric Sensorics,* (2010). Every line represents a variable in the constitutive equations.

A general distinction between direct and converse piezoelectric effect can be made. The direct piezoelectric effect and the converse piezoelectric effect depend on the piezoelectric coefficient d_{111}:

$$P_1 = d_{111} T_{11}$$

for the direct effect, with T_{11} as component of the stress tensor and

$$S_{11} = d_{111} E_1$$

for the converse effect, with S_{11} as strain and E_1 as external field. The converse piezoelectric effect is used for scanning applications. The piezoelectric coefficients are defined as the ratios of the strain components over a component of the applied electrical field intensity $d_{31} = \frac{S_1}{E_3}$.

Typical values for these coefficients found in the literature are $10^{-9} mV^{-1}$ to $10^{-12} mV^{-1}$. The traditional piezo ceramic material used for scanners is lead zirconate titanate ceramics (PZT). The initial produced ceramics do not show the piezoelectric effect, because they are isotropic due to random arrangement of the dipoles. A poling process ensures a permanent electric polarisation. The dipoles are then aligned with the poling field. The poling field is labelled following a convention in the 3 direction (the positive z-direction). Newer piezo ceramics are lead free, but have lower piezo constants. An overview over the relevant parameters for piezoelectrics is given in the Appendix.

Scanner Designs

A general distinction between scanning tip and scanning sample designs can be made. Both design approaches have advantages and disadvantages. While scanning tip based scanner designs are usually more versatile for advanced operations, e.g. low temperature applications, scanning sample based systems are often mechanically more stable.

There are usually two main approaches for achieving the nanometer resolution in scanning probe microscopy: tube piezo based designs and linear actuator based designs. Tube designs have the advantage of having a low drift and stable operation, but they introduce a scanner bow and can exhibit nonlinearities. For closed loop operation linear actuator based designs are preferred, because they are easier to implement and actuators with sensors are commercially available. The scanner used in the Multimode is a sample scanning, open loop tube scanner.

Sensors

Most of the measured physical interactions, disregarding electron tunneling as in use for STM at the moment, cause a displacement of the probe or a shift of the actuating frequency. Detecting sensors need to be able measure small displacements or frequency shifts. As the displacement is usually very small, the sensors signal needs high amplification and therefore a good signal noise ratio must be ensured. In Table 1 is an overview of sensors and their applications in SPM. In Figure 5 the most commonly used detection methods are illustrated.

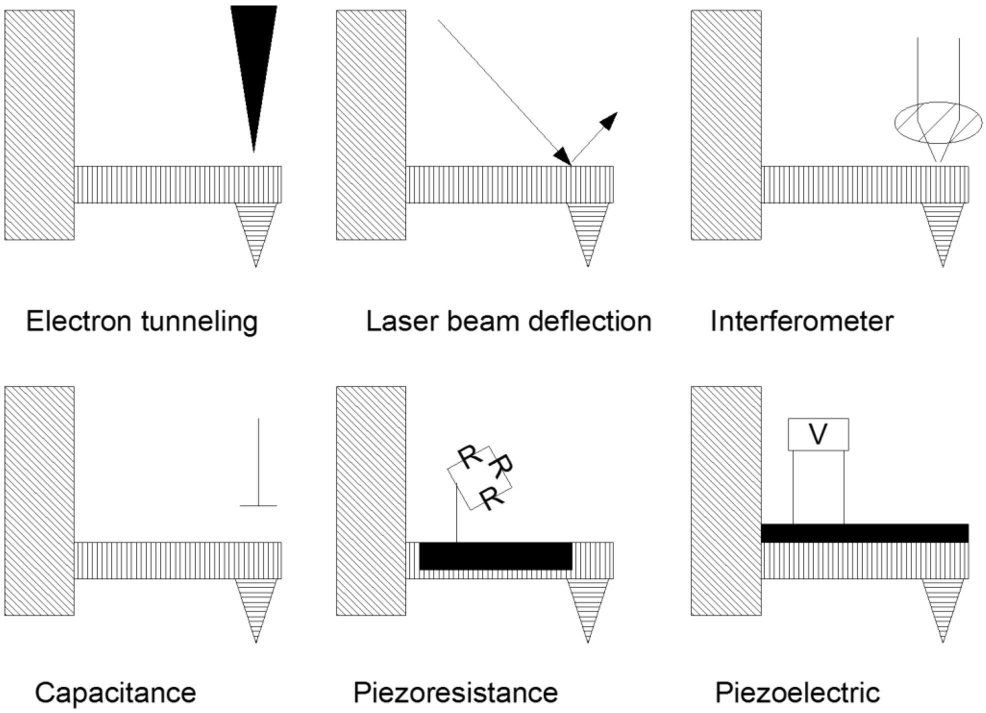

Figure 5 Commonly used sensors for displacement of cantilevers and tips.

Method	Description
Electron tunneling	original concept, potentially highly sensitive, practically problematic
Laser beam deflection	most widely used, robust, high sensitivity, not directly quantitative, requires calibration
Interferometer	best sensitivity, quantitative, uses limited space, complicated
Capacitance	sensor can be microfabricated, strong force from sensor, limited sensitivity
Piezoresistance	ideal for microfabrication & integration, limited sensitivity, heating of cantilever, drift, creep
Piezoelectric	mostly quartz tuning forks, good for true atomic resolution, limited sensitivity

Computer Interfaces

While early designs of scanning probe microscopes could work without any computers, simply displaying the scanned lines on an oscilloscope or being recorded with a XY-recorder, it has become a convenient practice to use a computer for controlling and recording of the measurement. Analysing the measured data with a computer enables to make use of the full arsenal of digital data processing.

Nowadays it is even common to implement the complete feedback control loop(s) in field programmable arrays (Nowak et al., 2011), so that the control processes involved in scanning probe microscopy can be adressed in software in real time. Graphical programming languages like Labview[5] or IHDL (for the R9 controller by RHK) are convenient ways to modify the setup. Software for numerical computations like Matlab/Scilab/Octave gives full analytical access to the data.

Though this is the current state, the usual lab equipment has still an analogue feedback, digitally controlled by a microprocessor and/or DSP, which is connected to a computer. In order to interface with a computer or microprocessor, somewhere in the signal flow an analogue-to-digital conversion has to take place. Usually the drive signal from the feedback loop is converted and is representing the image height signal. Digital-analogue converter are used to control the piezo amplifiers, the scanning process, setpoints for feedback loops, possible bias voltages and/or other equipment that needs to be controlled. Additional inputs can be used to acquire current maps, magnetic force images, electric potential maps, sensor outputs, etc.

---

[5] A case study by the National Taiwan University can be found under cs-14623 on the webpage of National Instruments. (www.ni.com).

Software Realization

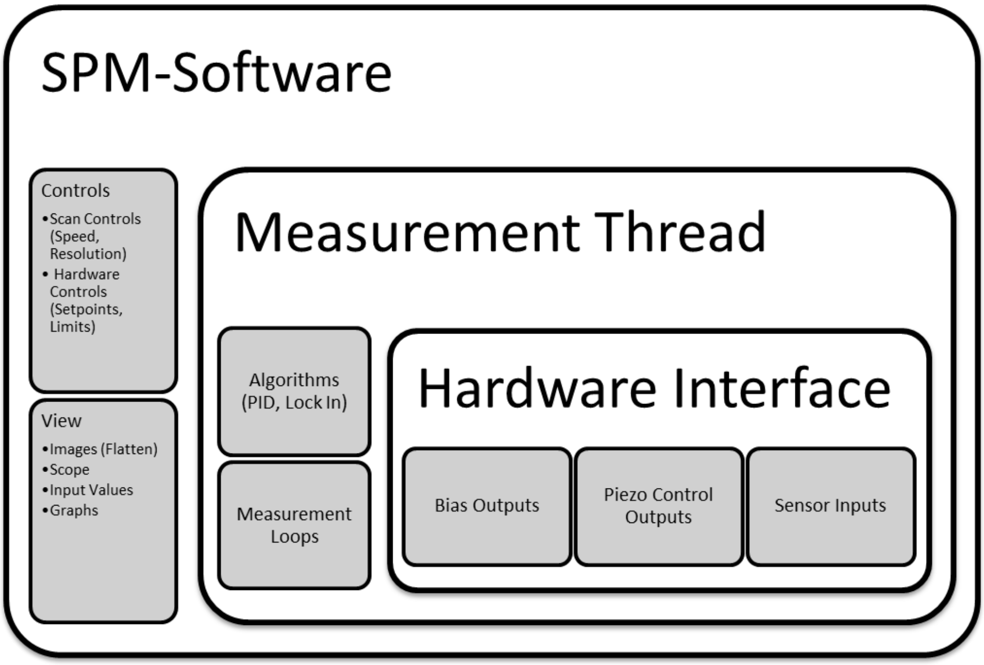

Figure 6 Schematic example diagram of a hierarchical software structure for SPM software.

In Figure 6 a schematic diagram for a hierarchical software structure is presented. It gives an impression of a general structure for the implementation of SPM software. There are some open source implementations of SPM software, e.g. GsXM (Zahl et al., 2010).

Visualization And Data Representation

From a mathematical point of view, an image is just a matrix, a two dimensional array of real numbers v(x,y). Unless the image has infinite resolution, the variables x and y are discrete and can be represented as natural numbers. In a typical SPM image the lateral resolution is given by the size of the scan area, divided through the numbers of measurement points, e.g. a 100 nm x 100 nm image with 256 x 256 points gives a theoretical lateral resolution of 0.4 nm. The real lateral resolution will be depending on the measured physical property, the probe geometry and the instrument stability. Heights in SPM images represent the measured physical interaction, in STM experiments to obtain the topography this is usually the drive signal from the constant current feedback loop implementation.

Image processing

As all SPM images can be seen as two dimensional discrete matrices, the methods of numerical computation apply. Data treatment can therefore be done by standard mathematical methods:
By means of programming (e.g. in Python, C, etc.) or with specialized programs like Matlab (Octave), Igor or Origin the data can be analysed, modified and displayed. But it is usually more convenient to use specialized programs which have the most common processes and analysis functions preprogrammed, e.g. SPIP (commercial), Gwyddion (free) (Nečas and Klapetek, 2011), ImageJ (free) (Abramoff, M.D., Magalhaes, P.J., Ram, 2004), WSxM (citeware) (Horcas et al., 2007) and for Bruker (Veeco, Digital Instruments, Thermoscope) AFMs there is Nanoscope Analysis (free).

Common processes and analysis functions are listed and explained in the Appendix. Additional information on the mathematical and methodical approaches can be found in The Image Processing Handbook by (Russ, 2011).

In this thesis several versions of WSxM are used for all image representations. For the access of additional image data the Nanoscope Analysis 1.40 software and the Nanoscope 5.31/6.13[6] software have been used. For grain analysis Gwyddion 2.25 has been used. Whenever necessary the image data and metadata in the header have been directly accessed with editors or homemade software.

---

[6] The Nanoscope 5.31/6.13 software has been used to acquire the images, as discussed in the Appendix.

Scanning Tunneling Microscopy

Scanning tunnelling microscopy was invented by Binnig and Rohrer (1982) and uses electron tunnelling as physical interaction between probe and sample. The probes are usually metal electrodes and the samples need to have certain conductivity. The tunnelling current is converted by a current to voltage circuit to a voltage, which is compared with a reference value. The output voltage V_{out} of a current to voltage converter is defined as:
$V_{out} = R_{Gain} \cdot I$, where R_{Gain} is usually between 1 MΩ and 10 GΩ.
The difference between measured I and the setpoint I_{set} is then amplified to drive the z piezo.
Two major modes exist besides a dynamic mode, a constant current mode and a constant height mode. In Figure 7 these modes are demonstrated with the tip on three positions on a sample.

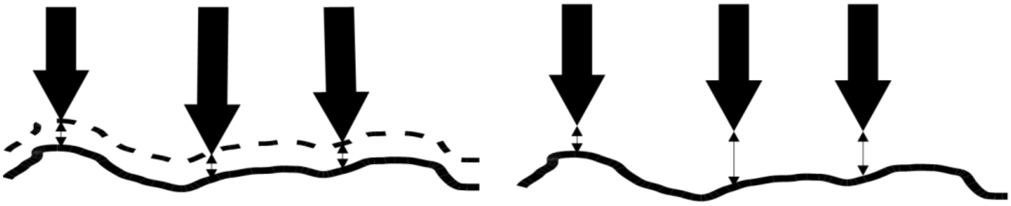

Figure 7 Constant current (left) and constant height mode (right). A tip is shown on three positions. The dashed line implicates the measured topography. The small arrows implicate with their length the current flow between tip and surface.

Dynamic modes are rather rare but can extract additional information about the sample material, like dielectric properties.
The constant current mode uses the feedback loop to regulate the current on every measurement point to a constant reference value. The error signal from the feedback can then be used to display the topography, if one considers the corrugation of a homogeneous material.
The constant height mode measures the current changes if a constant z height is adjusted. This mode only works on flat surfaces. Advantages are that one can see material differences - the disadvantages are the risk to crash, if there are height changes and z drift (e.g. in open loop systems) the tip can easily crash.

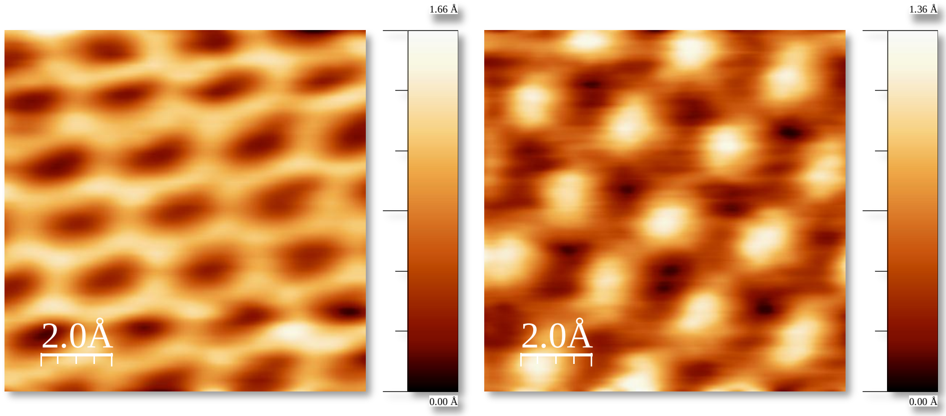

Figure 8 Atomic resolution on HOPG under ambient conditions showing the honeycomb lattice (left) and the triangular lattice (Bernal stacked graphite)(right).

Scanning tunnelling spectroscopy

In scanning tunnelling spectroscopy a voltage is ramped and the current is measured. This can be done at every pixel of an image (CITS), over the complete range of the image (slowly/fast modulated), at one point in the middle of the image or aimed somewhere on a desired spot – depending on the implementation of the measurement setup. The used measurement setup in this work only allowed taking an I-V curve in the middle of the image.
Taking a dI-dV curve probes the local density of states of the sample and can also contain states of the tip. For more detailed information about STS I recommend the already mentioned literature.

Tip considerations

STM tips can be produced by etching or mechanical shearing. The tips used in this work have been platin-iridium tips, which have been mechanically cut. Platin-iridium tips are very stable in ambient conditions and therefore are a preferable choice for measurements under those conditions and are known to produce atomic resolution (as demonstrated in Figure 8).

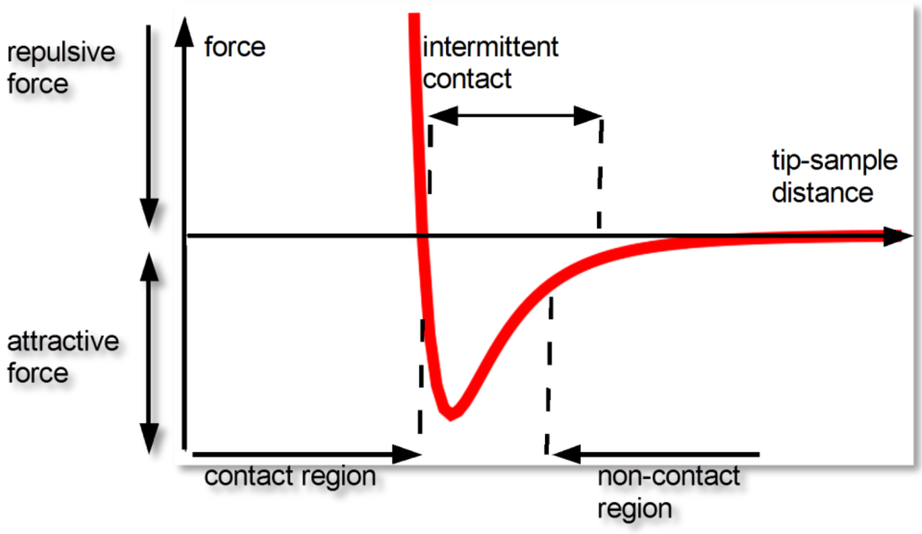

Figure 9 The potential regions which define what kind of contact between tip and sample is established for the different AFM modes. For dynamic mode measurements the intermittent contact region and the non-contact region are utilised.

Atomic Force Microscopy

The atomic force microscope was invented 1986 by (Binnig and Quate, 1986). In standard atomic force microscopy there can be distinguished between contact modes, where a constant force is applied and held constant, and dynamic modes (García, 2002) where damping or phase shift/frequency shift are held constant. The dynamic modes can be classified in non-contact and in tapping mode. In Figure 9 the different potential regimes are presented.

Contact Mode

In contact mode the tip scans the sample in close contact with the surface, which means that the force on the tip is repulsive in range of several nN. In contact mode AFM the deflection of the cantilever is sensed with a four quadrant diode and compared in a feedback amplifier to a reference value. If the measured deflection is different from a reference value a voltage is applied to the piezo to raise or lower the sample relative to the cantilever until the difference to the reference value is nullified. The drive signal is displayed as a function of the lateral position of the sample.

Non-contact Mode

In non-contact mode, invented in 1987 (Martin et al., 1987), the tip oscillates close to its resonant frequency 1 - 10 nm above the sample surface, actuated by a piezo oscillator. AC detection methods can be used to detect the small forces between the tip and the sample by measuring the change in amplitude, phase, or frequency of the oscillating cantilever in response to force gradients from the sample.

Tapping Mode

Tapping mode (TM) imaging is implemented by oscillating a cantilever assembly at or near the cantilever's resonant frequency. The piezo motion causes the cantilever to oscillate with a high amplitude (typically greater than 20 nm) when the tip is not in contact with the surface. The oscillating tip is then moved toward the surface until it begins to tap on the surface. The vertically oscillating tip alternately contacts the surface and lifts off, generally at a frequency of 50 to 500 kHz. As the oscillating cantilever begins to intermittently contact the surface, the cantilever oscillation is reduced due to energy loss caused by the tip contacting the surface. The cantilever oscillation amplitude is maintained constant by a feedback loop and the drive signal is the presented image height information. The digital feedback loop adjusts the tip-sample separation to maintain constant amplitude and force on the sample. The phase image can be used to identify material properties (Schmitz et al., 1997).

MFM

Magnetic force microscopy (MFM) is usually done in a dynamic mode on a magnetic sample, using a magnetic cantilever. In Figure 10 the original description of the AFM producer is presented. It is outlined that the magnetic force gradient causes a phase shift while scanning the tip above different domains during the LiftMode scan. In this thesis MFM has been used to clarify the out-of-plane domain structure of the used substrates. Figure 11 shows a MFM image of a recording tape. On the left image the simultaneously measured topography is shown and the right image shows the magnetic structure of the tape.

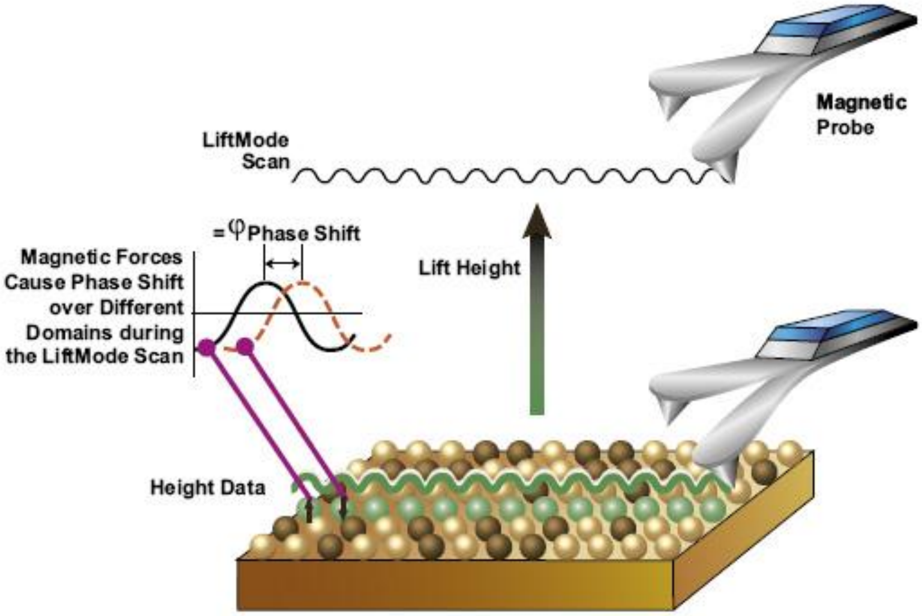

Figure 10 A multimode system from Bruker was used during this thesis. MFM as it is explained by Bruker: "Magnetic Force Microscopy (MFM) uses a combination of TappingMode™, LiftMode™ and a properly prepared tip to gather information about the magnetic held above a sample. Each line of the sample is first scanned in TappingMode operation to obtain the sample topography. The topographic information is stored and retraced with a user selectable height offset in LiftMode, during which the magnetic data are collected. Typical lift heights in MFM range from 20-100 nm." The image is courtesy of the manufacturer.

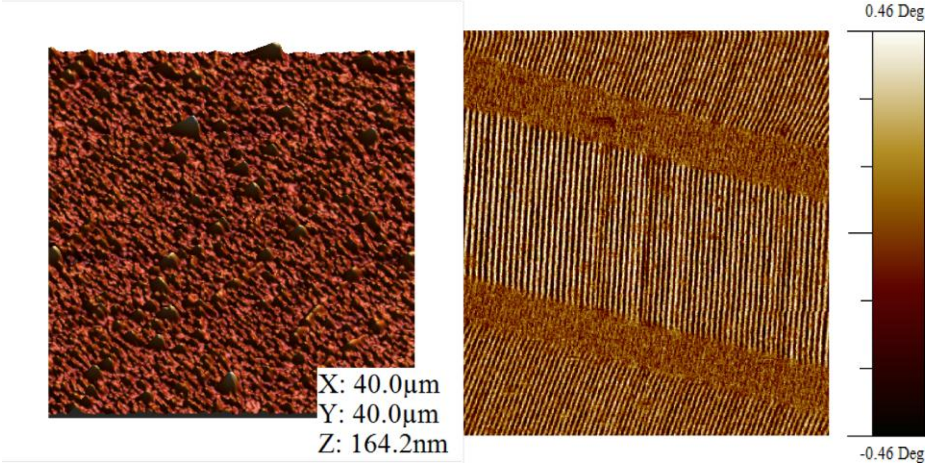

Figure 11 MFM measurement of a magnetic recording tape. The left picture shows the simultaneously measured topography in a three dimensional representation. The right picture shows the magnetic structure of the tape.

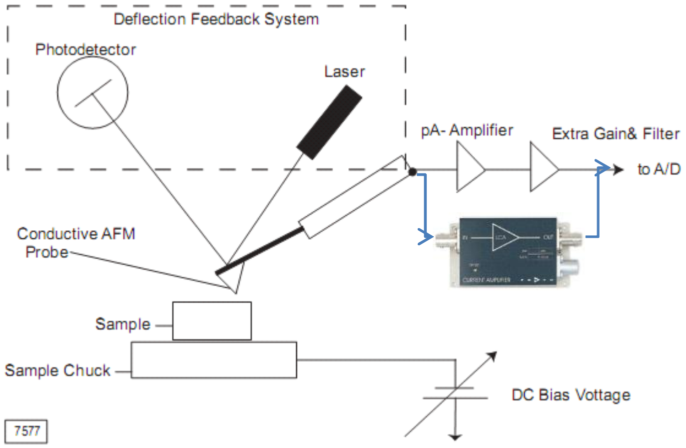

Figure 12 Schematic of the modified C-AFM setup used in this work. A *Femto* (LCA-1K-5G) current to voltage converter with a fixed gain of 5 x 10^9 V/A has been used for the current conversion.

C-AFM

Conducting atomic force microscopy (C-AFM) is done in contact mode with a conducting cantilever. Usually normal contact mode operation is performed, a deflection setpoint set and the feedback adjusted to keep the force constant.
Additionally to the topography the current between tip and sample is recorded, which results in a current map of the surface. Therefore interesting conducting regions can be spatially resolved on the topography and vice versa.

Current-voltage (I-V) characteristics can be acquired at fixed points on the surface by applying a voltage between the AFM tip and a fixed counter electrode, and measuring the resulting current between the electrodes. Depending on the system under study, the measured currents can range from pico-Amperes to hundreds of nano-Amperes.

A *Femto* amplifier with a range of 4 nA has been added to the microscope in order to sense currents between tip and sample. The output of the amplifier was connected with an auxiliary ADC input of the Nanoscope III electronics. In the software this input has been assigned to record the current simultaneously with the topography, which results in a current map of the surface.

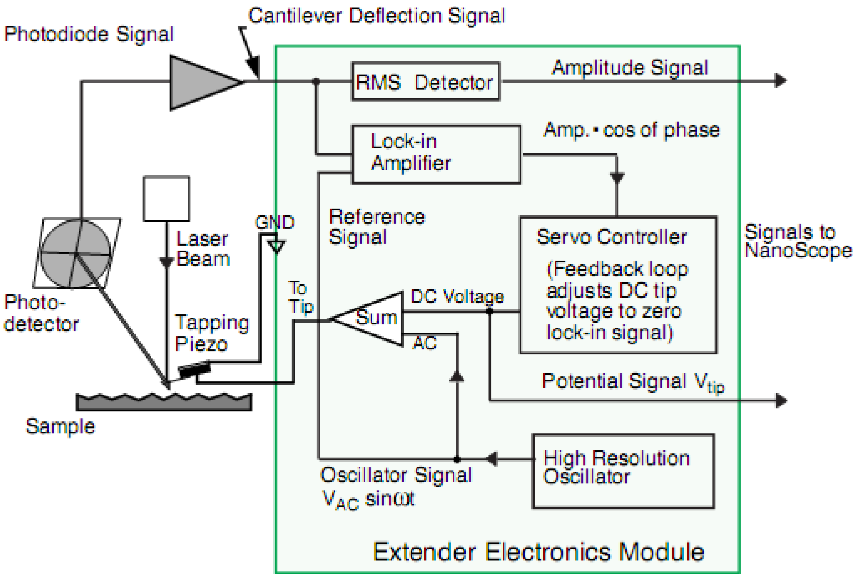

Figure 13 Schematic showing the functional principle of the Kelvin-Probe-Force-Microscopy as implemented in the Multimode AFM. The picture is taken from the manual and is courtesy of Bruker.

Kelvin-Probe-Force-Microscopy

Kelvin-Probe-Force-Microscopy has been invented by (Nonnenmacher et al., 1991). It combines the Kelvin-Probe technique (Kelvin, 1898) with dynamic force microscopy.

KPFM provides the capability to image the local surface potential, the contact potential difference of a sample with high spatial resolution. It minimizes the electrostatic interaction between the tip and the surface. As the amplitude modulated tapping mode represents the direct force between tip and sample, the changes in oscillation frequency of the tip are dependent on the force gradient between tip and sample. The CPD itself is defined as

$$V_{CPD} = \frac{\Phi_{Tip} - \Phi_{Sample}}{-e}$$

where Φ_{Tip} and Φ_{Sample} are the work functions of the sample and tip, and e is the electronic charge.

Starting from the energy in a parallel plate capacitor

$$U = \frac{1}{2} C (\Delta V)^2$$

with C as the local capacitance between the AFM tip and the sample; ΔV as the voltage difference between the two, the force on the tip is the rate of change of the energy with separation distance:

$$F = -\frac{dU}{dZ} = -\frac{1}{2}\frac{dC}{dZ}(\Delta V)^2$$

Using an AC voltage and a DC voltage on the tip generates a AC and DC component of ΔV:

$$\Delta V = \Delta V_{DC} + V_{AC} \sin(\omega t)$$

ΔV_{DC} includes applied DC voltages, work function differences, surface charge effects, etc. The force can then be written as:

$$F = \frac{1}{2}\frac{dC}{dZ}\left(\Delta V_{DC}^2 - \frac{1}{2}\, V_{AC}^2\right) - \frac{dC}{dZ}\Delta V_{DC} V_{AC} \sin(\omega t) + \frac{1}{4}\frac{dC}{dZ} V_{AC}^2 \cos(2\omega t + 2\varphi)$$

This formula has a DC term, an omega term and a two omega term.

A sinusoidal driving force is caused by the oscillating electric force with the frequency omega. The cantilever itself is only excited by forces near or at it resonance frequency and therefore the DC and the two omega term do not cause significant oscillation of the cantilever.

Through the electric force motion in z-direction can be excited in the cantilever. The cantilever response is directly proportional to the amplitude of the F_{omega} drive term:

$$amplitude\ of\ F_\omega = \frac{dC}{dZ}\Delta V_{DC} V_{AC}$$

The scanning process is a two pass method. In the first pass the topography is measured and in the second pass the tip moved in an adjustable height over the surface. During the second pass the AC[7] voltage is applied to the tip and the local electrical fields excite the cantilever. The surface potential feedback loop is adjusting the voltage on the tip until it equals the voltage of the sample ($\Delta V_{DC} = 0$), where the cantilever amplitude should be zero ($F_{omega} = 0$). In order to get absolute numbers, the tip must be calibrated. As the tip calibration under ambient conditions is difficult, measurements presented in this work will only be showing work function differences instead of absolute numbers.

---

[7] Plus an additional small default DC voltage.

Cantilever choice and characteristics

For all AFM methods the choice of the cantilever is important.
The standard used cantilever in this thesis is the Olympic OMCL-AC 240 series:

Tip shape : sharpened tetrahedral (tilted)
Tip height : 15 µm (9 to 19 µm)
Tip radius : smaller than 10 nm (7 nm (typ.))
Tip angle : less than 35 degrees
Tip material : single crystal silicon (semiconductor, N type, 4 - 6 ohm*cm)

The typical mechanical properties of the cantilever are:

Thickness(um)	Length(um)	Width(um)	Spring constant (N/m)	Resonacne frequency (kHz)
2.8	240	30	1.8 (0.7 - 3.8)	70 (50 - 90)

For MFM imaging homemade and commercially available tips have been used. The homemade tips had a CoCr coating of 60 nm and had a resonance frequency around 250 kHz.
For C-AFM and Kelvin-Probe imaging commercially available Pt coated tips with a minimum tip apex of 25 nm and a resonance frequency of 80 kHz have been used.

Tip load and high resolution

The capability of high resolution imaging under ambient conditions depends on the tip load. With careful adjustment of the parameters even atomic resolution in contact mode should be possible (Gan, 2009), if the used setup has the ability to fine tune the parameters as needed. It is therefore mandatory to find the correct parameters for every sample/tip combination in order to achieve high resolution and quality images.

Magnetic Thin Films: Preparation And Magnetism

Preparation of Thin Films

In this section I will discuss the possibilities to deposit material on a substrate via physical vapour deposition. Two methods of deposition, evaporation and sputtering, will be briefly discussed. More information can be found in (Ohring, 2002), (Mattox, 1989, 2003), (Venables et al., 1984) *and in* (Rossnagel et al., 1990).

Physical vapour deposition (PVD) processes are techniques which physically "vaporise" materials and deposit the material on a substrate in a high vacuum. In opposite to chemical vapour deposition, where precursors can be chosen to control deposition, only adhesion and surface diffusion of the adsorbed material on the substrate determine the resulting film structure and thickness. If the substrate is crystalline and flat, defect rate and lattice mismatch between the deposited material and the substrate are important for the film growth and morphology. During an *evaporation* process a material source is heated and the material is then transferred to a substrate in a certain distance, where the film growth process starts. *Sputtering* is a process where atoms are ejected from the source material, which is usually at room temperature, through the impact of gaseous ions of a noble gas, generated in glow discharge plasma. The ejected atoms are transferred to substrate in a certain distance. The processes involved in film growth are depicted in Figure 14.

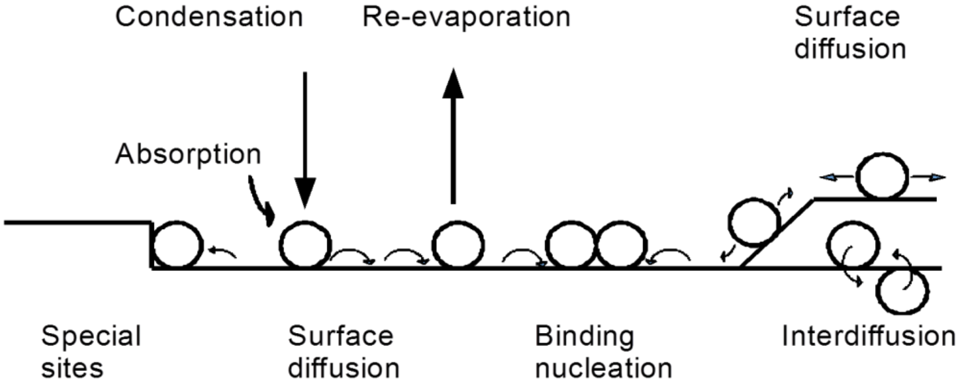

Figure 14 Surface processes as described by (Venables et al., 1984).

During thermal evaporation the temperature of the source material is raised until the material evaporates or sublimes onto the substrate. Often an open boat made of tungsten suspended on a wire is chosen to heat the source material. The evaporated material will be deposited in the whole chamber and therefore evaporation is a messy, inefficient method, which will not produce a uniform deposit. For more uniform films, the substrates ought to be rotated. The deposition rate is related to the source area, to the temperature and to the distance between source and substrate. Quartz oscillators can be used to measure the amount of material deposited. The frequency shift will be proportional to the deposited material and if one calibrates with e.g. X-Ray-Reflectivity to determine the layer thickness of a sample, it is possible to measure in-situ the amount of the deposited material and therefore the expected film thickness.

The favoured method to sputter uniform films is magnetron sputtering. In Figure 15 a schematic of conventional magnetron sputtering is shown. During the ion bombardment of the target, secondary electrons are also emitted from the target and these electrons play an important role in maintaining the plasma. For magnetron sputtering these electrons are constrained in their motion to the vicinity of the target by magnets, which are arranged so that one pole is positioned at the central axis of the target and the second pole is formed by a ring of magnets around the outer edge of the target. The trapped electrons increase the ionization efficiency in the dense plasma in the target region. Therefore increased ion bombardment leads to higher sputter rates and deposition rates. Another advantage of magnetron sputtering is the lower operating pressure.

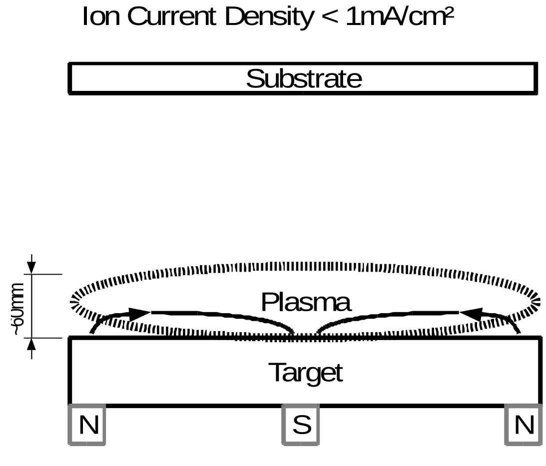

Figure 15 Schematic of conventional magnetron sputtering.

The parameters for magnetron sputtering are the voltage for the plasma, the field strength of the magnets and the operating pressure. These parameters can be adjusted to reach the desired film properties (Thornton, 1986). Additionally the distance between substrate and target can be changed. If the substrate is in the vicinity of the plasma ions, ion bombardment of the film will change the film growth (Mattox, 1989). The energy distribution of the ejected material depends on the scattering events on their way to the substrate and on the energy distribution of the plasma ions.

For oxide sputtering, RF sputtering has been used. In RF sputtering one applies an alternating potential to one side of a dielectric plate and a discharge exists on the other side, so that a displacement current can flow though the dielectric into the plasma. A positive potential of the dielectric plate causes a large electron current to flow to the surface of the plate, charging it negatively. The current saturates a few volts above the plasma potential at a high enough value to remain negative when the plasma is switching to positive. This causes an ion current to the target. If the cycle length is short enough, the target surface can remain negative. The ions take, because of their mass, several cycles to arrive at the target and have an energy distribution which peaks approximately at the peak of RF voltage. High pressures during sputtering can smear out the energy distribution through scattering of the ions.

In this work all thin films have been prepared in a Leybold CLAB Clustertool sputter system consisting of six four inch magnetron sputter sources, a two inch source and a handler system which enables to coat up to eight four inch wafer. The sputter system is completely computer controlled and the parameters are the argon spatial pressure (via the turbo pump shutter), argon flow, the power applied to the sputter target and the application of the sputter masks which are installed. The film thickness has been measured on calibration samples (i.e. sputter time =100s), applying X-Ray Reflectometry (XRR).

For evaporation of gold on the molecules a home build[8] system with integrated quartz oscillator has been used.

---

[8] Designed and built by Dr. K. Rott.

Magnetism of Thin Films

In this section I will shortly outline the principles of magnetism of thin films and the mechanisms involved. A deeper insight can be found in (Vaz et al., 2008)*and in the citations therein.*

Magnetism is caused by the Pauli Exclusion Principle, the electron-electron repulsive Coulomb term of the electronic potential and the kinetic energy of the electrons. Different electron spin states are coupled via their electron orbitals by the exchange energy. The exchange energy can be described by the Heisenberg Hamiltonian for localized spin states:

$$H = \sum J_{ij} S_i \cdot S_j$$

where J_{ij} is the exchange integral and S_i the spin of atom i. Other magnetic terms are the magnetic anisotropy term (originating from spin-orbit coupling), the classical magnetostatic energy term and the Zeeman term.
Usually the exchange energy is much larger (0.1 eV/atom) than the magneto static (0.1 meV/atom) and magnetic anisotropy (10µeV/atom), but in thin films certain length scales can be reached, which change the influence of magnetostatic and magnetic anisotropy for the macroscopic magnetism of a sample.
The excess exchange energy density is for cubic or isotropic materials:

$$e_{ex} = A(\nabla \boldsymbol{m})^2$$

where A is the exchange constant and $\boldsymbol{m}=\boldsymbol{M}/M_S$ is the magnetization unit vector with M_S the saturation magnetization.
The anisotropy energy density is usually expressed phenomenologically by:
$e_{uni} = K_u(1 - \alpha_3^2) + K_u'(1 - \alpha_3^2)^2 +$...for uniaxial materials and
$e_{cub} = K_1 \sum_{i>j} {\alpha_i}^2 {\alpha_j}^2 + K_2 {\alpha_1}^2 {\alpha_2}^2 {\alpha_3}^2 +$…for cubic materials,
where the α_i are the direction cosines of the magnetization.
The magnetostatic energy density term can be written as

$$e_{ms} = 2\,\pi \boldsymbol{H}_d \cdot \boldsymbol{M}$$

where $\mathbf{H}_d$ is the magnetic dipolar field created be the magnetization distribution, given by[9]:

$$\boldsymbol{H}_\mathrm{d} = -\mathcal{M}\boldsymbol{M}$$

---

[9] Ellipsoidal geometry

and $\mathcal{M}$ is the shape dependent demagnetizing tensor. Due to the long range character of the dipolar interaction the shape of the specimen plays an important role for the orientation of the magnetization. For this reason the name shape anisotropy often occurs in the literature. In thin films the shape anisotropy is the main reason for a preferred in-plane configuration.

From these expressions the exchange length l_{ex} and the domain wall width l_{dw} can be calculated.

$$l_{ex} = \sqrt{(\frac{A}{2\pi M_S^2})}$$

$$l_{dw} = \sqrt{\left(\frac{A}{K}\right)}$$

In thin films considered in this work the film thickness is smaller than the exchange length.

The exchange constant A is a measure of the interaction strength of neighbouring spins and is a phenomenological parameter that reflects the magnetic symmetry of the system, which can be related to the microscopic parameters of the system. Sadly it is hard to obtain for thin films, so that usually bulk values are used for calculations.

The magnetic anisotropy with the anisotropy constant K is a relativistic manifestation of the coupling between the electron spin and the orbital moment. Therefore local changes in the electronic structure at surfaces and interfaces are expected to lead to changes in the magnetic anisotropy – this can result in interface induced perpendicular magnetic anisotropy, as first shown by Gradman and Müller in $Ni_{48}Fe_{52}(111)$ thin films (Gradmann and Müller, 1968).

Following Néel's notation the surface anisotropy is given by

$$E_S = K_S cos^2\theta + K_{S,p} sin^2\theta cos^2\phi$$

where θ and Φ and are the polar and azimuthal angles of the magnetization vector with respect to the direction perpendicular to the surface, respectively. If K_S is negative, the first term favours perpendicular anisotropy. An in-plane surface anisotropy is expressed through the second term, which must be considered in lower symmetry surfaces, e.g. fcc(110), bcc(110), etc.

Although this model is very intriguing, it fails often in the prediction of the sign of K_s, a more detailed discussion of that matter can be found in (Vaz et al., 2008).

The effective uniaxial anisotropy perpendicular to the plane of a thin film can be written as[10]:

$$K_{u,eff} = 2\pi D_m {M_S}^2 + K_u + \frac{2K_S}{t}$$

with the magnetic dipolar energy contribution as the first term, K_u is the magnetocrystalline energy contribution from the bulk and the surface magnetic anisotropy energy contribution is the last term. The out-plane demagnetizing factor D_m, which is approximately one for thin films, is in general a function of the film thickness, e.g. for an undistorted fcc (001) film it is D=1-0.2338/n (n>1 is the film thickness in monolayers).

If one introduces strain, magnetoelastic coupling will contribute to the anisotropy. $K_{u,eff}$ becomes

$$K_{u,eff} = 2\pi {M_S}^2 + K_u + B_{me}\epsilon + \frac{2K_S}{t}$$

where ε is the strain and B_{me} is the magnetoelastic coupling coefficient. Strain in films can be caused by e.g. thermal strain, associated with differences in thermal expansion coefficients, intrinsic strain caused by the nature of the deposition process and strain due to lattice mismatch.

The thin films switch from out-of-plane to in in-plane magnetisation after reaching a certain thickness. This can be understood, if one takes into account the competition between the surface and volume terms. One obtains a critical thickness:

$$t_{SRT} = -\frac{2K_S}{2\,\pi\,M_S^2 + K_u}$$

Below the critical thickness the sign of $K_{u,eff}$ changes its sign from positive to negative and the spins prefer to lie along the surface normal. This model ignores higher order anisotropies as they occur in e.g. Co(0001)/Au(111).

---

[10] For very small domains, the magnetostatic interaction between the domains is such that the magnetostatic term can be described by: $\frac{1}{2}\mu_0 M_{s,perp}^2$(average perpendicular component of magnetisation)(Johnson et al., 1996)

Deposition Of Molecules Or Nanoparticles On Substrates

For specimen deposition several methods can be found in the literature e.g. (Gomar-Nadal et al., 2008). The most common technique is to simply drop cast the specimen in a solvent, which will evaporate on the surface and will leave the entities on the surface.

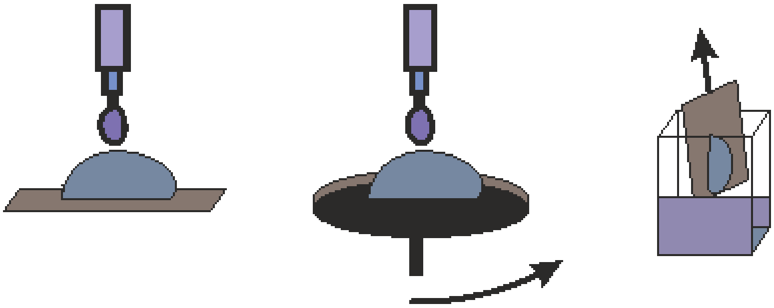

Figure 16 Schematic of drop-casting (left), spin-coating (middle) and sample-drowning (right).

It is also possible to apply a droplet to a sample and to mount it on a spin coater[11] (or apply the droplet during rotation). Furthermore the whole substrate could be drowned in the solution and pulled out slowly, so that the sample is wetted. All of these methods have in common that after the exposure to the solution of specimen and solvent, the solvent evaporates and the specimen is distributed over the substrate.

Self-Ordering

In general two methods of self-ordering can be distinguished: self-assembly which happens near the equilibrium and self-organisation which usually occurs far from equilibrium. Self-assembly is usually a process determined by surface potentials on surfaces of the substrates. Self-organisation forms patterns under uniform surface potentials, in a highly non-equilibrium environment and with strong non-linearity. In Figure 17 the relationship between order and disorder and the grade of non-equilibrium is schematically shown.

---

[11] Spin coater are common tools for lithographic processes, they are usually rotating the sample and used for resist coating.

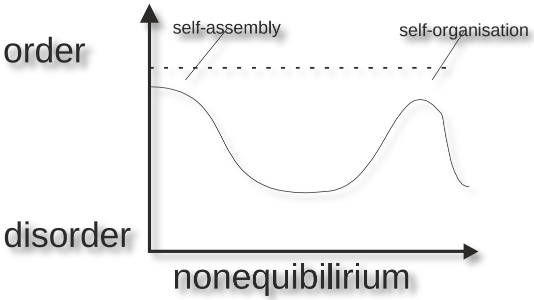

Figure 17 Schematic characteristics of self-assembly and self-organisation. The transition from disorder to order can be described as a function of non-equilibrium (super saturation) in the liquid drying process. Inspired by (Hosokawa et al., 2007).

The description of self-ordering processes in colloidal systems can be deducted from the self-organisation during the drying process of nanoparticles. The schematic drying process is shown in Figure 18.

The movement of the nanoparticles in liquid is governed by newton's law. Several forces acting on the nanoparticles must be taken into account. There are horizontal capillary forces due to the shape deformation of free surfaces caused by interaction between nanoparticles and solvent, electrical forces caused by the surface charging of the nanoparticles and also magnetic forces as magnetic nanoparticles are used. Brownian force based on the molecular movement in the solvent must also be considered. Additionally vdW forces between the nanoparticles occur. The force between nanoparticle and substrate is a friction force based on the Coulomb rule. Which force dominates the drying process is governed by the drying rate. High drying rates create more disorder while slow drying rates will result in more ordered films. Dipolar interactions are responsible for colloidal crystal formation. These interactions can be electrostatic or magnetostatic. The involved forces can be manipulated in order to achieve the desired effect.

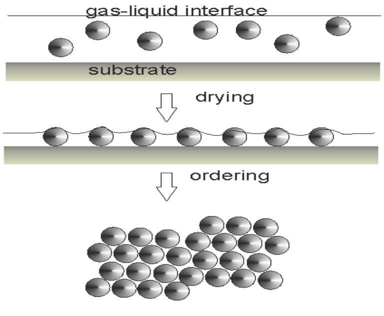

Figure 18 Schematic drying process.

RESULTS

Magnetic Multilayer Sytems As Substrates For SPM

In this section the utilisation of magnetic multilayers as a magnetic substrate for SPM measurements are discussed.

Why magnetic multilayers?

While spin-polarized STM and other spin-dependent SPM techniques rely on a magnetic tip, which are difficult to prepare, magnetic substrates can be prepared fast and easy with sputtering techniques.

In the literature (e.g. (Jia et al., 2011)) single crystals with an ultrathin magnetic layer prepared by MBE have been the preferred choice for SPM investigations on magnetic surfaces, because of the highly controllable MBE process and therefore high quality thin films. Although these substrates have several advantages they take some effort in handling and time to prepare.

Sputtering has evolved to a technique that can produce high quality thin films with high quality interfaces as can be seen in e.g. TMR elements (Thomas et al., 2008). Therefore using sputtered thin films for SPM investigation should be possible in general.

Magnetic multilayer systems have been vastly investigated in the past e.g. by (Stiles, 2006), (Johnson et al., 1996) and many others. They can be “tuned” by adjusting the film parameters to have different properties e.g. the magnetisation can be in-plane or out-of-plane, depending of the magnetic interlayer thickness. The advantage of multilayers over a single magnetic thin film is the easily accessible magnetisation because the magnetic moment of the system is detectable enough for typical measurement methods. The disadvantage may be the higher roughness and less defined interfaces.

Magnesium Oxide Cover Layer

This section discusses the detection and structuring of the magnesium oxide cover layer and shows the resulting images.

The magnetic thin films prepared in this thesis have been covered with a thin magnesium oxide cover layer. The chosen nominal thickness of the layer was between one and two monolayers in order to have enough coverage on the substrate which is still thin enough to obtain STM images. Magnesium oxide is known to be isolating even in monolayer thickness (Schintke et al., 2001) and has a large band gap (7.7 eV)(Daude et al., 1977). Because of the low nominal thicknesses used in this work, the success of the deposition has been checked with AES. A TEM grid has been used as a sputter mask to demonstrate the MgO coverage in SEM.

Auger Electron Spectra

Auger Electron Spetroscopy is very surface and material sensitive (Powell et al., 1999). Even small amounts of deposited materials can be detected. The characteristic Auger-electron energy for Mg is 1150 eV. The presence of Mg has been checked for the samples and a small bump in the spectra at the characteristic energy has been found as presented in Figure 19.

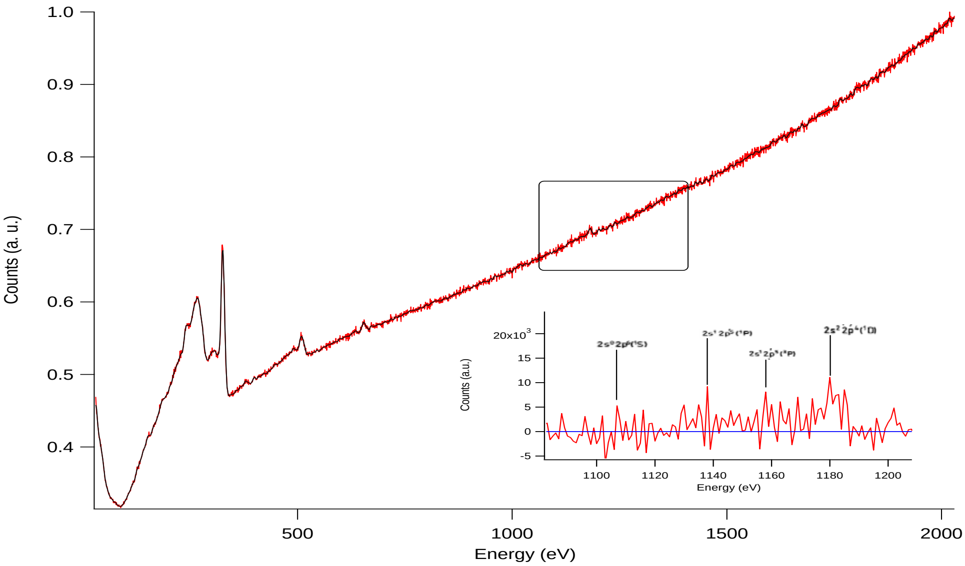

Figure 19 Typical complete AES spectrum with marked MgO peak taken on a CoPd multilayer. The black line is a smoothed line in order to visualise the curvature. The nominal thickness of the MgO layer was 0.2 nm. The inset shows the marked region with subtracted background and the positions of the MgO peaks.

TEM grid deposition

Additionally to the AES investigations to prove the existence of the MgO cover layers a TEM grid was used as a sputter mask. Commercially available TEM grids are coated with carbon or Formvar and come in different sizes and shapes. A carbon coated gold TEM grid with five micron wide quadratic holes has been put into an ultrasonic bath until the carbon coating was removed. After removing the carbon, the TEM grid was mounted onto the sample by pressing it on the surface with a metal sheet clamped on. The metal sheet had a hole a bit smaller than diameter of the TEM grid, a schematic is shown in Figure 20. In Figure 21 SEM images of the mask sputtered MgO are shown. As the MgO has been sputtered on gold, the charging of the MgO layer gives a good contrast in the SEM picture.

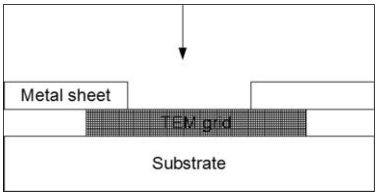

Figure 20 Schematic of the deposition process. The grid was clamped onto the surface with a metal sheet with a hole in it, which was slightly smaller than the TEM grid.

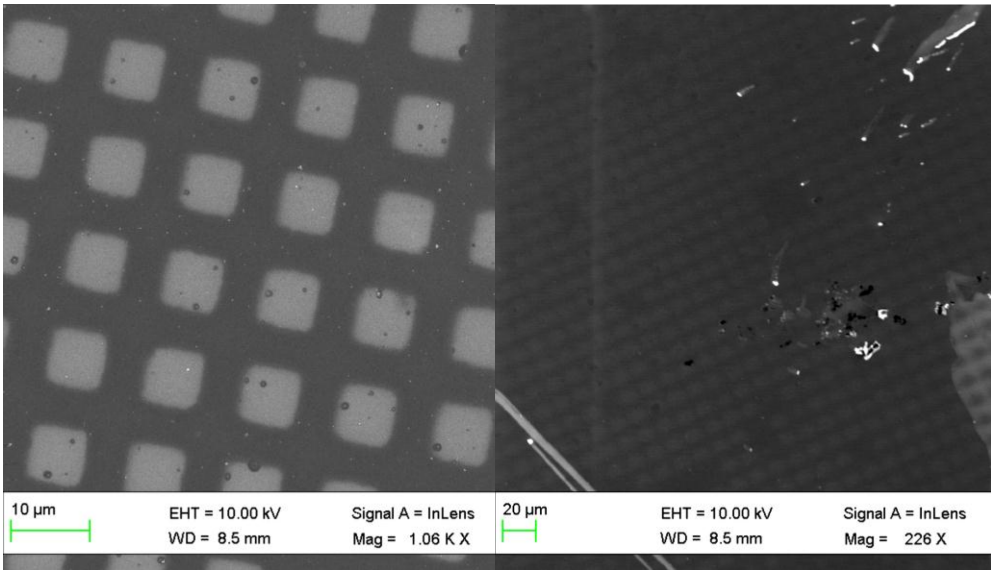

Figure 21 SEM picture of MgO deposited through the mask on Au. The nominal film thickness of the MgO is 5 nm (on the left). Even a nominal thickness of 0.5 nm results in a clearly visible pattern (on the right).

Using a TEM grid as a deposition mask is an easy and convenient way to achieve a patterned surface. In the Section about magnetic molecules a TEM grid will be used for the patterning of molecules on a thin-film substrate.

Cobalt Palladium Multilayer

Cobalt Palladium multilayer with ultrathin cobalt layer have first been investigated by Carcia et. al. in 1985 (Carcia et al., 1985). *They exhibit an out-of plane magnetisation which can be attributed to the interfacial strain and polarisation effects of the Pd atoms in the Pd layer beetween the cobalt layers* (Draaisma and de Jonge, 1987). *The interfacial strain is caused by the lattice mismatch (Cobalt (HEX/FCC): 2.51 Å/3.54 Å, Palladium (FCC): 3.89 Å). In this section AFM/STM/MFM images are shown and discussed. Occurring aging effects under ambient conditions will be demonstrated.*

Sample preparation

The multilayer systems have been sputterdeposited on SiO_{50}/Si Wafers. Samples usually have been characterised shortly after preparation. The mainly used layerstack $[Co_{0.4}Pd_{1.8nm}]_{x9}$ $MgO_{0.2nm}$ is depicted in Figure 22.

For the MFM measurements $[Co_{x}Pd_{1.8nm}]_{x19}$ MgO_{2nm} layerstacks have been used, with x=0.4 nm, x=0.45 nm and x=0.5 nm. The samples were prepared with a base pressure of $1 \cdot 10^{7}$ mbar and an argon pressure of $1 \cdot 10^{3}$ mbar. The argon flow was held at 20 sccm. The applied power to the targets has been 115 W for the MgO and Co and 60 W for the Pd.

Film thicknesses have been calibrated with XRR measurements on calibration samples.

Further details about similarly prepared CoPd layerstacks and details about their magnetic behaviour optimisation can be found in (Kugler et al., 2011).

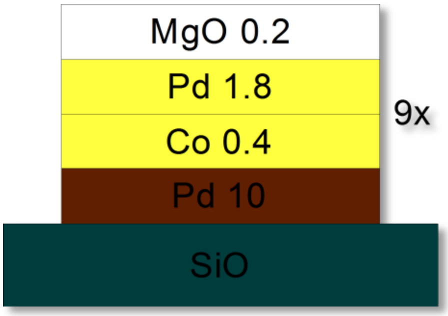

Figure 22 Schematic of the mainly used layerstack.

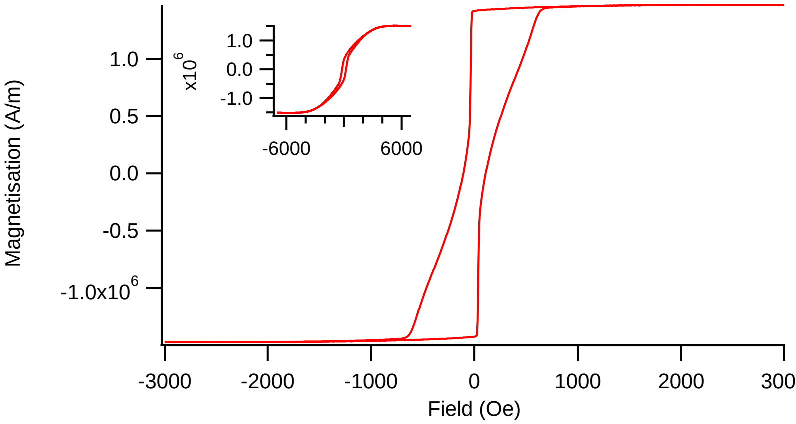

Figure 23 Out-of-plane AGM measurement[12] of the $Pd_{10}[Co_{0.4}Pd_{1.8}]_{x9}MgO_{0.2}$ multi-layer. The inset shows the in-plane measurement.

Magnetic properties

The out-plane magnetism has been confirmed with MOKE and AGM measurements, a typical AGM curve can be seen in Figure 23. The magnetisation curve shows the characteristic shape for out-of-plane magnetisation as shown schematically in Figure 24. The magnetisation change from up to down starts with nucleation of domains at the nucleation field H_n. After the up and down domains have reached an equilibrium at the minimum magnetisation of the nucleation field, the domains start to switch from up to down until the saturation magnetisation M_S is reached. The magnetisation from down to up undergoes the same process from the other direction.

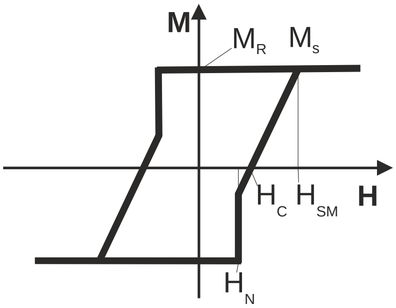

Figure 24 Schematic magnetisation curve of the layerstack with M_S as saturation magnetisation, M_r as remanent magnetisation, H_{SM} as saturation field strength, H_c as coercive field strength and H_N as nucleation field strength.

---

[12] The magnetisation is calculated by first approximating the magnetic volume (VM) (VM = sample weight * magnetic thin film thickness / wafer density). In order to obtain the magnetisation the measured moment is divided by the magnetic volume.

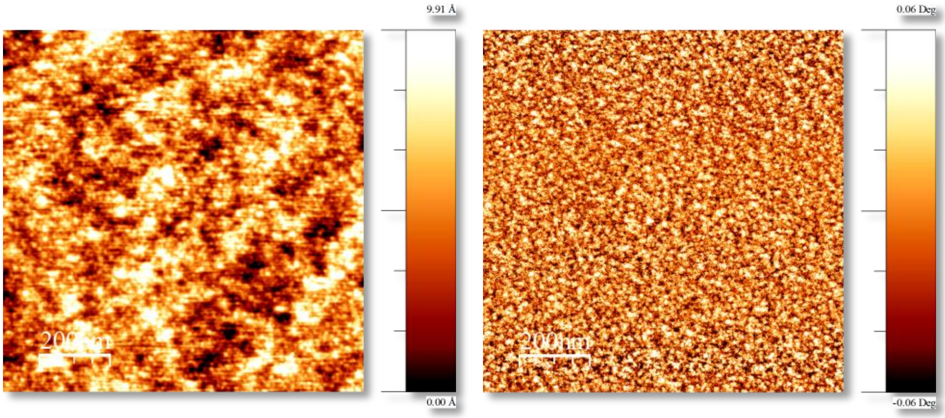

Figure 25 Tapping mode AFM images (topography on the left, phase image on the right side) of the Pd MgO Surface. The measurement was made shortly after preparation. The topographic image is equalized in order to expose the grain structure.

AFM images

The tapping mode images obtained with a standard tip from the surface of the $Pd_{10}[Co_{0.4}Pd_{1.8}]_{x9}MgO_{0.2}$ sample presented in Figure 25 show very small grains with an mean grain size of approximately 3.6 nm (obtained using Gwyddions grainsize anaylsis). The height histogram in Figure 26 confirms an extremely flat surface.

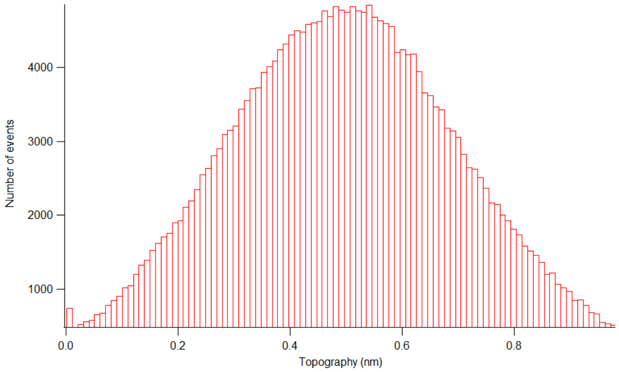

Figure 26 Exemplary height histogram of the AFM image. The image has a roughness (RMS) of: 0.23 nm.

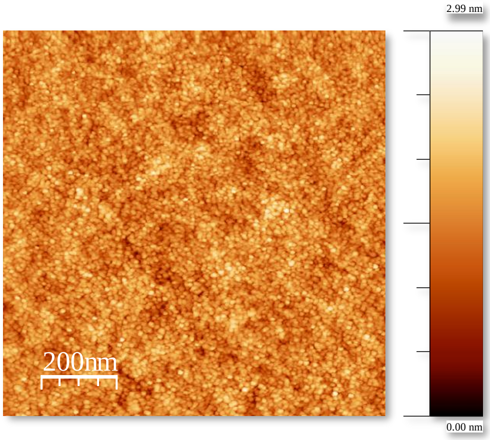

Figure 27 STM image of the Pd MgO surfaces. Settings were 1 V bias and a current set point of 5 nA.

STM images

STM images taken from the surface show the same flat topography as the AFM images, with a bit higher roughness (0.3 nm (RMS)), probably caused by the MgO (Nilius, 2009). A typical STM image is shown in Figure 27.
On fresh samples stable tunnelling currents between tip and sample could be established and stable measurements have been performed.
The flat STM image demonstrates convincingly that it can be used as a substrate for other entities though the small grain size makes small objects difficult to find.

MFM images

Figure 28 shows a schematic representation of the cobalt palladium multilayer system after Draaisma and de Jonge. The domains line up over several layers and domain walls are assumed to be very small.
In Figure 29 to 31 MFM images and their topographic images are shown. As the magnetic tips have been prepared via sputtering, the exact tip shapes and sizes are unknown. The samples have been reasonably flat (roughness < 0.6 nm (RMS))[13]. The tips have been magnetised shortly before the measurements. The lift height has been adjusted to 60 nm scan height. Due to the flat surface of the samples there was no change of the phase caused by surface corrugations.

---

[13] Aging effects caused the higher roughness. Further information can be found on page 57.

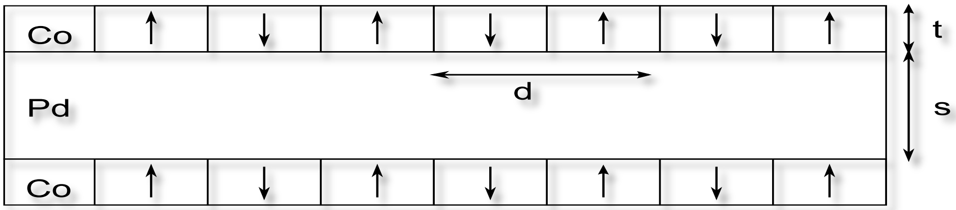

Figure 28 Schematic representation of a cross section of the multilayer films after Draaisma and de Jonge. The cobalt films are magnetised perpendiculary to the substrate plane. The domains line up over several layers and domain walls are very small. The domain width is d and the film thicknesses are s for the Pd layer and t for the Co layer.

The observed change in the phase image can therefore be attributed to magnetic interactions between tip and sample. The maze pattern is expected for out-of-plane magnetisation and has been analysed in detail by (Barnes et al., 1994) and (Rushforth et al., 2001). The maze structure clearly changes with the amount of Co in the magnetic interlayer thickness. In the demonstrated series the domain width is decreasing with increasing Co. As calculated by (Draaisma and de Jonge, 1987) this is not always expected, a minimum should occur, but the measured regime for the Co interlayer from 0.4 nm to 0.5 nm is too small to confirm the predicted behaviour.

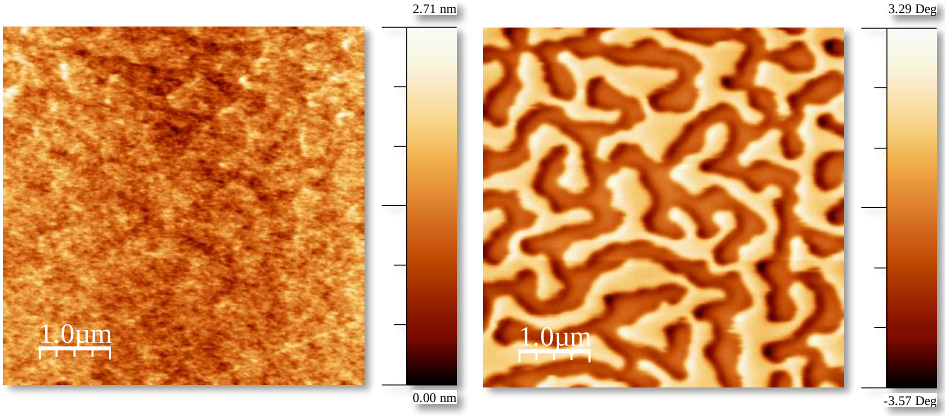

Figure 29 Topography (left) and MFM image (right) of CoPd multilayer with 0.4 nm Co layer thickness. The lift-height for the MFM picture was 60 nm.

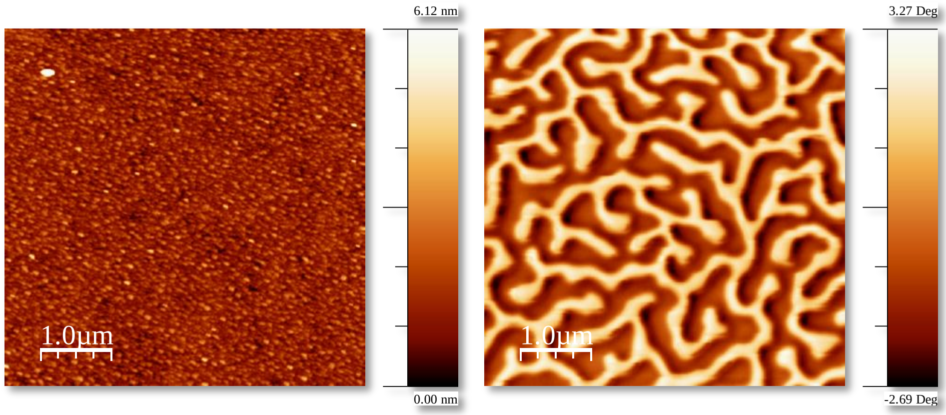

Figure 30 Topography (left) and MFM image (right) of CoPd multilayer with 0.45 nm Co layer thickness. The lift-height for the MFM picture was 60 nm.

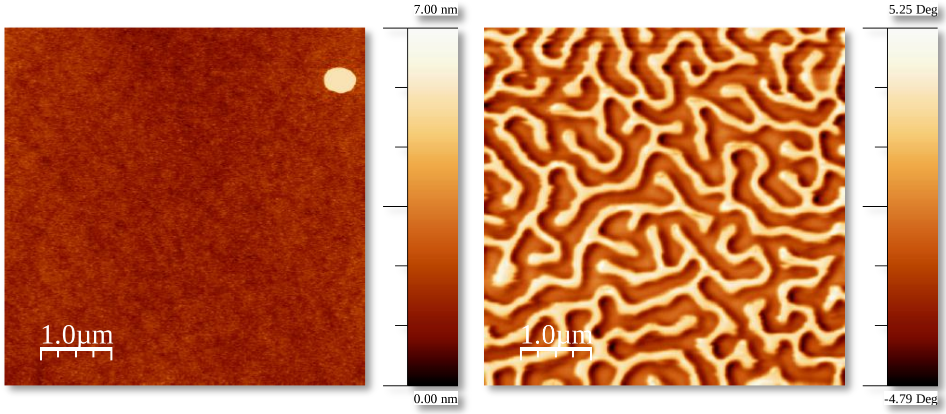

Figure 31 Topography (left, equalized) and MFM image (right) of CoPd multilayer with 0.5 nm Co layer thickness. The lift-height for the MFM picture was 60 nm.

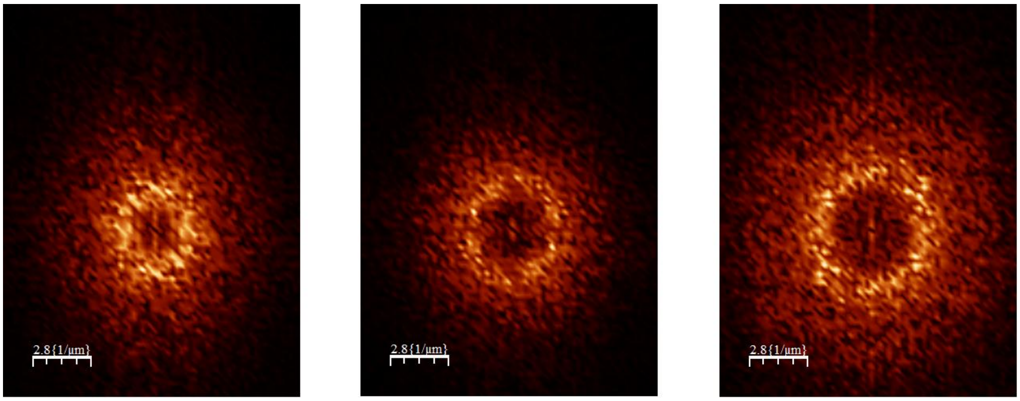

Zoomed in FFT of Figure 29 Zoomed in FFT of Figure 30 Zoomed in FFT of Figure 31

Figure 32 FFT analysis of the MFM images. The power spectral analysis results in a domain width of 625 nm for Figure 29, 444 nm for Figure 30 and 388 nm for Figure 31.

In Figure 32 a FFT analysis is of the MFM images is shown. If one calculates the power spectral density[14] for the images, one obtains the average value for the domain repetition length. The values are: 625 nm for Figure 29, 444 nm for Figure 30 and 388 nm for Figure 31.

Barnes et al. measured for a Co interlayer of 0.475 nm and a Pd layer with 1.43 nm in an 18 bilayer system a domain repetition length of 127 nm. This is a much smaller length than the ca. 416 nm (interpolated from Figure 30 and 31) of our samples. The observed difference can be attributed to a different measurement technique (lift mode as described on p. 31) and different film properties. Our films have been much smoother than the films investigated by Barnes et al. and a smaller grain size (Barnes: 20 to 40 nm). A higher quality film though should lead to larger domain sizes as the domains nucleate at film defects, so a film with fewer defects will exhibit larger domains.

---

[14] "Power Spectra" answers the question "which frequencies contain the signal´s power?" (or in an image “at which frequency does a change repeat”). The answer is in the form of a distribution of power values as a function of frequency, where "power" is considered to be the average of the signal. (http://www.wavemetrics.com/products/igorpro/dataanalysis/signalprocessing/powerspectra.htm)

Manipulation of the domains of a sample.

On the $[Co_{0.4}Pd_{1.8nm}]_{x9}\,MgO_{0.2nm}$ samples the cobalt content of the samples is less than in the above shown MFM images. Therefore the interaction forces caused by the sample are weaker and a tip which is exhibiting a high field can manipulate the domain structure of the sample.

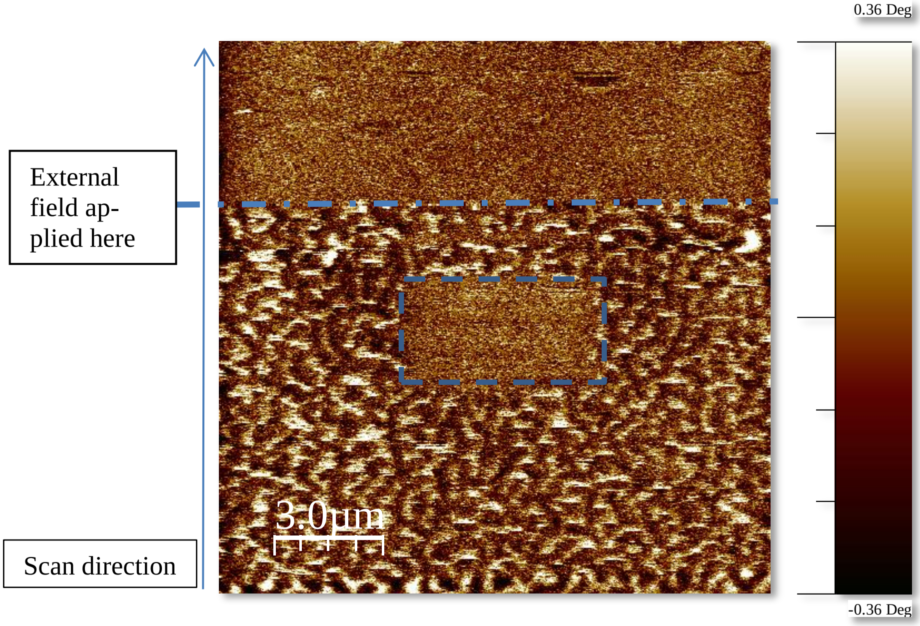

Figure 33 Manipulation of the domains with tip and magnet demonstrated in a MFM image.

In Figure 33 the manipulation of the domain structure of a sample is demonstrated. In the middle a recent scan area is visible. The tip “wrote” the area blank. At the marked line a magnetic field was applied to the sample and the maze pattern has been erased. Magnetic areas of such a sample can be patterned as needed.

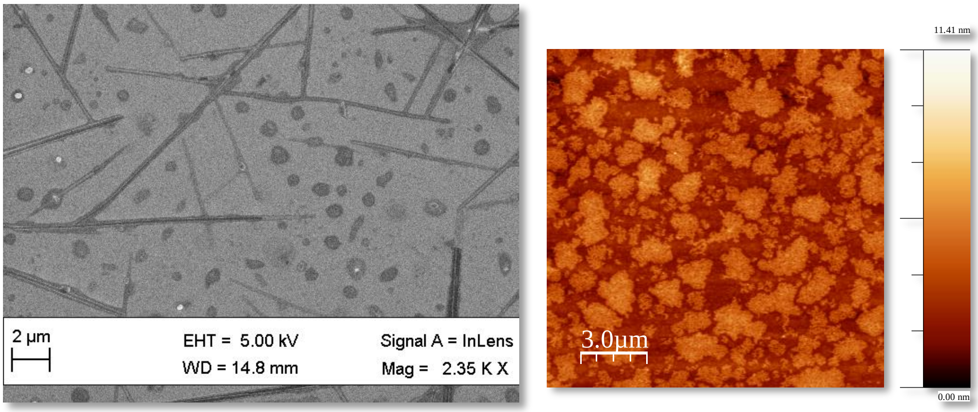

Figure 34 SEM image of an annealed sample after several days of exposure to air. (right left). AFM measurement of a several days old, not annealed sample (right side). Large crystals are visible.

Aging of the samples

During this work a rapid change of the surface of the samples has been observed. On the surface of the MgO covered CoPd samples crystals of unknown material appear. As Pd in combination with MgO is known to be a catalyst e.g. (Harding et al., 2008), the assumption of a chemical reaction on the surface is intriguing. However, we could not confirm or deny that assumption with an EDX investigation. The grown crystals are shown in Figure 34 (SEM image and AFM image). An annealed (annealing temperature of 250°C) sample is shown in the SEM image which has long rods. The AFM image shows an as prepared sample, which seems to grow islands of crystals. The growth of the crystals starts shortly after getting in touch with air and continues over time until the crystals are even visible without microscope.

The reason for the crystal growth is assumed to be a rearrangement of the Mg atoms on the surface of a noble metal driven by the oxygen from the air as it has been observed with e.g. Ag atoms on MgO cubes (Liu et al., 1992).

Cobalt Gold Multilayer

Cobalt Gold mulitlayer with ultrathin cobalt layers have first been investigated by Chappert et. al. in 1986 (Chappert et al., 1986). *They exhibit out-of-plane magnetisation for certain cobalt film thicknesses.*

Sample Preparation

The multilayer systems have been sputterdeposited on SiO_{50}/Si Wafer. Samples usually have been characterised shortly after preparation. A series of $Au_{10}/[Co_x/Au_y]_{9x}$ samples has been produced with x=[0.6 nm to 1.1 nm] and y=[1 nm to 6 nm]. The mainly used layer stack is depicted in Figure 35. Further details about the stack optimisation can be found in (Grote, 2010).

Figure 35 Typical stack used in the experiments.

Magnetic Properties

The magnetic properties of the multilayer systems have been investigated with AGM and MOKE as demonstrated in Figure 36. The out-of-plane measurements of both methods have been normalised and compared in order to check if one obtains the same curve shape. The saturation magnetisation is 621 kA/m and the coercivity is 155 Oe in this example. The lower saturation magnetisation is unexpected but has been observed in cobalt/nonmagnetic metal systems with changed surface to volume ratio (Ho et al., 2010). The curve shape deviates a little bit from the curves obtained for CoPd, which is probably caused by the different film smoothness and interfaces and or by the more or less failed automatic diamagnetic background subtraction of the AGM software.

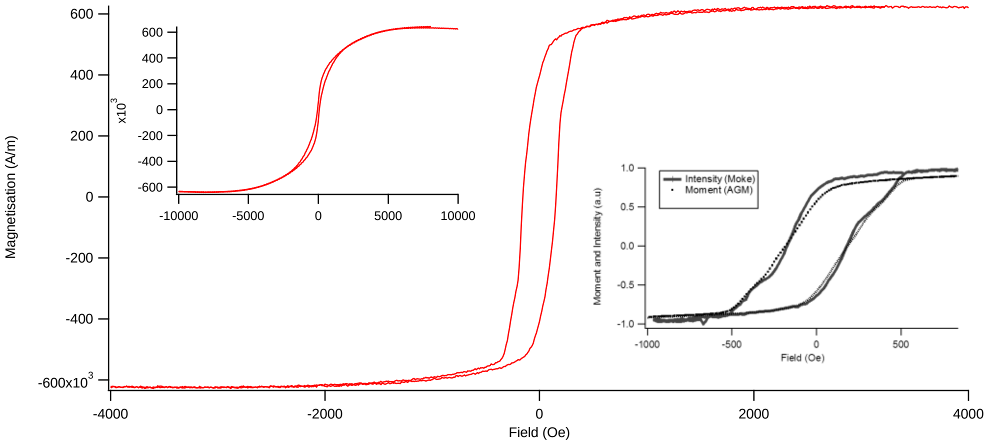

Figure 36 Magnetisation curves of $Au_{10}/[Co_{0.7}/Au_{6}]_{9x}$ measured with AGM. The left inset shows the in-plane curve.
In the right inset MOKE and AGM measurements are compared, the MOKE setup has been modified in order to measure the out-of-plane direction of the field.

AFM Images

In Figure 37 the AFM images of a MgO covered $Au_{10}/[Co_{0.7}/Au_{6}]_{9x}$ mulitlayer is shown. Gwyddions grainsize analysis results in a mean grainsize of 23.2 nm. The roughness of the AFM image is 0.47 nm (RMS).

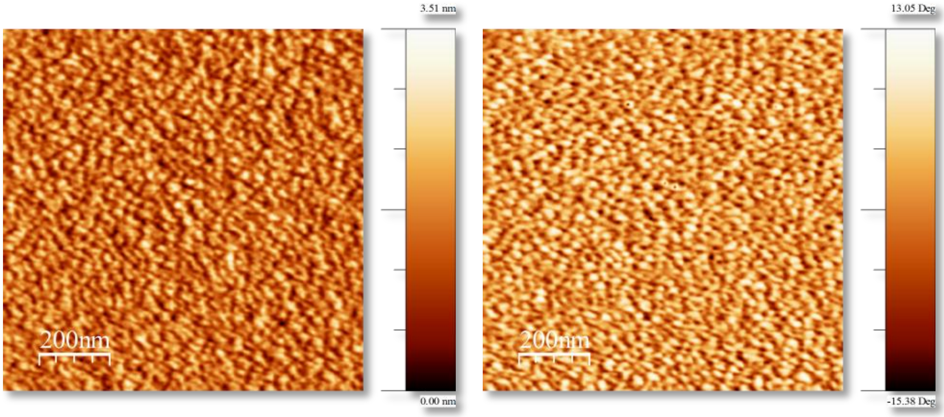

Figure 37 AFM image of CoAu Multilayer covered with two monolayer MgO. Topography is on the left side and phase image is on the right.

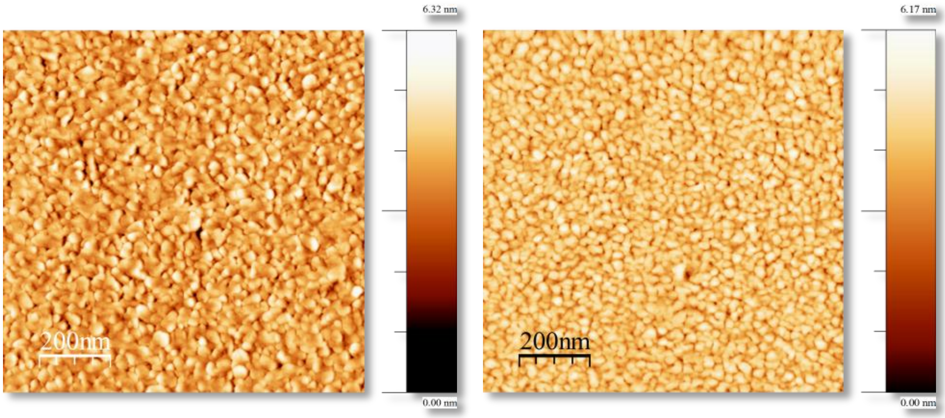

Figure 38 STM image of CoAu Multilayer covered with two monlayer (right) and with one monolayer MgO (left). Parameters to obtain images like those shown above were usually a current setpoint around 1 nA and bias voltages around 100 mV.

STM Images

STM images showed a roughness of approximately 0.6 nm (RMS). This is three times rougher than the CoPd multilayer systems. While the MgO mismatch is smaller, the grain size of the CoAu multilayer systems is ten times larger than the grain size of the CoPd systems. The larger grains seem to be the cause for the higher roughness, as their uneven facets corrugate the surface. This can be assumed analysing the image in Figure 38.

MFM

One MFM image of a MgO covered Au$_{10}$/[Co$_{0.7}$/Au$_{6}$]$_{30x}$ mulitlayer can be seen in Figure 39 and shows a maze pattern mixed with bubbles[15]. MFM images of CoAu systems have been discussed by (Donzelli et al., 2003). In our samples the large nonmagnetic interlayer (6 nm), chosen for better film properties, causes less coupling and therefore the Co layer behave nearly magnetically independent. The observed large domains (compared with (Donzelli et al., 2003)) correspond to that interpretation (Draaisma and de Jonge, 1987).

---

[15] The typical situation in a perpendicular magnetised film is that the domains are now connected with stray fields. In the walls the magnetisation lies parallel to the surface along different directions. Bubbles are isolated cylindrical domains that might form on perpendicular magnetised films due to their stability.

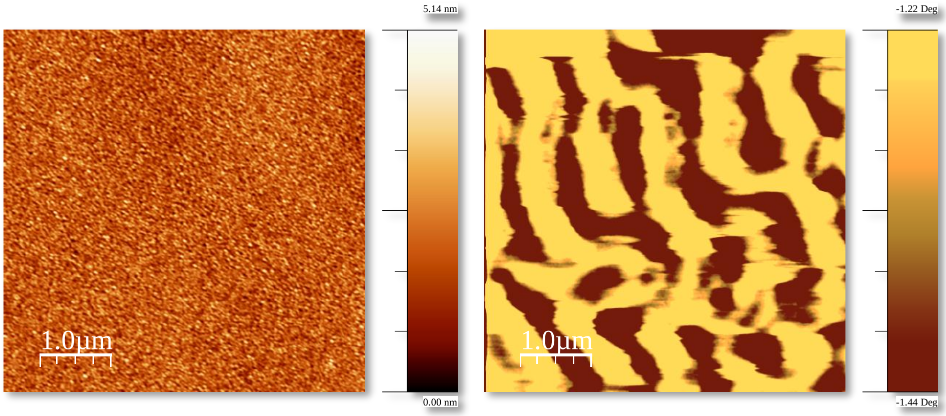

Figure 39 Topography (left) and MFM image (right) of a CoAu multilayer with 0.7 nm Co layer thickness. The lift-height for the MFM picture was 60 nm.

Aging

In order to make sure that the samples are stable in ambient conditions a freshly prepared sample has been measured initially and eight days later with SEM. The results can be seen in Figure 40: no visible aging effects have been observed. The MgO/Au combination is stable enough to be used in ambient condition experiments.

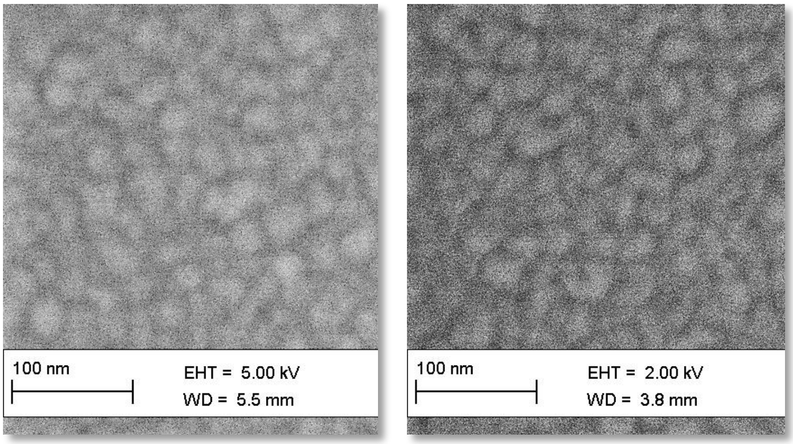

Figure 40 SEM picture MgO covered Au$_{10}$/[Co$_{0.7}$/Au$_{6}$]$_{9x}$ mulitlayer directly after sputtering (left side). SEM picture after eight days (right side): No aging effects have been observed during that time period.

Magnetic Molecules

Single Molecule Magnets (SMM) have been brought into the focus of physics through the pioneering work of (Gatteschi, 1994). *The multiple usefulness of SMMs can be found in the literature e.g.* (Sanvito and Rocha, 2006), (Leuenberger and Loss, 2001). *In this work the molecules have been deposited as an example for the accessibility of molecular nanostructures on magnetic substrates and investigated with AFM/STM.*

Molecules

The molecules used in this thesis are $[\{(\mathrm{talen}^{tBu}{}_2)\mathrm{Mn}_3\ \{\mathrm{Cr(CN)}_6\}]^{3+}$ solved in different solvents and are provided by the chemistry group of Prof. Th. Glaser[16]. Details about the used molecules can be found in (Glaser et al., 2006).

Spin Coating

The molecules have been solved in dichloromethane and solvent has been added until the liquid has become optical transparent (typically a concentration around $1{:}10^6$). The substrate has then been mounted on the spin coater and the speed has been adjusted to 6000 rpm. After starting the rotation, the molecules and solvent have been drop casted on the spinning substrate. A resulting AFM image is shown in Figure 41. The images have been obtained on the MgO covered CoPd multilayer systems discussed in the previous sections. Freshly prepared samples have been used to avoid the aging problems. The molecules stick together and build structures with a lateral diameter of 10 to 20 nm and a height from one to three molecular heights. These nanostructures exhibit a clear phase response, due to strong adhesion forces.

---

[16] $[\mathrm{talen}^{xx}]$ stands for the triplesalen ligands used to stabilize the molecules. In our case the tris(tetradentate) triplesalen ligand H(6)talen(t-Bu2).

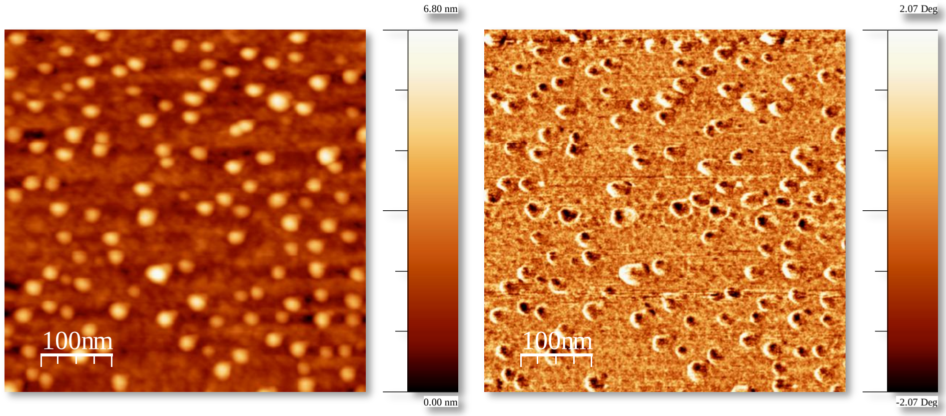

Figure 41 TM-AFM image of molecules deposited on CoPd with spin coating, using dichlormethane as a solvent. Low concentrations used. The coating speed has been 6000 rpm. The spinning time has been 30 s. Topography is on the left side and phase image is on the right.

While on the AFM images a clear distinction between the molecules and the underground can be made, this has not been possible on STM images. The solvent alters the electronic surface so that a distinction between underground and molecules can only be estimated by the height of the entities. Another approach would be CITS, which was not available with the STM at hand. Some STS curves have been acquired but as the location of the curve is unknown, it is difficult to evaluate if there are molecules involved at all.

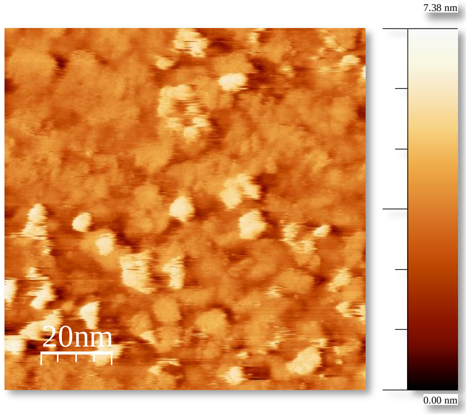

Figure 42 STM image of spin coated molecules. It is clearly difficult to identify the molecules only from the topography. Although a height contrast can be seen, the altered surface (caused by the solvent and/or the molecules) of the substrate makes an association of the prominent features with the molecules questionable.

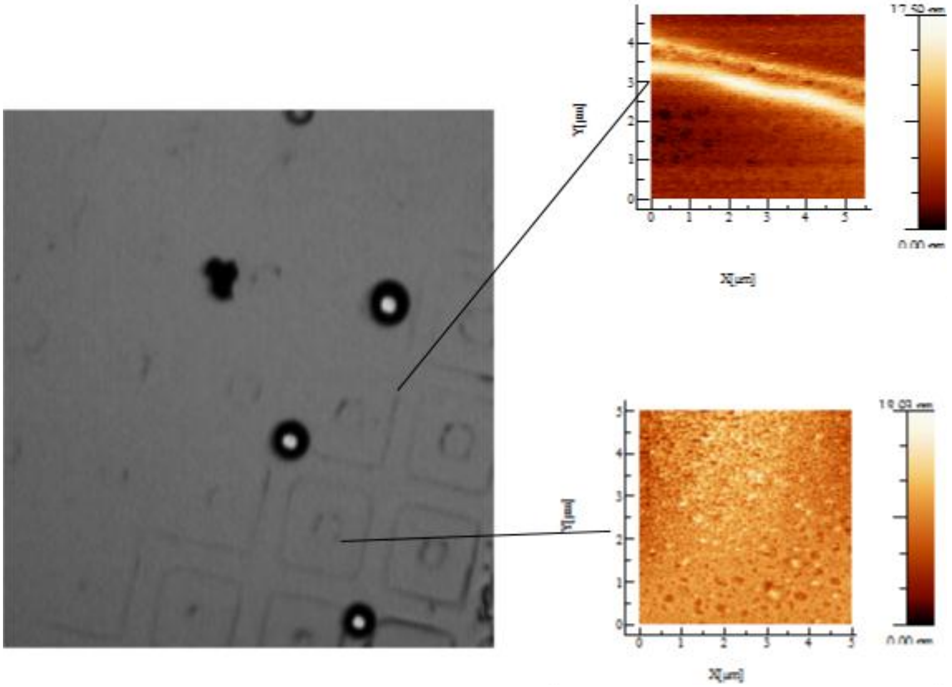

Figure 43 Using a TEM grid with 20 micrometre windows for patterning of molecules on a substrate. The microscope image in 200 times magnification shows patterned regions. AFM images of parts the patterned surface give a microscopic view of the patterning.

Mask deposition using a TEM grid

Lithography Assisted Wetting has been demonstrated as a tool for positioning specimen on the surface (Cavallini and Biscarini, 2003). We have tested the capabilities of a TEM grid to assist creating pattern of molecules on the surface. The TEM grids have been freed of the carbon layers in an ultrasonic bath and pressed on the surface of a MgO covered gold substrate. In Figure 43 the patterned surface is shown in an optical microscope image. The image shows clearly regions with higher concentration and regions with lower concentration of the drying solvent. In the AFM images a microscopic view of the high concentration regions in Figure 43 is shown, areas with a visible coverage, where molecules build clusters on the surface, are prominent. The general problem concerning the clusters is to identify molecules in them – the solvent (dichloromethane) usually is not as clean as desired, as it is solving residues contained in the air and surroundings. The solvent also covers homogeneously the surroundings of the molecule – adhesion differences between the substrate and molecules are not visible in the phase anymore.

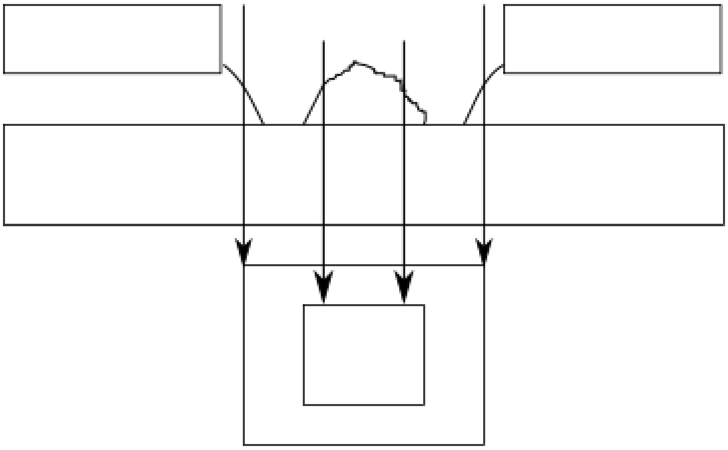

Figure 44 Schematic explanation of the rectangular pattern on the microscopy image. The capillary forces make the solvent dry at the contact points with the grid. In the middle forms a coffee stain pattern.

The process of how the patterns are established is illustrated in Figure 44.

In order to get a smaller pattern TEM grids with 5 µm windows have been used on another substrate and molecules in solvent have been deposited via drop casting.

During the AFM analysis areas with extremely low coverage have been targeted. In Figure 45 the results of the attempts to isolate molecules is shown. If the solvent is not equalizing the phase interaction a clear difference between the molecules (black spots) and the substrate can be seen in the phase image. It was then possible to isolate entities whose sizes correspond with the expected heights of a single molecule, obtained by (Heidemeier, 2006). Comparing with results obtained by the group of P. Müller in Erlangen shown in the Appendix the phase respond matches perfectly. They deposited only via drop casting without a TEM grid. Therefore the mask deposition technique can be considered as a working pathway in order to deposit entities at a local position.

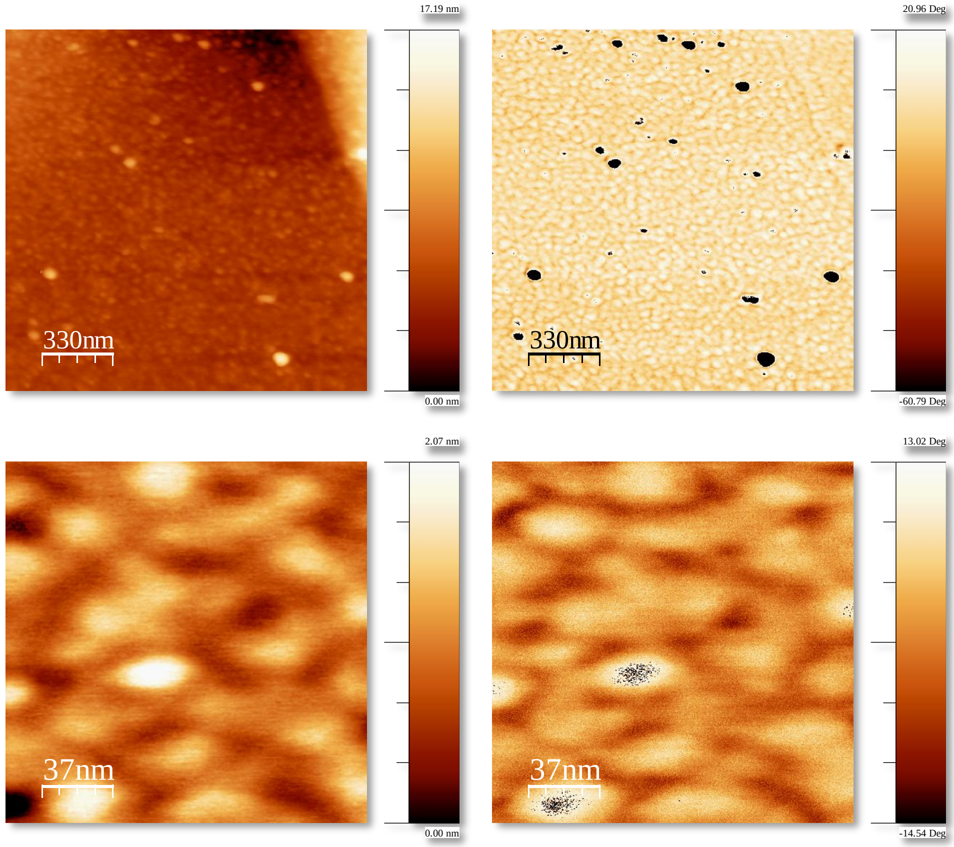

Figure 45 The areas in-between the patterned can exhibit very low coverage of the molecules. The upper image pair shows a survey of a region with low coverage. The lower image pair shows entities with the height of a single of molecules and a clear phase contrast (right images) could be identified. These images correspond with the findings of the group of P. Müller in Erlangen (see Appendix).

Kelvin Force Probe Microscopy On SMMs

Molecules have been drop casted on a MgO (0.5 nm) layer on Ru (10 nm) and afterwards covered with Gold (2 nm, evaporated). This sample has been measured with Kelvin Force Probe Microscopy. In Figure 46 an overview of the resulting images is presented.

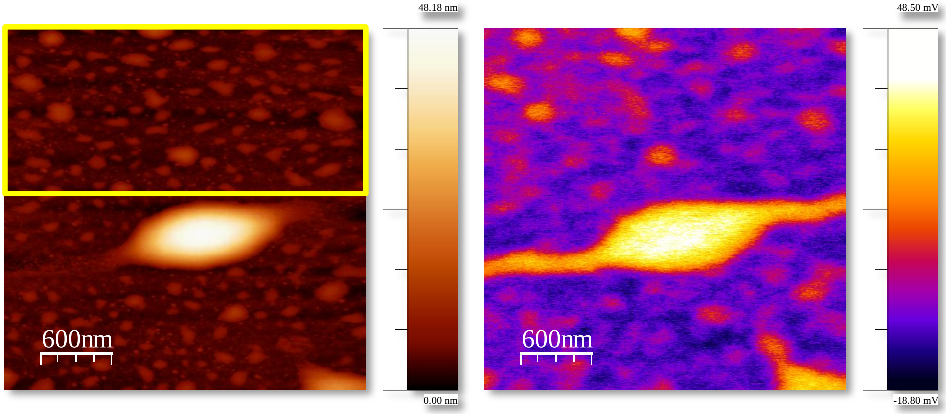

Figure 46 Overview measurement of molecules on theMgO/Ru surface. Large clusters and small clusters have been observed. The work function of the clusters with assumed molecules is higher than the measured work function of the surrounding substrate areas. The marked are is shown in **Figure 47**.

Large clusters surrounded by small clusters are visible. The small clusters have not all the same work function, although some of them have the same height. The difference in the potential is demonstrated in Figure 47. Higher potential is repulsive for electrons, which means that clusters with molecules should “light up” in the KFPM images.

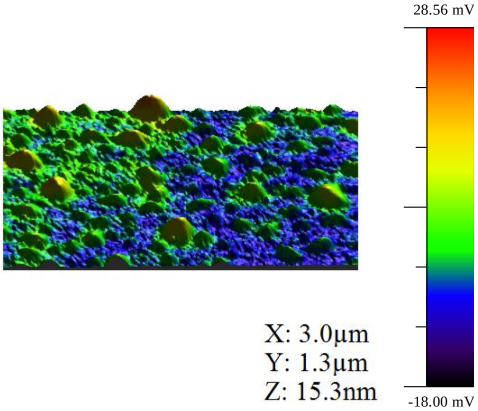

Figure 47 Upper region of **Figure 46** in detail with the layered work function map showing areas with higher potential on the left and regions with lower work function between the clusters.

Magnetic Nanoparticles

Since the success of magnetic nanoparticle synthesis in the 1960's (e.g. (Faber, O. C., Jr.; Papell, 1968) *the synthesis has made a huge progress. Puntes et. al. for example introduced in 2001 a synthesis that enables shape and size control of cobalt nanoparticles* (Puntes et al., 2001). *General information about the used nanoparticles can be found in* (Weddemann et al., 2010).
Cobalt nanoparticles have been deposited on HOPG and tapping mode AFM images have been acquired. Two different deposition processes are demonstrated. Finally the transport properties of clusters and single cobalt particles have been investigated.

Deposition Of Nanoparticles On Substrates

In the following the results of the deposition process are presented. In Figure 48 drop casted cobalt nanoparticles with a diameter between 6 nm and 12 nm prepared through thermolysis have built clusters on HOPG. The clusters can be found on HOPG edges and defects, where the nucleation process is taking place. This indicates that the particles adhere more to each other than to the substrate. The clusters themself seem to be structured due to self-ordering processes. The usual concentration of the nanoparticles in solution for this experiments is 1:50 (nanoparticle solution to solvent ((m)ethanol)).

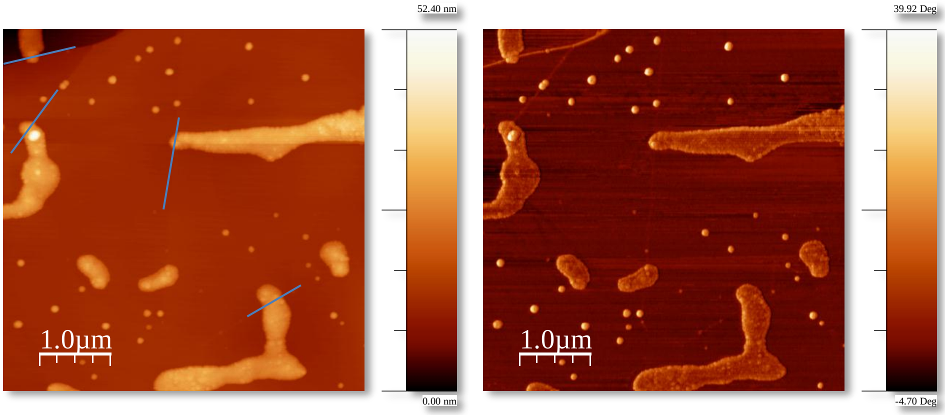

Figure 48 Drop casting cobalt particles on HOPG results on in particles clusters. The general result is cluster formation caused by strong capillary forces and inter particle forces. The clusters prefer HOPG edges (blue lines) as nucleation sites, but also reside at other nucleation templates given by the substrate, e.g. defects and contaminations. More images can be found in the Appendix (p. 118).

Ordering through external field

Without an external magnetic field the deposited particles organise in clusters as shown in Figure 49. In Figure 50 a small area scan shows that single particles already can be assumed and that the particles might have close range order in the clusters.

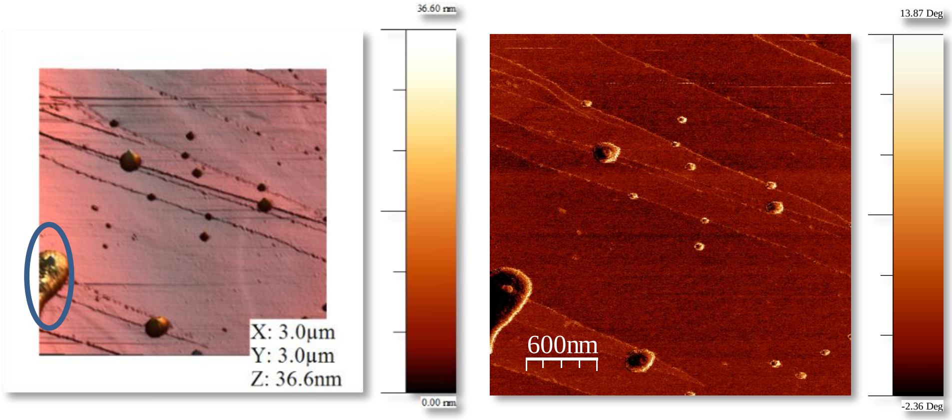

Figure 49 Large area scan of deposited cobalt nanoparticles on HOPG without applied filed while deposition. The topography is on the left and the phase image on the right. The close-up shown in **Figure 50** is marked.

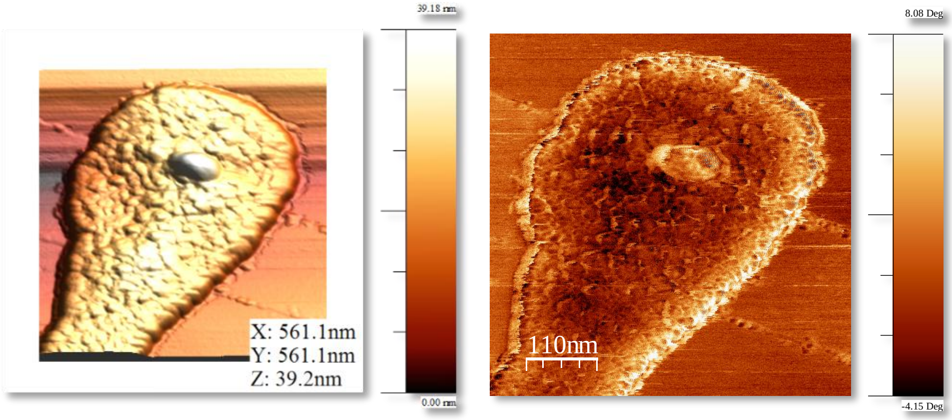

Figure 50 Close-up on a cluster. Single particles can be assumed comparing the sizes of the entities visible in topography (left) and phase image (right).

Applying a magnetic field while the solvent evaporates aligns the particles along the magnetic field, due to induced dipolar interaction. Only where they are free to move during the drying process they are able to align, at a barrier the particles are forced into another direction. This effect can be used for establishing patterns on the substrate. In Figure 51 the resulting alignment of the cobalt nanoparticles along the magnetic field axis is shown.

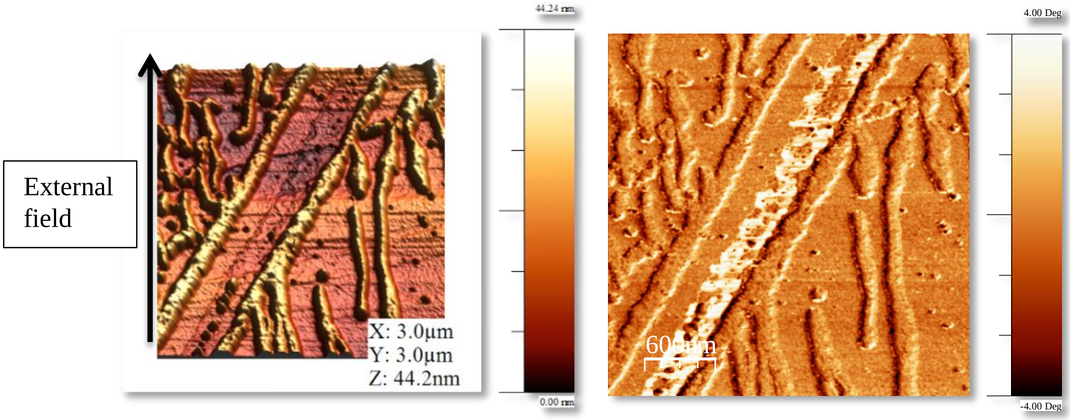

Figure 51 Deposition in a magnetic field. The superparamagnetic particles order along the field lines. The diagonal distortion of the particle lines is caused by the topography. 3D-Topography on the left, phase image is on the right side.

Self-organisation

Contrary to the simple drop casting in the section above cobalt nanoparticles prepared as a 1:50 solution have been drop casted onto HOPG in an argon atmosphere and directly after the deposition a vacuum is applied, which causes the solvent to evaporate very quickly. The resulting AFM and SEM images are shown in Figure 52. As the solvent evaporates fast, the drying process is far from equilibrium and therefore a self-organisation of the particles can be seen. The nanoparticles still reside in clusters, while the particles in the clusters are organised in hexagonal lattices. Mainly the clusters are as flat as one or two particle heights, which indicate that flat clusters are preferred. In Figure 53 an area of Figure 52 is magnified in order to show the hexagonal ordering. Applying a two dimensional FFT on the ordered particles reveals the typical FFT pattern of hexagonal ordered entities.

Without nucleation sites the clusters have no place to stick to. Plane edges on HOPG are these ideal nucleation sites and the clusters and particles are always found in the vicinity of a plane edge. Another example can be seen in Figure 54. More images of clusters nucleated at edges can be found in the Appendix on p. 118.

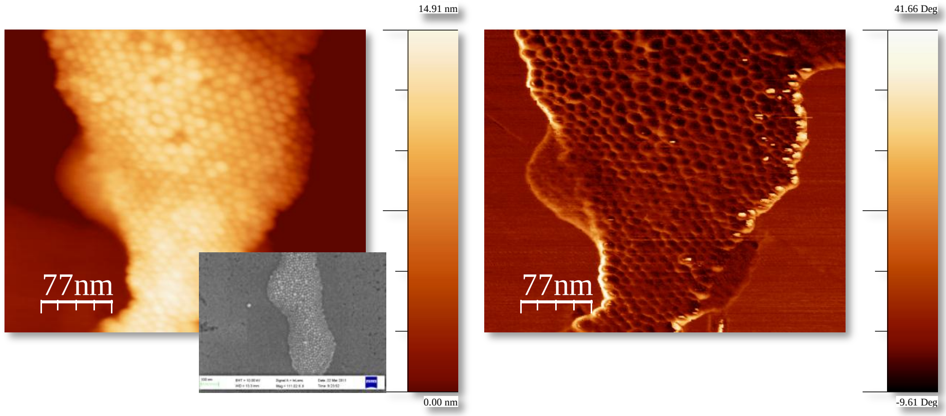

Figure 52 Tapping mode image of self-organised Cobalt nanoparticles on HOPG. The particles are clearly distinguishable in phase image (right) and topography (left). The small inset shows a SEM image of an ordered cluster.

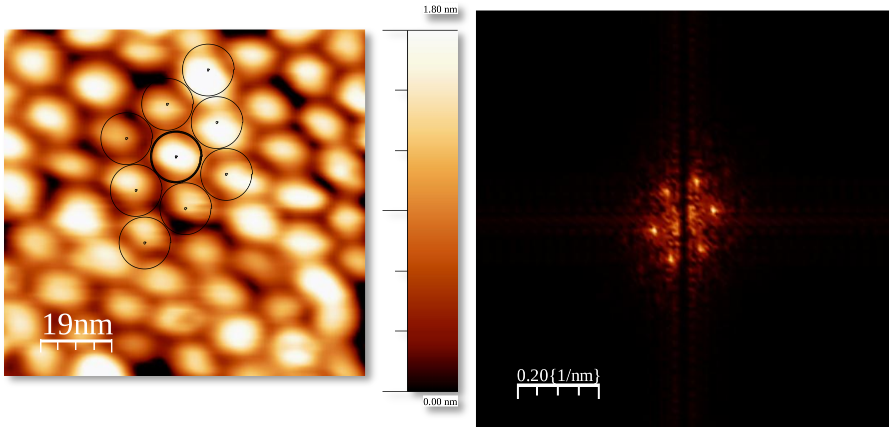

Figure 53 Hexagonal order of the particles. The image on the left is a magnified region of the topography of **Figure 52**. The right image is a 2d-FFT of that image and shows the typical pattern of a hexagonally ordered entities, with a particle distance of about 10 nm, which corresponds with the particle radius.

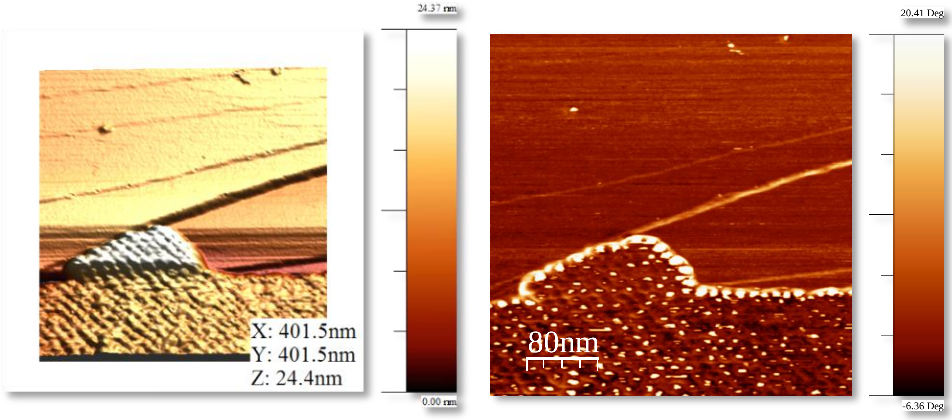

Figure 54 Another cluster located at a plane edge. Edges are ideal nucleation sites and are needed for the clusters.

Transport Properties Of Cobalt Nanoparticles

The transport properties of cobalt nanoparticles are important for future device applications. One possible application might be the design of GMR systems based on two magnetic nanoparticles connected via a CNT (Fu et al., 2005). *In order to realise such configurations it is imperative to understand the electronic transport through single particles and clusters. In this section measured conductance maps of cobalt particles and clusters on HOPG and their I-V curves will be presented. In* Figure 55 *a sketch of the measurement geometry is shown.*

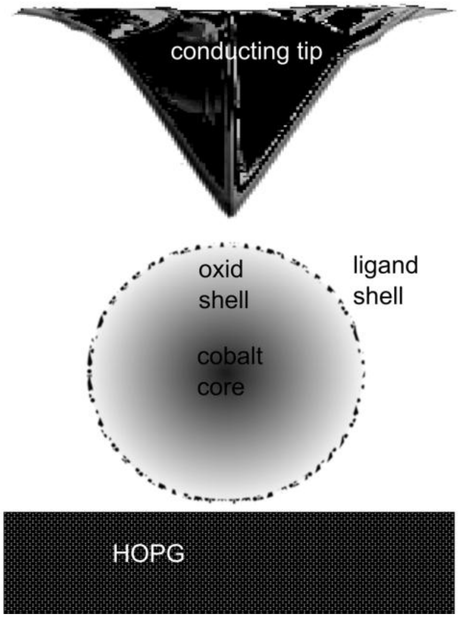

Figure 55 Schematic of the measurement geometry.

C-AFM is a common method in order to contact nanostructures and molecules (Mativetsky et al., 2008) and has been chosen for taking images of the magnetic nanoparticles and for taking I-V curves of them.

In order to measure single particles the concentration of the particles in the solvent has been reduced to 1:100.

Characterisation of the used nanoparticles

The particles used for the transport measurements have been deposited on a TEM grid and the diameter has been measured, SEM images were taken, and AGM measurements have been performed. In Figure 54 a TEM image of the particles deposited on a TEM grid is shown. Clearly sizes and shapes of the particles can be seen. The diameter statistics in Figure 56 gives an average of 6.8 nm ± 2 nm for the particle diameter. For comparison with AFM images one must keep in mind that the ligand shell is not visible in the TEM.

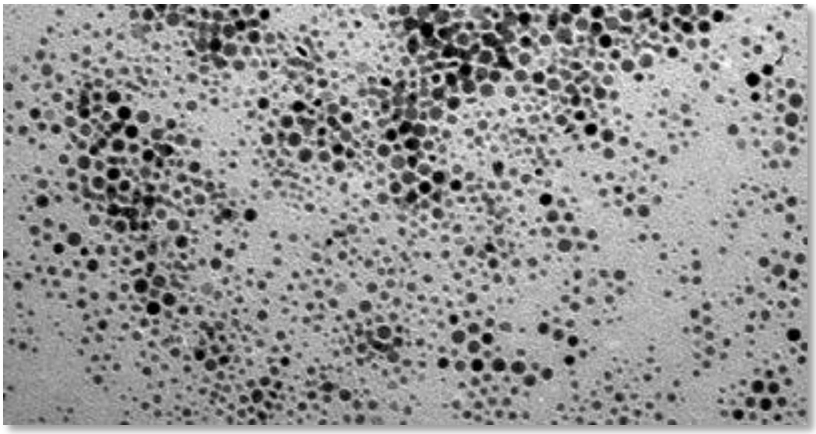

Figure 56 TEM image of the used particles on TEM grid. (Image width: 648.4 nm)

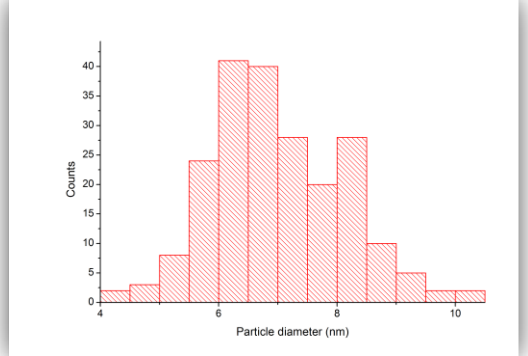

Figure 57 Particle diameter statistics. The resulting average is 6.8 nm ± 2 nm.

In Figure 58 a high resolution TEM image of a single nanoparticle is presented – regions of CoO on the outside and a Co core can be identified and the lattice constants can be measured. The polycrystalline regions of CoO on the outside give an impression of how inhomogeneous a possible contact area with the single particle can be. Cobalt oxide is believed to have two modifications, CoO in rocksalt structure and the spinel form Co_3O_4.

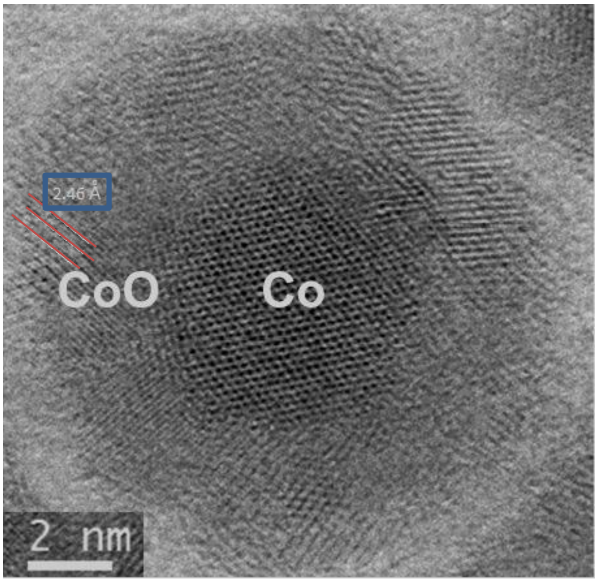

Figure 58 High resolution TEM image[17] of a single cobalt nanoparticle. The measured distances correspond with the lattice constant of CoO (For convenience not every measured distance is shown, but there are no distances which can be attributed to the spinel structure). The oxide shell does not consist of a monocrystaline layer, instead it has regions of CoO with different orientations.

Magnetic properties

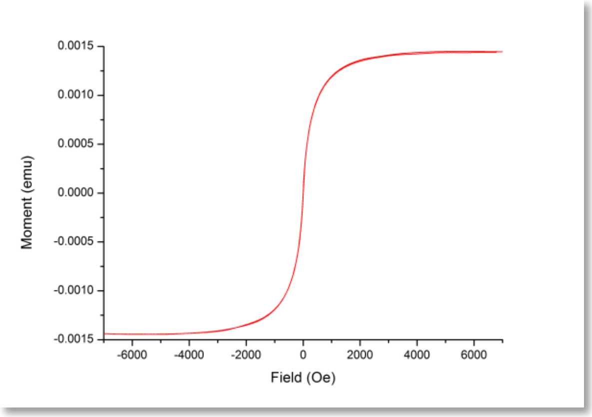

Figure 59 AGM curve of the used particles. They are superparamagnetic.

The magnetisation curve measured with an AGM shown in Figure 59 confirms the expected superparamagnetic behaviour of Co nanoparticles of this size. This means, that there are no attractive repulsive long time interactions between the particles.

---

[17] Acquired by Prof. Dr. A. Hütten of Bielefeld University at Jeol Ltd in Japan.

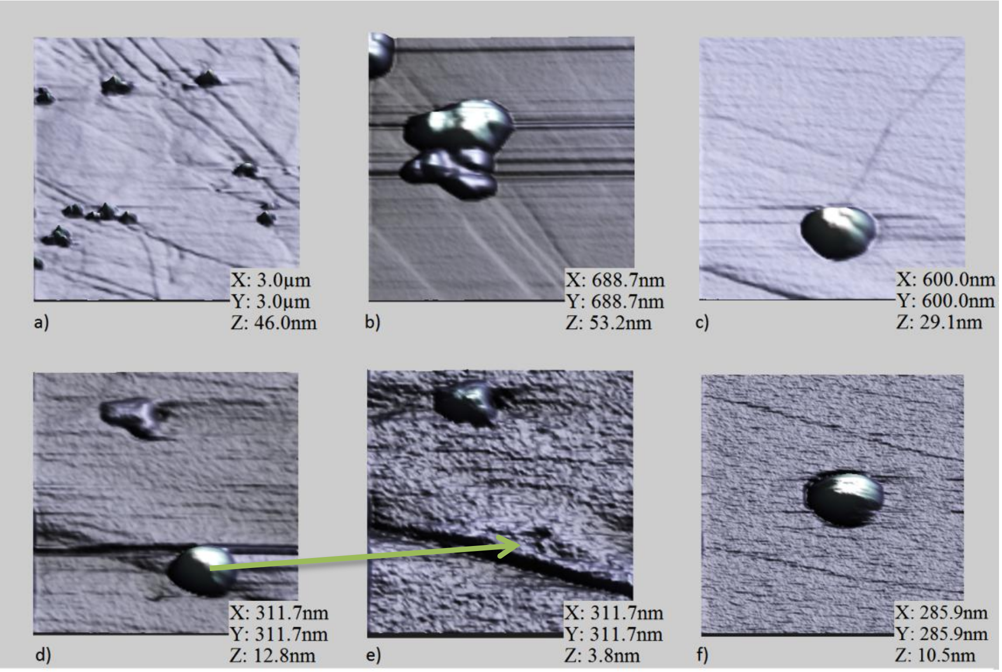

Figure 60 Topography images taken with a conductive tip, with a tip radius around 50 nm. a) Gives an overview over a typical region. b) and c) show clusters and d) and f) single particles. From d) to e) the particle has been removed.

Topography of the deposited nanoparticles

In Figure 60 topography images of the deposited nanoparticles on the HOPG are shown. In Figure d) and e) the same regions are imaged, where a single particle has been removed (indicated by the arrow). In order to remove particles the force setpoint is crucial and can be used to manipulate particles on the surface.

The slightly higher lateral size of single particles can be explained with rests of the solvent trapped at the ligand shell. This can be seen in lateral force images, as places where the particles have been removed are still deflecting the cantilever due to capillary forces as shown in Figure 61.

The mechanism of surface adhesion of the particles seems to be governed by the solvent. Therefore the particles are not strongly bound to the surface: this can also be observed with STM experiments, where the particles are simply moved aside by the tip (Figure 62).

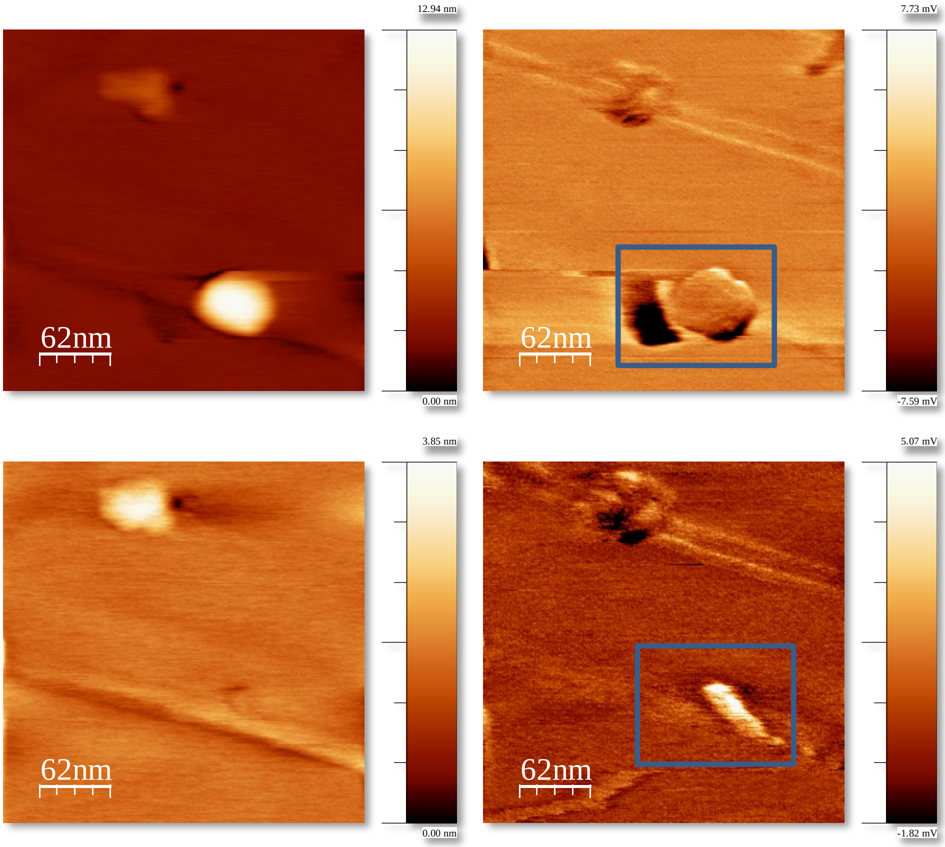

Figure 61 Topography images (left side) and the friction force images (right side) show that the particle is disappeared. At the spot where the particle has been, there is still a rest of the solvent which is visible in the friction image.

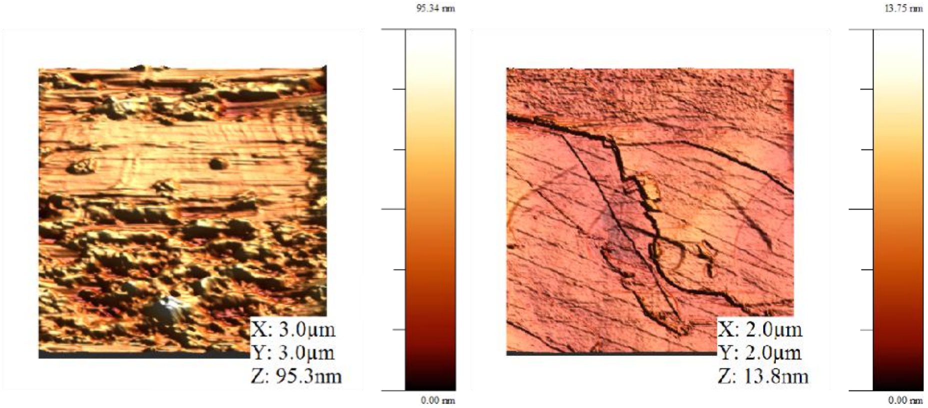

Figure 62 Contact mode AFM image on the left, STM image of the same sample, but not the exact same position on the right. No particles can be found with the STM, because they are moved aside.

Conductance maps

A common problem of C-AFM measurements is to establish a reliable contact between tip and item under investigation (Guo et al., 2006). In order to have an indicator for a good contact, the tip is brought in contact with the HOPG and the force set point is adjusted until the characteristic pattern (Banerjee et al., 2005) is appearing in the current image. In Figure 63 this pattern on HOPG is shown.

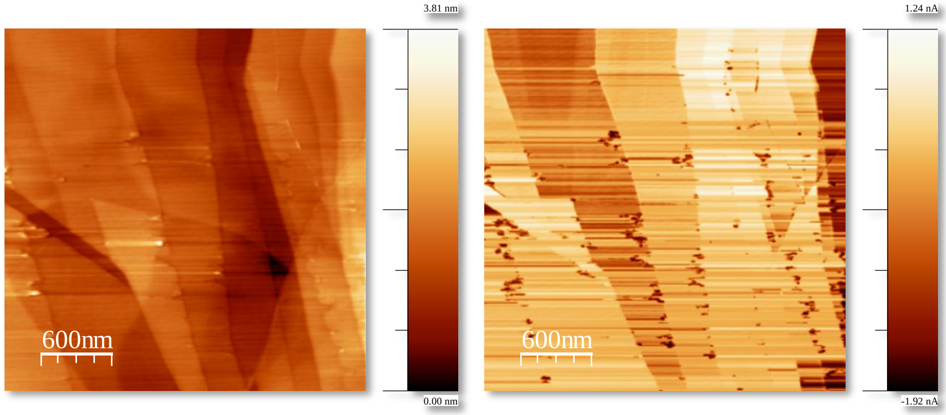

Figure 63 Topography of cleaved HOPG and the conductance map. The edges of the graphene flakes are clearly visible.

HOPG can be described as periodical stacked graphene sheets along the c-axis. In the a-b plane a strong σ bonding (sp^2) exists, while the perpendicular π-orbital electrons along the c-axis are the cause of the conductivity along the a-b plane by quantum mechanical hopping. The graphene layers are weakly bonded to their neighbouring layers through interlayer interaction forces. At the edges of the graphene layers the π electronic states are different - this causes an observable conductance change and can also be observed in the work function change at the edges. There is a vast amount of research concerning the edges of graphene sheets in the literature e.g. (Banerjee et al., 2006) which cannot be covered by this work. Concerning this work it is only important to know that the conductance and work function changes are there and therefore individual flakes of graphene can be recognised.

In Figure 64 the schematic explanation of the pattern is shown. For more detailed explanation the above mentioned literature is recommended.

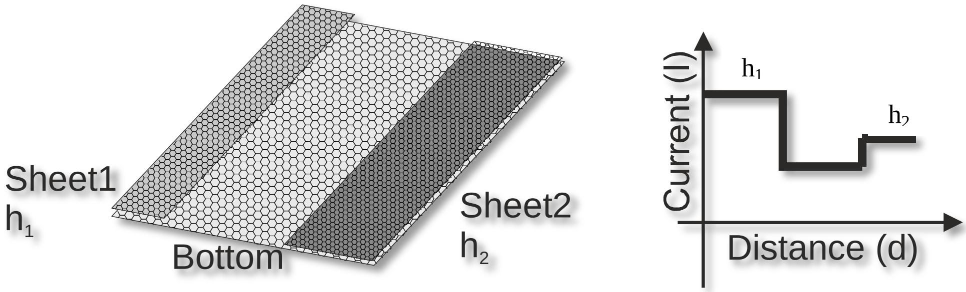

Figure 64 Schematic explanation of the stripes on the current map. The stripe with a larger distance h_1 has a higher electron mobility than the lower sheet h_2, because less electrons take part in the bonding vdW forces between the sheets.

Through the adjustment of the AFM parameters to make the pattern visible the contact between tip and surface is ensured.

In Figure 65 deposited nanoparticles on HOPG are shown in a survey image over a three micron large area.

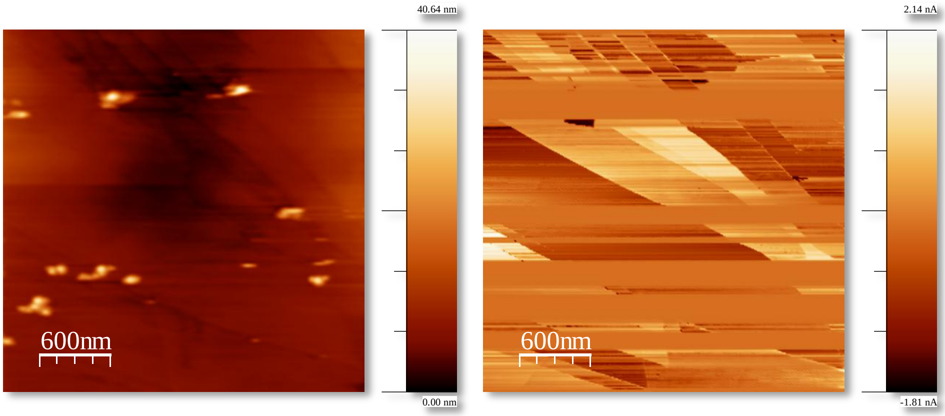

Figure 65 Overview over a region where drop casted particles as clusters and single particles reside. It is the same region as shown in **Figure 60** a). On the right the topography is shown and on the left the simultaneously obtained conducting map. The HOPG pattern is visible, but broken at the lines where the particle clusters are (explanation in the text).

In Figure 66 the topographies from single particles and particle clusters are overlaid by a colormap obtained from the simultaneously measured conductance maps.

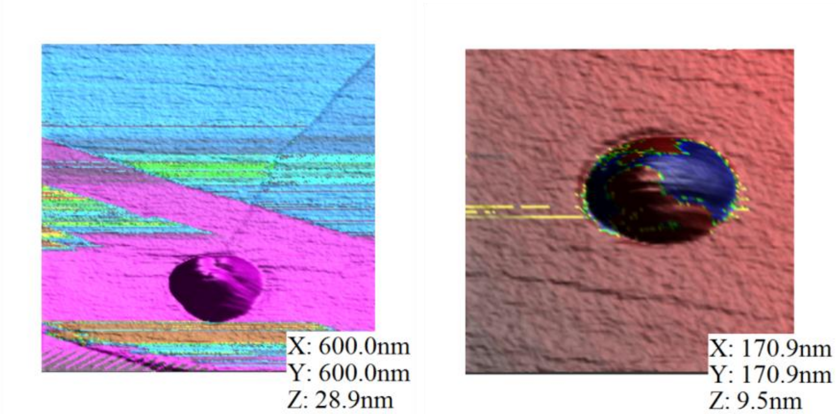

Figure 66 Topographies from a particle cluster (left) and a single particle (right) are overlaid by a colormap obtained from the simultaneously measured conductance maps. The topographies are from **Figure 60** c) and e)

In Figure 65 on the right side and in Figure 66 on the left side the HOPG conductance pattern vanishes in the scan lines at the locations, where the particles reside in the cluster. This could be caused by the feedback loop which adjusts the tip to the height of the particles. If the tip gets into a side-wall-contact with the particle, the feedback moves the tip to a slightly higher position above the surface so that the contact to the HOPG is lost. Alternatively the tip could have picked up some contamination from the solvent which either blocks the conductance or shifts the force setpoint through the compressibility from the liquid, so that the conductance disappears until the contamination is removed trough the scanning process.

The conductance map of a single particle shown in Figure 66 on the right side, however, showed some substructure and we assumed that the conducting parts of the particle can be attributed to metal and the less conducting parts to oxidised regions. The conductance maps give a general impression of the accessibility of the nanoparticles to local conductance measurements.

I-V Curves Of Cobalt Nanoparticles

In order to acquire I-V curves the point and shoot method of the Nanoscope software has been applied. First an image is acquired, then the points of interest can be marked and while the bias is ramped at this point, the current is recorded, a demonstration give Figure 67 and Figure 68. The resulting I-V curves were extremely sensitive to the applied force and to the state of the tip. Nevertheless, we observed characteristic features at low current regions around zero bias and the corresponding values for the band gaps match those of the different cobalt oxide configurations, i.e. 3.7 eV for CoO and 1.3 eV for the indirect band gap of the spinel Co_3O_4 (Yamamoto et al., 2004).

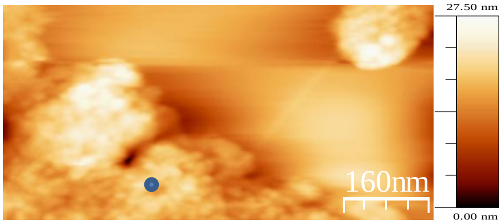

Figure 67 Demonstrating the point and shoot method: First an image is acquired and then the region where the I-V curves should be taken is marked.

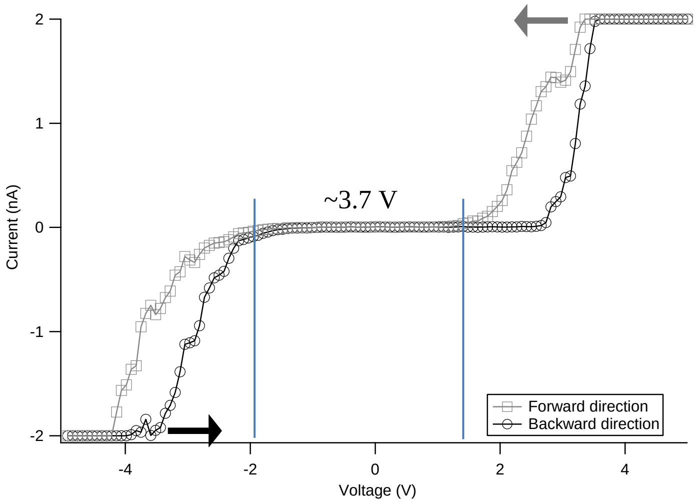

Figure 68 The averaged curves taken on the position marked in **Figure 67**. A shifted gap can be seen. The gap size is approximately 3.7 V.

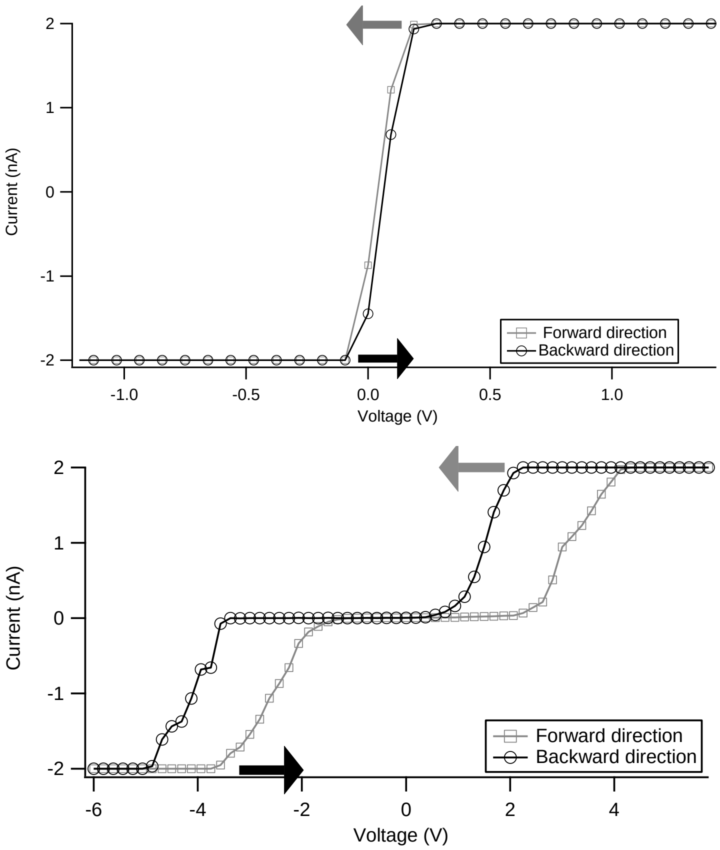

Figure 69 Typical I-V curves on HOPG (upper) and on small clusters (lower). The graphs are averaged I-V curves from at least 3 curves at different places. The gap visible on the right side is nearly the same as the gap found on the bulk particle clusters (**Figure 68**).

I-V curves of HOPG and Clusters

In Figure 69 typical I-V curves taken on small clusters as depicted in Figure 60c and HOPG are shown. For the HOPG I-V curves shown in Figure 69 on the top, the tip was moved to a position away from any particle. Similar results could be obtained on pure HOPG and in the vicinity of the particles. It corresponds with the expected behaviour for a metal-graphite contact. Small differences were obtained at atomic steps on the HOPG. Note that the output of the I/V converter saturates at I= 2 nA.

The small clusters show a similar I-V curve as the bulk particle clusters of Figure 68 with the large band gap of 3.7 eV. But here is a different behaviour at the edges of the clusters - on several occasions a change to a smaller gap has been observed. This is caused through possible single particle contacts The change to the smaller gap is shown in Figure 70.

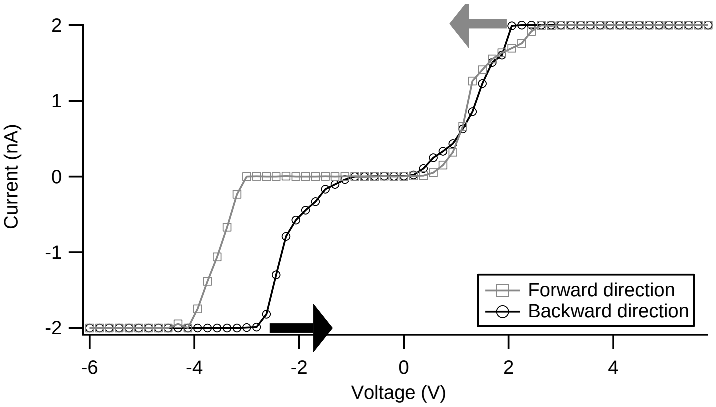

Figure 70 Changes observed at the edges of small clusters. The plateau changes from the wide gap in the forward direction to the smaller gap in the backward direction.

In Figure 71 a histogram analysis of the I-V curves on clusters is presented. It shows the trend to different band gaps: most prominent is the 3.7 eV gap and the smallest observed is the 1.3 eV gap, which is mostly observed at the edges of clusters. Additionally the 2.4 V plateau can be seen. It is the corresponding plateau to the 2.4 eV band gap of bulk cobalt.

The histogram also demonstrates that the contact stability is still an issue: Several of the I-V curves are far away from any reasonable value. An example of the typical obtained curves is given in the Appendix.

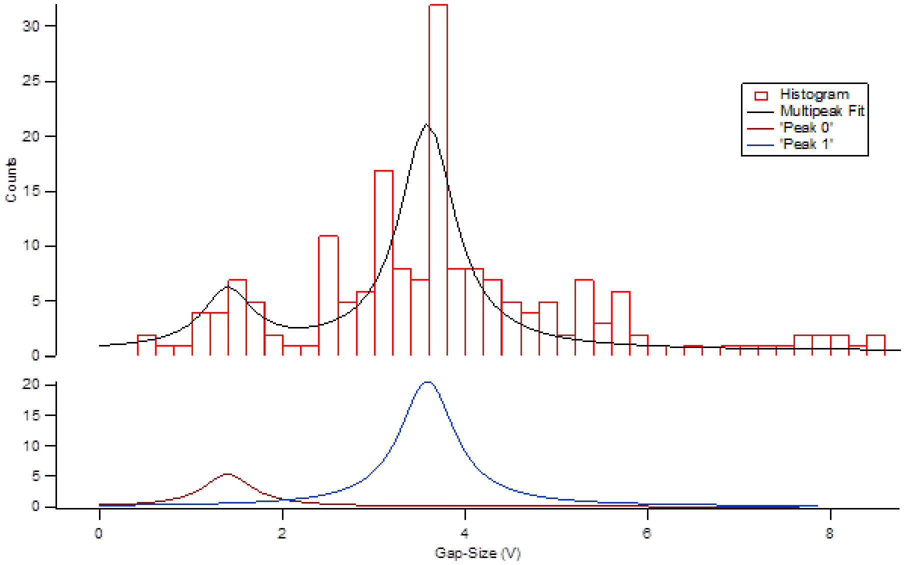

Figure 71 Histogram-Analysis of the I-V-curves on the clusters. The gap sizes are shown and the bin[18] size is 0.2 V. There are peaks by 1.3 V, 2.4 V, 3 V, 3.7 V, 5 V, 6V and around 7.8V . The clear peak at 3.7 V is caused by the CoO gap. The small one at 1.3 V is only found on single particles and at the edges of clusters. The peak at 2.4 V corresponds with the bulk band gap of CoO.

---

[18] The bin size has been chosen with respect to the distance between two measurement points in the I/V-curves. Applying a rule of thumb for gauss distributions would give a bin size of 0.9 V, which would not give a detailed enough overview of the results here, as there are multiple peaks (D.W. SCOTT, Biometrika **66**, 605-610 (1979)).

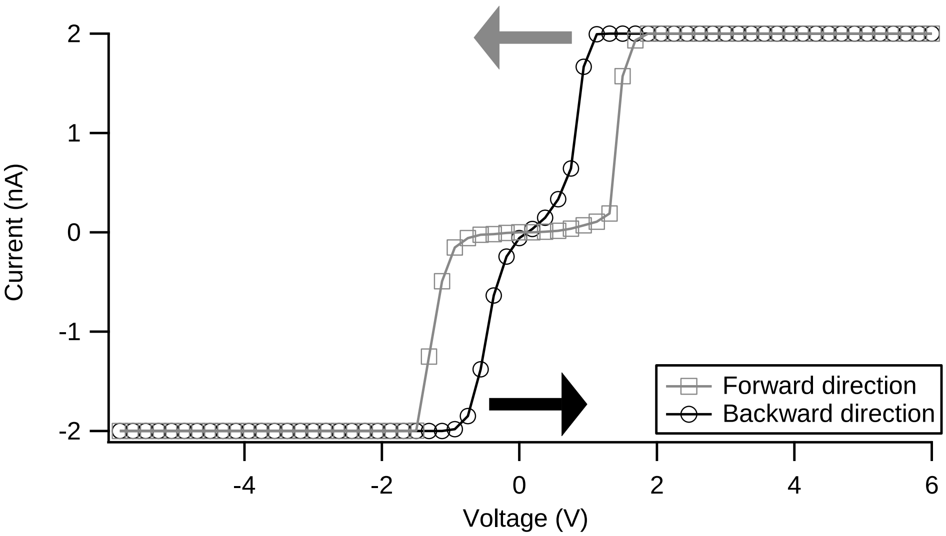

Figure 72 Single particle curve. The forward (black) and backward (grey) voltage scan direction are shown. The gap in the forward direction is 1.3 V. The observed dielectric breakdown (i.e. the disappearing of the gap in backward direction) can be attributed to ion movement in the particle. The topography of the single particle where this curves have been obtained is shown in **Figure 60** f).

I-V curves of clusters and single particles

As clusters of particles are high enough to bring the tip out of contact with the HOPG at the cluster edges this is not the case for a single particle. Additionally, the I-V curves of the cluster show a much wider gap than that observed for single particles as shown in Figure 72.

Here, the corresponding gap is 1.3 eV, i.e. it is in the regime of the indirect band gap of spinel cobalt oxides. Taking a look at the voltage sweep directions in Figure 67, it is interesting to see that the gap is observed in the forward direction. The backward voltage sweep shows a much smaller gap width and thus a breakdown of the resistance in the forward-scan gap region. Because a repetition of the measurement reproduces the same breakdown-behaviour this cannot be attributed to a permanent dielectric breakdown. This finding also corresponds with the soft dielectric breakdown behaviour observed by other groups (Inoue et al., 2008). In Figure 73 the histogram analysis for single particles is shown. It demonstrates clearly two peaks: one at 0.5 V and one at 1.3 V. While the 0.5 V peak can be due to small contact resistances caused by the ligand shell, it is nearly always observed in the backward direction.

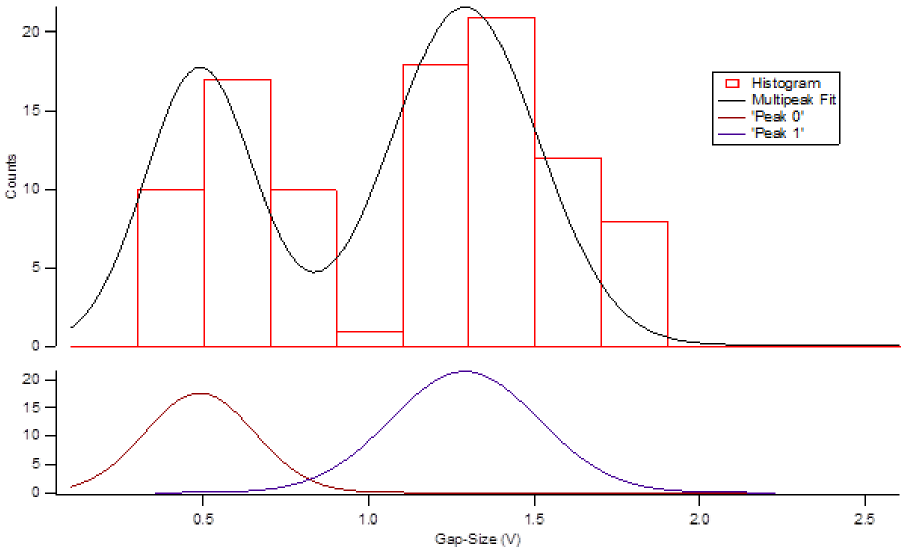

Figure 73 Histogram-Analysis of the single particle I/V-curves. Here the gap sizes are shown, the bin size is 0.2V. The curves show two distinct maxima. The multi peak fit gives two maxima: 1.29 V and 0.5 V. The 1.29 V maxima is the forward direction peak and the 0.5 V the backward direction peak as shown in **Figure 72**.

Effects of current stressing in clusters and single particles

The use of platin-iridium coated tips can increase oxidation rates through driving oxygen into the particle (Mugtasimov et al., 2011). The typical oxidation of a cobalt nanoparticle is governed by the Mott potential which moves the cobalt cations through the particle and an already existing shell to the surface, where they form the oxide (Gulbransen and Andrew, 1951) . Usually the oxidation happens through electron transfer from the metal to the oxygen. As the cobalt oxides are ionic, they will react to an applied voltage (Campbell, 1997) . Therefore, the applied voltage and the flowing current can be expected to cause a certain movement of atoms and ions in the particle and to heat the area underneath the tip. While in large clusters there are enough pathways for heat dissipation, due to the larger contact area, this is not the case for a single particle. Thus single particles will reach a higher temperature during the current flow from the tip to the particle. The change from CoO with a gap of 3.7 eV to Co_3O_4 (gap:1.3 eV) is expected in the temperature range of 400°C (Tompkins, 1981) . This temperature can easily be achieved if the transport of heat away from the nanoparticles is blocked or hindered (Dubi and Di Ventra, 2011). The control experiments on Co-films (thickness: 10 nm, Figure 77) did not show this reduction of the gap size during voltage sweeping which additionally supports this interpretation. A simple possible explanation is illustrated in Figure 74 where the pathways for heat dissipation in a single particle and in a cluster are sketched. For a single particle there is only the tip and the substrate available for heat exchange, while in a cluster the neighbouring particles can exchange heat also.

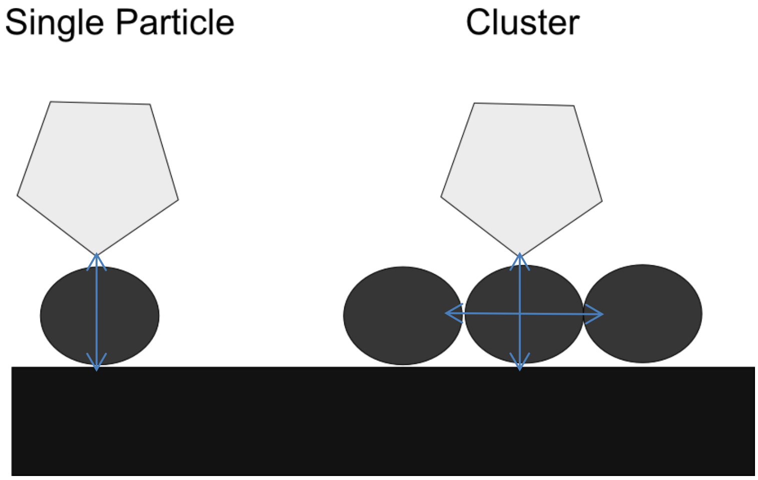

Figure 74 Simple explanation for the different heat channels of a single particle and a cluster. The single particle can only transfer heat to the HOPG and the tip, while in the cluster the particle can transfer heat to the neighbours also.

Dielectric breakdown

In order to further characterise the changes of the I-V curves observed during voltage sweeps on single particles, we measured highly resolved conductance maps prior to and after voltage sweeping. As shown by the resulting conductance maps in Figure 75 an obvious change in the local conductance on one single particle can be observed which was caused by the voltage sweeps.

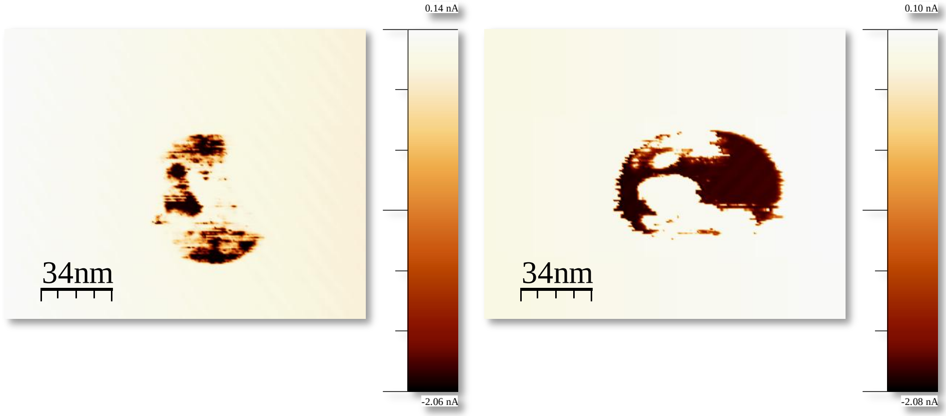

Figure 75 Conductance map of a single nanoparticle before (on the left side) and after (on the right side) several I-V measurements. A clear change of the local conductance can be observed, which can be attributed to ionic transport in the particle.

As outlined, this can be explained by the movement of ions in the particle, which is obviously not homogeneous. This finding is in agreement with the HR-TEM image which showed varying crystallographic orientations in the oxidic CoO-shell of the Co particles. The different regions of the oxygen crystal orientation visible in Figure 58 will cause a non-homogeneous local conductance so that different contacts between tip and particle and related ion movement can be expected. This indicates, that the soft breakdown in cobalt oxides, which has been also observed by other groups in thin films (Fu et al., 2005) and nanorods (Nagashima et al., 2011), is locally promoted by structural inhomogeneities at the particle surface.

Control experiments

In order to check the results a cobalt thin film (10 nm) on HOPG has been deposited. STM images and a STS curve have been obtained. In Figure 76 the measured topography is shown and in Figure 77 the STS curve is shown. The STS curve is averaged over ten measurements in order to reduce noise.

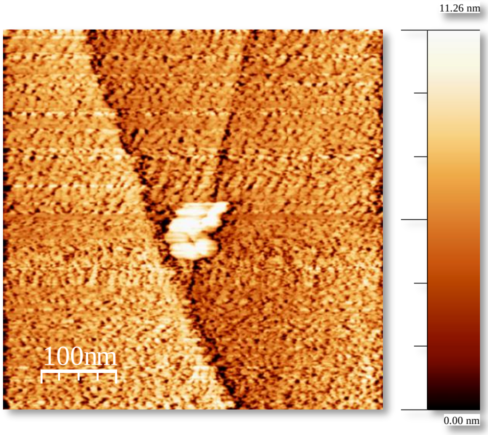

Figure 76 STM image of 10 nm cobalt thin film deposited on HOPG.

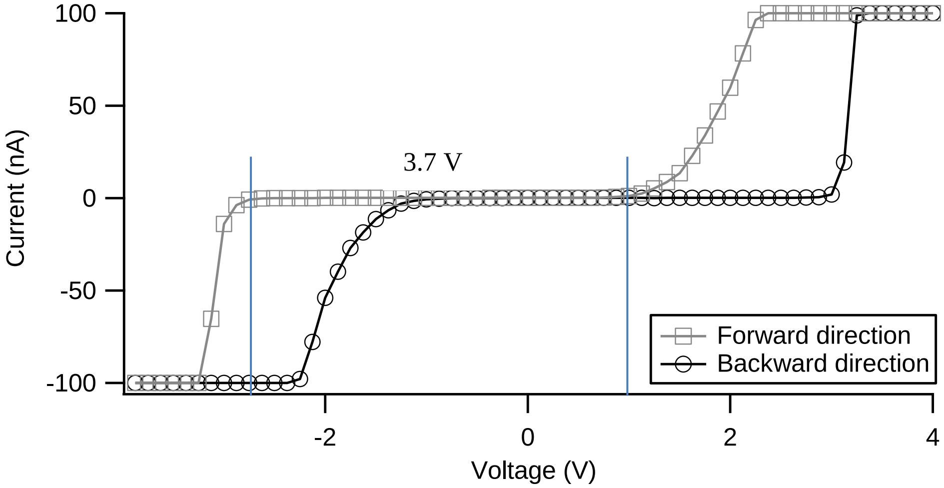

Figure 77 STS curve taken on the cobalt thin film. Ten curves are averaged. The 3.7 V gap is clearly visible. The forward direction (grey) and the backward direction (black) are shifted - resistive switching. The STM amplifier has a range of ±100 nA.

The STS curve clearly shows the gap as it has been observed in the I-V curves of the clusters, e.g. in Figure 68 . It also exhibits the resistive switching.

If the Co films are thicker than 10 nm, experiments with C-AFM show the expected 2.4 eV (Landolt-Börnstein, 1984) band gap of bulk cobalt oxide. These measurements confirm that under a certain thickness the band gap changes due to the surface volume ratio.

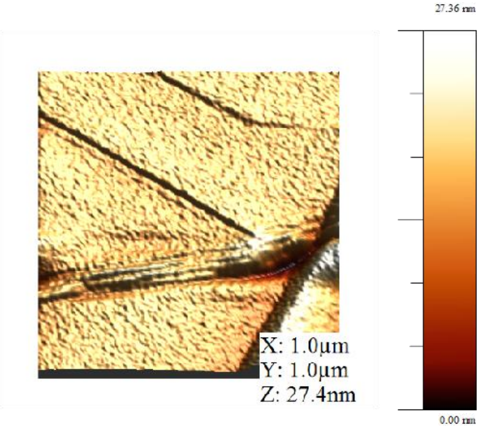

Figure 78 Conductive AFM measurement of a cobalt film on HOPG with at thickness beyond 10 nm.

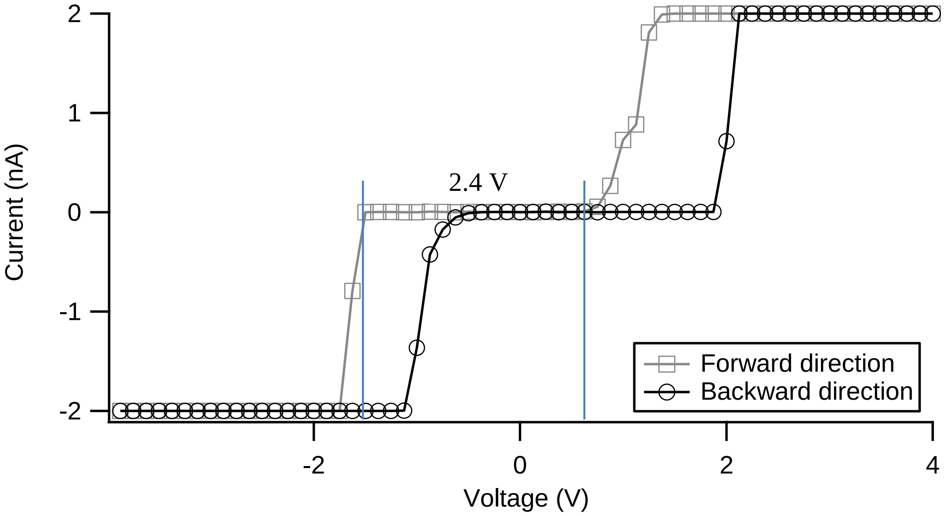

Figure 79 If the film thickness is high enough the band gap reverts to its bulk value of 2.4 eV.

Kelvin Force Probe Microscopy Of Nanoparticles On HOPG

Following the same route for the experiments as in C-AFM experiments firstly a clean HOPG sample has been investigated. In Figure 80 the results can be seen. Comparing with the results found by (Sommerhalter et al., 1999) a match of findings can be stated.

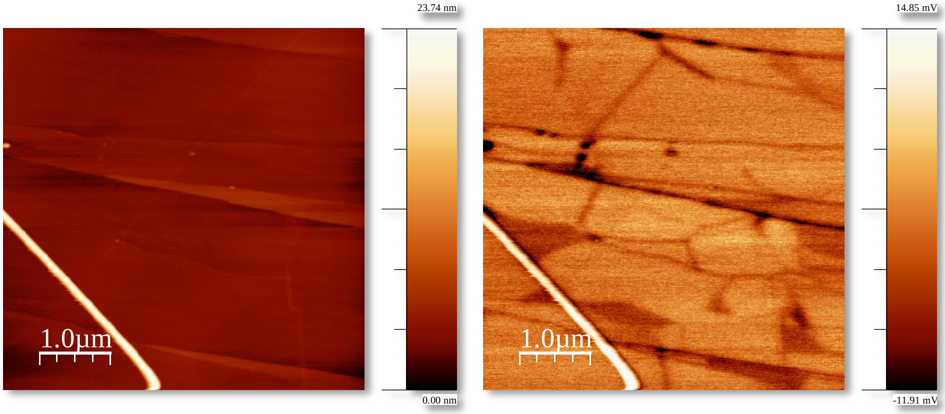

Figure 80 The topography is shown on the right side. On the left side the KFPM image is shown. The areas with equal work functions are clearly visible.

Cobalt nanoparticles have been deposited on the surface and the measurement can be seen in Figure 81. As expected the oxidised particles have higher electron repulsion than their surroundings (means a higher KFP signal). It is noteworthy that the HOPG pattern could not be identified but considering the scales and the surface sensitivity of KFPM this is not unexpected.

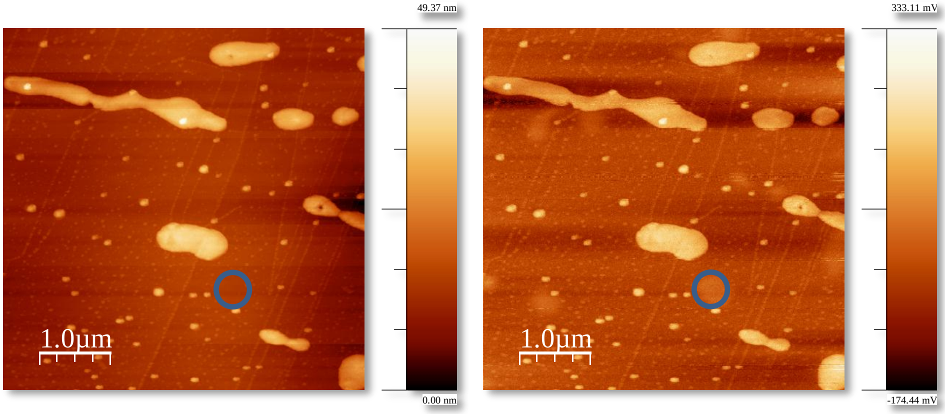

Figure 81 Magnetic nanoparticles on HOPG measured with KFPM technique. On the left is the topography and on the right side the potential image.

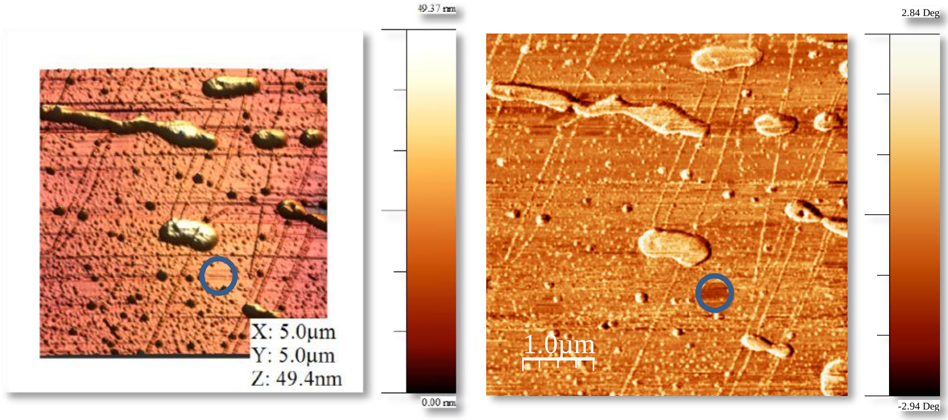

Figure 82 The 3D representation of the topography (on the left) and the phase image (on the right side) give a hint for the reason of the different work function measured at some places.

While most of the features correspond with the topographic image on the left side there are also areas where the work function is higher, which do not correspond to the topographic image. One of the areas is marked on the images in Figure 81 and Figure 82. These areas can be identified with the help of Figure 82 where the 3D representation and the phase image are shown. On the 3D image there are no features at those areas and the phase is different there. The reason for the areas with changed KFP- and phase signal cannot be identified. Because there is no topographic feature at these locations “buried” structures within the HOPG could be one possible source. Another possible source might be an uncovered surface of the HOPG, which is less likely considering that these areas are next to the particles.

Despite these structures it is remarkable that there are no strong KFP signal changes on the particles. In Figure 83 the contour plot with a discrete scale is shown. Comparing the topography with the KFP signal map one comes to the conclusion that there is not more than 20.5 millivolts (one colour) deviation for the particle cluster, which is less than would be expected for different oxides. Therefore the clusters are uniformly oxidised. This result underlines the previous findings and interpretations that the spinel gap is induced by the measurement.

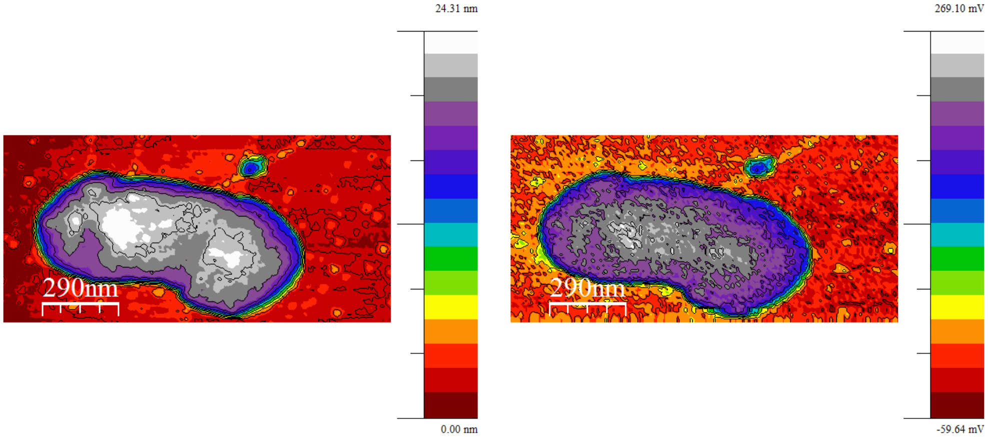

Figure 83 Comparison of the contour plots of the topography and the KFP signal. A change of colours in the KFP plot means a change of maximal 20.5 mV.

Summary And Conclusion

In this thesis it has been demonstrated that magnetic multilayer systems can be used as magnetic substrates for SPM applications and nanostructures composed of SMMs or magnetic nanoparticles and that they are accessible by several flavours of SPM (AFM, KPFM, C-AFM).

Magnetic multilayer systems covered with ultrathin MgO and with out-of-plane magnetisation have been prepared via sputtering and measured with STM/AFM/MFM. It has been proved that these systems exhibited the expected domain structures and that they are reasonable flat for SPM applications.

Single Molecule Magnets have been deposited on a substrate and measured with AFM and STM. Entities with the height of one molecule could be isolated and imaged.

Furthermore cobalt nanoparticles have been investigated with respect to their transport properties. Characteristic topographical features and current-voltage curves were observed with a striking difference between the resulting gap structure of particle clusters and single particles. A narrower gap structure found for single nanoparticles as compared to particle-clusters could be matched with the band gaps of cobalt oxide in rock salt (CoO) and spinel form (Co_3O_4). While the rock salt band gaps of 3.7 eV only occurred in the particle-clusters, the narrower gap of the spinel (1.3 eV) was frequently found for the single nanoparticles.

Another interesting point is that the resistive switching of cobalt oxide could be observed once again – even on a scale of 10 nm. Moreover, it seems even possible to switch the particles from one oxide to another.

The successful application of scanning probe methods to thin films, nanoparticles and nanostructures confirms that the imaginary machine introduced in the introduction can be built as the physics needed for the involved processes plays along.

The results found in this work can be used for further applications. Considering the current high interest in resistive switching (e.g. in RE-RAM) one can easily imagine a multitude of applications for cobalt nanoparticles in electric circuits. If one keeps in mind that not only the resistance changes, but also the magnetic behaviour, a combination between spintronics and the usually electron based electronics is thinkable. Both oxides are antiferromagnetic, but the Néel temperature for CoO is 290 K while the Néel temperature for Co_3O_4 is only 40 K (Gragnaniello et al., 2010). For technical applications this means one could switch off the antiferromagnetism with a current pulse (transition of the particle from CoO to Co_3O_4). In Figure 84 a sketch of a possible multipurpose system is made.

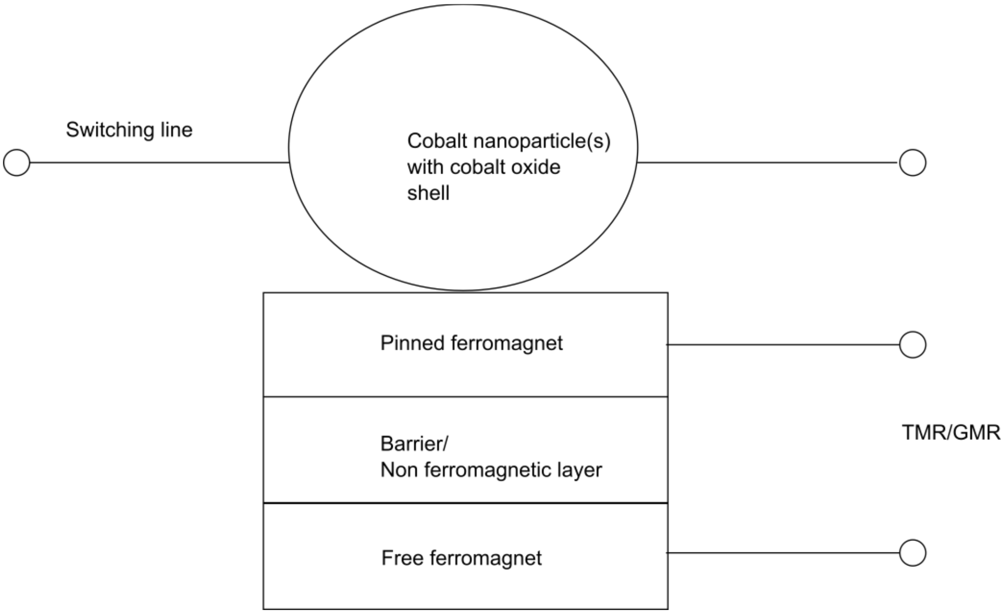

Figure 84 Proposed multipurpose system. Assuming pinning between a ferromagnetic layer and antiferromagnetic nanoparticles is achievable one could use such a system for resistive switching of the cobalt particle and for TMR/GMR systems with "off switch" for the pinning. Current lines, which are necessary for the magnetic field, have been omitted for clarity.

LITERATURE

Abramoff, M.D., Magalhaes, P.J., Ram, S.J., 2004. Image processing with ImageJ. Biophotonics international 11, 36-42.

Banerjee, S., Sardar, M., Gayathri, N., Tyagi, A., Raj, B., 2005. Conductivity landscape of highly oriented pyrolytic graphite surfaces containing ribbons and edges. Physical Review B 72, 1-7.

Banerjee, S., Sardar, M., Gayathri, N., Tyagi, A.K., Raj, B., 2006. Enhanced conductivity in graphene layers and at their edges. Applied Physics Letters 88, 062111.

Barnes, J.R., O'Schea, S.J., Welland, M.E., Kim, J.-Y., Evetts, J.E., Somekh, R.E., 1994. Magnetic force microscopy of Co-Pd multilayers with perpendicular anisotropy 76, 2974-2980.

Binnig, G., Quate, C.F., 1986. Atomic Force Microscope. Physical Review Letters 56, 930-933.

Campbell, C.T., 1997. Ultrathin metal films and particles on oxide surfaces: structural, electronic and chemisorptive properties. Surface Science Reports 27, 1-111.

Carcia, P.F., Meinhaldt, A.D., Suna, A., 1985. Perpendicular magnetic anisotropy in Pd/Co thin film layered structures. Applied Physics Letters 47, 178.

Cavallini, M., Biscarini, F., 2003. Nanostructuring Conjugated Materials by Lithographically Controlled Wetting. Nano Letters 3, 1269-1271.

Chappert, C., Dang, K., Beauvillain, P., Hurdequint, H., Renard, D., 1986. Ferromagnetic resonance studies of very thin cobalt films on a gold substrate. Physical Review B 34, 3192-3197.

Chen, C.J., 2007. Introduction to Scanning Tunneling Microscopy. Oxford University Press.

Daude, N., Jouanin, C., Gout, C., 1977. Electronic band structure of magnesium and calcium oxides. Physical Review B 15, 2399-2405.

Donzelli, O., Palmeri, D., Musa, L., Casoli, F., Albertini, F., Pareti, L., Turilli, G., 2003. Perpendicular magnetic anisotropy and stripe domains in ultrathin Co/Au sputtered multilayers. Journal of Applied Physics 93, 9908.

Draaisma, H.J.G., de Jonge, W.J.M., 1987. Magnetization curves of Pd/Co multilayers with perpendicular anisotropy. Journal of Applied Physics 62, 3318.

Dubi, Y., Di Ventra, M., 2011. Colloquium: Heat flow and thermoelectricity in atomic and molecular junctions. Review of Modern Physics 83, 131-156.

Faber, O. C., Jr.; Papell, S.S., 1968. On the influence of nonuniform magnetic fields on ferromagnetic colloidal sols. NASA-TN-D-4676.

Foster, A., Hofer, W., 2006. Scanning Probe Microscopy. Springer New York.

Foster, B., 2009. Focus on Microscopy: One Button and Two Heads-Mainstreaming AFM. American laboratory 41, 11-13.

Fu, L., Liu, Z., Liu, Y., Han, B., Hu, P., Cao, L., Zhu, D., 2005. Beaded Cobalt Oxide Nanoparticles along Carbon Nanotubes: Towards More Highly Integrated Electronic Devices. Advanced Materials 17, 217-221.

Gan, Y., 2009. Atomic and subnanometer resolution in ambient conditions by atomic force microscopy. Surface Science Reports 64, 99-121.

García, R., 2002. Dynamic atomic force microscopy methods. Surface Science Reports 47, 197-301.

Gatteschi, D., 1994. Molecular magnetism: A basis for new materials. ADVANCED MATERIALS-DEERFIELD BEACH- 6, 635–635.

Glaser, T., Heidemeier, M., Weyhermüller, T., Hoffmann, R.-D., Rupp, H., Müller, P., 2006. Eigenschaftsorientiertes rationales Design von Einzelmolekülmagneten: ein aus drei molekularen Bausteinen aufgebauter Mn6Cr-Komplex mitC3-Symmetrie und einem Spingrundzustand vonSt=21/2. Angewandte Chemie 118, 6179-6183.

Gomar-Nadal, E., Puigmartí-Luis, J., Amabilino, D.B., 2008. Assembly of functional molecular nanostructures on surfaces. Chemical Society reviews 37, 490-504.

Gradmann, U., Müller, J., 1968. Flat Ferromagnetic, Epitaxial 48Ni/52Fe(111) Films of few Atomic Layers. Physica Status Solidi (b) 27, 313-324.

Gragnaniello, L., Agnoli, S., Parteder, G., Barolo, A., Bondino, F., Allegretti, F., Surnev, S., Granozzi, G., Netzer, F.P., 2010. Cobalt oxide nanolayers on Pd(100): The thickness-dependent structural evolution. Surface Science 604, 2002-2011.

Grote, J.-P., 2010. Senkrechte Magnetisierung von Co/Au Schichtsystemen.

Gulbransen, E.A., Andrew, K.F., 1951. The Kinetics of the Oxidation of Cobalt. Journal of The Electrochemical Society 98, 241-251.

Guo, D., Hou, S., Zhang, G., Xue, Z., 2006. Conductance fluctuation and degeneracy in nanocontact between a conductive AFM tip and a granular surface under small-load conditions. Applied Surface Science 252, 5149-5157.

Harding, C., Kunz, S., Habibour, V., Teslenko, V., Arenz, M., Heiz, U., 2008. Dual pulsed-beam controlled mole fraction studies of the catalytic oxidation of CO on supported Pd nanocatalysts. Journal of Catalysis 255, 234-240.

Hartmann, U., 1999. MAGNETIC FORCE MICROSCOPY. Annual Review of Materials Science 29, 53-87.

Hayakawa, J., Ikeda, S., Lee, Y.M., Matsukura, F., Ohno, H., 2006. Effect of high annealing temperature on giant tunnel magnetoresistance ratio of CoFeB⁄MgO⁄CoFeB magnetic tunnel junctions. Applied Physics Letters 89, 232510.

Heidemeier, M., 2006. Anorganische Chemie Koordinationschemie m-phenylenverbrückter Übergangsmetallkomplexe und deren Verwendung in der gezielten Synthese von Einzelmolekülmagneten.

Ho, C.-C., Hsieh, T.-W., Kung, H.-H., Juan, W.-T., Lin, K.-H., Lee, W.-L., 2010. Reduced saturation magnetization in cobalt antidot thin films prepared by polyethylene oxide-assisted self-assembly of polystyrene nanospheres. Applied Physics Letters 96, 122504.

Horcas, I., Fernández, R., Gómez-Rodríguez, J.M., Colchero, J., Gómez-Herrero, J., Baro, A.M., 2007. WSXM: a software for scanning probe microscopy and a tool for nanotechnology. The Review of scientific instruments 78, 013705.

Hosokawa, M., Nogi, N., Naito, M., Yokoyama, T., 2007. Nanoparticle Technology Handbook. Elsevier, Amsterdam.

Inoue, I., Yasuda, S., Akinaga, H., Takagi, H., 2008. Nonpolar resistance switching of metal/binary-transition-metal oxides/metal sandwiches: Homogeneous/inhomogeneous transition of current distribution. Physical Review B 77, 1-7.

Israelachvili, J.N., 2010. Intermolecular and Surface Forces. Academic Press; 3rd edition

Jackson, J.D., 1998. Classical Electrodynamics Third Edition, American Journal of Physics. Wiley.

Jia, J.-F., Ma, X., Chen, X., Sakurai, T., Xue, Q.-K., 2011. STM and MBE: one of the best combinations. Journal of Physics D: Applied Physics 44, 464007.

Johnson, M., Bloemen, P., Den Broeder, F., De Vries, J., 1996. Magnetic anisotropy in metallic multilayers. Reports on Progress in Physics 59, 1409–1458.

Kelvin, Lord, 1898. Contact electricity of metals. Philos. Mag. 46, 82–120.

Kugler, Z., Drewello, V., Schäfers, M., Schmalhorst, J., Reiss, G., Thomas, A., 2011. Temperature and bias voltage dependence of Co/Pd multilayer-based magnetic tunnel junctions with perpendicular magnetic anisotropy. Journal of Magnetism and Magnetic Materials 323, 198-201.

Landolt-Börnstein, 1984. Physics of NonTetrahedrally Bonded Binary Components,, New Series. ed. Springer, New York,.

Leach, R.K., Boyd, R., Burke, T., Danzebrink, H.-U., Dirscherl, K., Dziomba, T., Gee, M., Koenders, L., Morazzani, V., Pidduck, A., Roy, D., Unger, W.E.S., Yacoot, A., 2011. The European nanometrology landscape. Nanotechnology 22, 062001.

Leuenberger, M.N., Loss, D., 2001. Quantum computing in molecular magnets. Nature 410, 789-93.

Liu, J., Pan, M., Spinnler, G.E., 1992. Electron Microscopy Characterization Of Epitaxial Growth Of Ag Deposited On Mgo Microcubes. MRS Proceedings 295.

Martin, Y., Williams, C.C., Wickramasinghe, H.K., 1987. Atomic force microscope–force mapping and profiling on a sub 100-A° scale. Journal of Applied Physics 61, 4723.

Mativetsky, J.M., Palma, M., Samorì, P., 2008. Exploring Electronic Transport in Molecular Junctions by Conducting Atomic Force Microscopy. Anion Sensing 157-202.

Mattox, D.M., 1989. Particle bombardment effects on thin-film deposition: A review. Journal of Vacuum Science & Technology A: Vacuum, Surfaces, and Films 7, 1105.

Mattox, D.M., 2003. The Foundations of Vacuum Coating Technology, Coating. NOYES PUBLICATIONS.

Melitz, W., Shen, J., Kummel, A.C., Lee, S., 2011. Kelvin probe force microscopy and its application. Surface Science Reports 66, 1-27.

Mironov, V.L., 2004. Fundamentals of the scanning probe microscopy, Microscopy.

Mugtasimov, A.V., Peskov, N.V., Pankina, G.V., Chernavskii, P.A., Lunin, V.V., 2011. The kinetics of low-temperature oxidation of cobalt nanoparticles in porous media. Russian Journal of Physical Chemistry A 85, 217-224.

Nagashima, K., Yanagida, T., Oka, K., Kanai, M., Klamchuen, A., Kim, J.-S., Park, B.H., Kawai, T., 2011. Intrinsic mechanisms of memristive switching. Nano letters 11, 2114-8.

Nečas, D., Klapetek, P., 2011. Gwyddion: an open-source software for SPM data analysis. Central European Journal of Physics 10, 181-188.

Nilius, N., 2009. Properties of oxide thin films and their adsorption behavior studied by scanning tunneling microscopy and conductance spectroscopy. Surface Science Reports 64, 595-659.

Nonnenmacher, M., O'Boyle, M.P., Wickramasinghe, H.K., 1991. Kelvin probe force microscopy. Applied Physics Letters 58, 2921.

Nowak, D.B., Lawrence, a J., Dzegede, Z.K., Hiester, J.C., Kim, C., Sánchez, E.J., 2011. Field programmable gate array based reconfigurable scanning probe/optical microscope. The Review of scientific instruments 82, 103701.

Ohring, M., 2002. Materials Science of Thin Films. Elsevier.

Powell, C.., Jablonski, A., Tilinin, I.., Tanuma, S., Penn, D.., 1999. Surface sensitivity of Auger-electron spectroscopy and X-ray photoelectron spectroscopy. Journal of Electron Spectroscopy and Related Phenomena 98-99, 1-15.

Puntes, V.F., Krishnan, K.M., Alivisatos, A.P., 2001. Colloidal Nanocrystal Shape and Size Control: The Case of Cobalt. Science 291, 2115-2117.

Reiss, G., Hütten, A., 2005. Magnetic nanoparticles: applications beyond data storage. Nature materials 4, 725-6.

Rossnagel, S., Cuomo, J., Westwood, W., 1990. Handbook of plasma processing technology. Noyes Publication.

Rushforth, a. W., Main, P.C., Gallagher, B.L., Marrows, C.H., Hickey, B.J., Dahlberg, E.D., Eames, P., 2001. Magnetic force microscopy studies of the domain structure of Co/Pd multilayers in a magnetic field. Journal of Applied Physics 89, 7534.

Russ, J., 2011. The Image Processing Handbook, Sixth Edition. CRC Press.

Sanvito, S., Rocha, A.R., 2006. Molecular-Spintronics: the art of driving spin through molecules. Molecules.

Schintke, S., Messerli, S., Pivetta, M., Patthey, F., Libioulle, L., Stengel, M., De Vita, A., Schneider, W.-D., 2001. Insulator at the Ultrathin Limit: MgO on Ag(001). Physical Review Letters 87, 2-5.

Schmitz, I., Schreiner, M., Friedbacher, G., Grasserbauer, M., 1997. Phase imaging as an extension to tapping mode AFM for the identification of material properties on humidity-sensitive surfaces. Imaging 4332.

Sommerhalter, C., Matthes, T.W., Glatzel, T., Jäger-Waldau, A., Lux-Steiner, M.C., 1999. High-sensitivity quantitative Kelvin probe microscopy by noncontact ultra-high-vacuum atomic force microscopy. Applied Physics Letters 75, 286.

Stiles, M.D., 2006. Exchange Coupling in Magnetic Multilayers. Contemporary Concepts of Condensed Matter Science 1, 51–76.

Thomas, A., Drewello, V., Schäfers, M., Weddemann, A., Reiss, G., Eilers, G., Münzenberg, M., Thiel, K., Seibt, M., 2008. Direct imaging of the structural change generated by dielectric breakdown in MgO based magnetic tunnel junctions. Applied Physics Letters 93, 152508.

Thornton, J.A., 1986. The microstructure of sputter deposited coatings. Journal of Vacuum Science and Technology 3058-3065.

Tichý, J., Erhart, J., Kittinger, E., Přívratská, J., 2010. Fundamentals of Piezoelectric Sensorics. Springer Berlin Heidelberg, Berlin, Heidelberg.

Tompkins, H.G., 1981. Summary Abstract: Oxidation of cobalt in air from room temperature to 467 °C. Journal of Vacuum Science and Technology 18, 408.

Vaz, C. a F., Bland, J. a C., Lauhoff, G., 2008. Magnetism in ultrathin film structures. Reports on Progress in Physics 71, 056501.

Venables, J., Spiller, G., Hanbucken, M., 1984. Nucleation and growth of thin films. Reports on Progress in Physics 47, 399–459.

Weddemann, A., Ennen, I., Regtmeier, A., Albon, C., Wolff, A., Eckstädt, K., Mill, N., Peter, M.K.-H., Mattay, J., Plattner, C., Sewald, N., Hütten, A., 2010. Review and outlook: from single nanoparticles to self-assembled monolayers and granular GMR sensors. Beilstein Journal of Nanotechnology 1, 75-93.

Wiesendanger, R., 1995. Scanning Probe Microscopy and Spectroscopy: Methods and applications, Measurement Science and Technology. Cambridge.

Yamamoto, H., Tanaka, S., Hirao, K., 2004. Nanostructure and Optical Nonlinearity of Cobalt Oxide Thin Films. Journal of the Ceramic Society of Japan 112, S876–S880.

Yuasa, S., 2008. Giant Tunneling Magnetoresistance in MgO-Based Magnetic Tunnel Junctions. Journal of the Physical Society of Japan 77, 031001.

Zahl, P., Wagner, T., Möller, R., Klust, A., 2010. Open source scanning probe microscopy control software package GXSM. Journal of Vacuum Science & Technology B: Microelectronics and Nanometer Structures 28, C4E39.

Zutic, I., Fabian, J., Sarma, S.D., 2004. Spintronics: Fundamentals and applications. Computational Materials Science 323-410.

APPENDIX

Table of forces

Type of Force	Subclasses and Alternative Names	Main Features
	Attractive	
van der Waals	Dispersion force (v & s) Induced dipole force (v & s) Casimir force (v & s)	Ubiquitous force, occurs both in vacuum and in liquids
Electrostatic	Coulombic force (v & s) Ionic bond (v) Hydrogen bond (v) Charge–transfer interaction (v & s) “Harpooning” interaction (v)	Strong, long-ranged force arising in polar solvents; requires surface charging or charge-separation mechanism
Quantum mechanical	Covalent bond (v) Metallic bond (v) Exchange interaction (v)	Strong short-ranged forces responsible for contact binding of crystalline surfaces
Hydrophobic	Attractive hydration force (s)	Strong, apparently long-ranged force; origin not yet Understood
Ion–correlation	van der Waals force of polarizable ions (s)	Requires mobile charges on surfaces in a polar solvent
Solvation	Oscillatory force (s) Depletion force (s)	The oscillatory force generally alternates between attraction and repulsion; mainly entropic in origin
Specific binding	“Lock and key” binding (v & s) Receptor–ligand interaction (s) Antibody–antigen interaction (s)	Subtle combination of different noncovalent forces giving rise to highly specific binding; main “recognition” mechanism of biological systems.
	Repulsive	

Quantum mechanical	Hard-core (v) Steric repulsion (v) Born repulsion (v)	Forces stabilizing attractive covalent and ionic binding forces, effectively determine molecular size and shape
Van der Waals	Van der Waals disjoining pressure (v)	Arises only between dissimilar bodies interacting in a medium
Electrostatic		Arises for certain constrained surface charge distributions
Solvation	Oscillatory solvation force (s) Structural force (s) Hydration force (s)	Monotonically repulsive forces, believed to arise when solvent molecules bind strongly to surfaces
Entropic	Osmotic repulsion (s) Double-layer force (s) Thermal fluctuation force (s) Steric polymer repulsion (s) Undulation force (s) Protrusion force (s)	Forces due to confinement of molecular or ionic species between two approaching surfaces. Requires a mechanism which keeps trapped species between the surfaces
	Dynamic Interactions	
Nonequilibrium	Hydrodynamic forces (s) Viscous forces (s) Friction forces (v+s) Lubrication forces (s)	Energy-dissipating forces occurring during relative motions of surfaces or bodies.

Note: v, Applies only to interactions in *vacuum*; s, applies only to interactions in *solution*, or to surfaces separated by a liquid; v & s, applies to interactions occurring both in vacuum and in solution

Taken from:(Israelachvili, 2011)

Important parameters for piezoelectronics

Parameter	Meaning
Curie point	The piezoelectric ceramics are ferroelectric materials – above the Curie point the ferroelectricity is lost and the piezoelectric property is degraded above such a temperature. Piezoelectric should only be used in their specified operation temperature.
Temperature dependence of piezoelectric coefficients	The variation of the piezoelectric coefficients through temperature is strongly material dependent. The material has to be chosen application dependent.
Mechanical quality number	This number provides a measure of the internal mechanical energy loss of the material. A large number indicates a small loss and is therefore desired.
Coupling constants	These constants give a measure of the effectiveness of the piezoelectric material. k equals the electrical energy converted to mechanical energy divided by the input electrical energy The typical range is from 0.5 to 0.7.
Aging	Due to relaxation the materials lose their piezoelectric properties. The aging follows a logarithmic law.

Common scanner designs

The classical tripod scanner

The first STM built by Binnig and Rohrer was based on the tripod design. The displacements along the x,y,z axis are actuated by three independent PZT transducers. The transducers were made of rectangular pieces of PZT, metallized on two sides. For a 20 mm long and 2 mm thick piezo one will find a resonance frequency of 3.3 kHz, which is quite low and therefore needs good vibrational isolation.

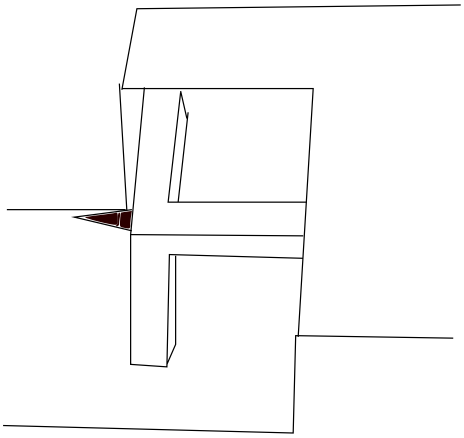

Modern tripod scanner

An example modern tripod design uses a tripod in order to move the probe over the sample. The piezos are separated and the z-scanner is close to the sample. The setup is able to scan large areas up to 130 µm and was invented by Topometrix.

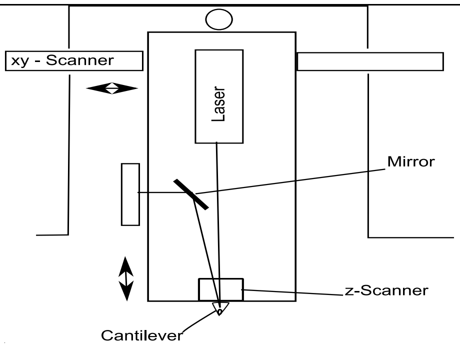

Tube scanner

The tube scanner has become the most used concept and has also been used in this work. The scanner has high piezo constants as well as high resonance frequencies. The tube scanner has been invented by Binnig and Smith in 1986. The

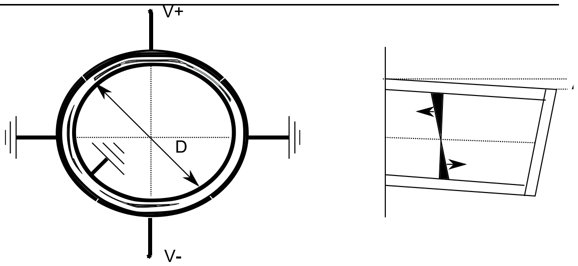

The working principle of the deflection in a four quadrant tube scanner. The same but on side inversed voltage is applied at the y easiest way to implement a tube scanner is to segment four segments on the outside of the tube for x-y movement and use the inner electrode as piezo for the z-direction.

One of the problems with this design is that the motions driven by the x, y, and z voltages are nonlinear and not precisely orthogonal. This must be corrected by programming in the control system. Substantial improvement can be achieved by using bipolar, symmetric x and y voltages, and by placing the tip at the center of the tube. A $+V_x$, and $-V_x$ voltages are applied on the opposite x quadrants, whereas a $+V_y$ and $-V_y$ voltages are applied on the opposite y quadrants.

electrodes of the scanner, while the x, z electrodes are grounded. A pressure is generated in the upper quadrant, and a tension is generated in the lower quadrant. The torque at every cross section in B sums up to zero, whenever the strain and tension are in equilibrium.

Decoupled scanner

A decoupled scanner has totally independent movement of xy- and z- scanners. This concept has been introduced by Park Systems and its advantages are that it eliminates the scanner bow and that non-contact modes can be implemented easily. This concept is now widely used by many manufacturers.

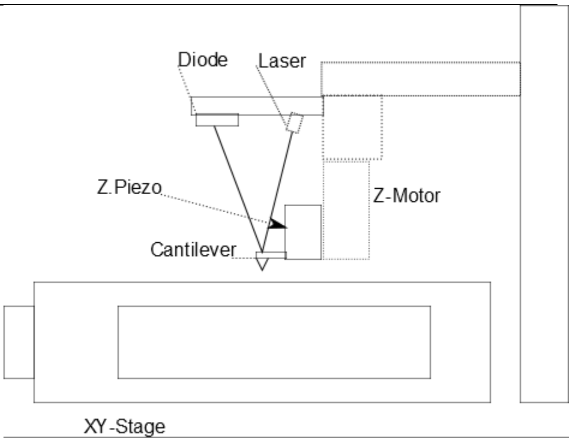

Besocke Beetle design

The beetle design has been invented by K. Besocke and is based on tube piezos. This design enables variable temperature measurements as it decouples the tip from the sample. The main advantage of this approach is thermal drift stability and a small mechanical loop. If one uses a sample holder with inclined planes for every leg, the approach can be done with short pulses to the piezo legs - the tip is “walked” into contact.

This design is an example of inertial stepper designs.

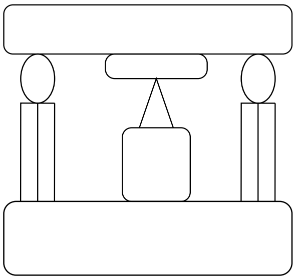

Beetle walker design. Three legs consisting of segmented piezo tubes “walk” the tip over the sample. The z-piezo is underneath the tip holder.

Additional designs

There are several other proposed designs, e.g. an unimorph disk scanner, a bimorph pizo based design, an inchworm based design or other piezo driven motor based designs.

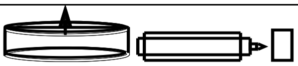

Common methods for image treatment

Method	How it works and what it is for
Plane subtraction	A 2D-Plane is subtracted from the image. This can correct mal alignments between probe and sample. Planes can be subtracted globally or local.
Flatten	Due to drift in the z-direction between two lines, SPM images can have a low frequency noise in Y direction. This can be treated, using a polynomial line fit, subtracting the line to line difference. The simplest flatten function is just to subtract a constant, the average of the line. For scanner bows, a parabola fit is often useful. In some occasions third order fits can achieve the desired effect. The chosen flatten function can be responsible for roughness differences or shadow effects. Most of the programs offer flattening along paths or flattening discarding regions. These functions are useful to avoid shadow effects, e.g. if there is a single nanoparticle on a flat surface.
Erase\average lines	Sometimes single lines in a measurement are corrupted in an otherwise good looking image. Those lines are just artifacts which do not contribute to the general understanding and often they destroy the image scaling. For better representation of the relevant data it is sometimes helpful to find an average of the lines next to the line in question and the line itself or to erase such lines.
Crop and split	It is often only a part of an image which contains the data of interest, therefore crop and split functions are useful tools in order to visualize a region of interest, without distracting the viewer with unneeded information.
LUT editing/manipulation	The lookup tables (LUT) colorize the data height dependent. The tables do not alter the data. They only change the appearance of the presentation. Parameters that can be changed are contrast, brightness and scaling of the image.If the scaling is changed, the image data is altered. Another process to visualize features on the SPM image is equalizing the height dependence. Equalizing changes

	the height scale.
2D-Correlation	Two correlations are usually probed: **Self-correlation**, which is defined by a shift K_x and K_y of the original image matrix from the image center multiplied with a sum over the image point. The new resulting image $G(K_x, K_y) = \sum f(x,y) \cdot f(x + K_x, y + K_y)$ is then a measure of how different the two images are. The more similar the image and the shifted image are, the higher the value of the self-correlation. The highest value is obtained at the center of the image (where K_x and K_y are zero) and any periodicity in the original image will be visible as a periodic pattern. **Cross-correlation**, which is defined as $G(K_x, K_y) = \sum g(x,y) \cdot f(x + K_x, y + K_y)$ where g and f represent two image matrices.
2D-FFT	A two dimensional Fast-Fourier transformation makes it possible to detect regular patterns on an image. It is defined on a complex function h(x,y) as $H(n_1, n_2) = \sum_{y=0}^{N_2-1} \sum_{x=0}^{N_1-1} epx\left(\frac{2\pi i n_2 y}{N_2}\right) \exp\left(\frac{2\pi i n_1 x}{N_2}\right) h(x,y)$ The resulting image can then be analyzed with respect to the distances between the regular entities and their ordering on the original images. An example is a STM image of HOPG, the Fourier image reveals the hexagonal ordering and the interatomic distance.
2D-Filter	Image distortions caused by measurement artifacts and hidden features in an image can be enhanced or suppressed by two dimensional filtering, e. g. high frequency distortions can be treated with a lowpass filter. 2D-Filter usually reduce the resolution of the image as they work on windows of several pixel.

Image Math	As an image is represented by a two dimensional matrix, matrix operations (rotate, mirror, inverse, multiply,add, subtract) can be applied for image corrections or modifications.
Image Statistics	A typical image with a 512x512 resolution has 262144 points in total. Therefore a vast amount of statistical analysis methods can be applied, e.g. roughness analysis, grain size analysis, etc. Some commonly reported values to quantify the **height statistics** are: **Root Mean Square** This is the standard deviation of the height distribution: $R_q = \sqrt{\frac{1}{A}\iint_A h^2(x,y)dxdy}$ **Arithmetic Mean** The arithmetic mean is the mean surface height or the first moment of distribution: $R_a = \frac{1}{A}\int_A \lvert h(x,y)\rvert dxdy$ **Skewness** The skewness describes the third statistical moment, qualifying the symmetry of distribution: $R_{sk} = \frac{1}{R_q^3}\left[\frac{1}{A}\iint_A h^3(x,y)dxdy\right]$ **Kurtosis** The kurtosis is the fourth statistical moment, describing the flatness of distribution: $R_{ku} = \frac{1}{R_q^4}\left[\frac{1}{A}\iint_A h^4(x,y)dxdy\right]$ **Grain Analysis** The methods applied can be found in "Theoretical analysis of the atomic force microscopy characterization of columnar thin films" by P. Klapetek, I. Ohlídal *Ultramicroscopy*, **94 (19-29), 2003**

The used measurement software

The measurement software is the Nanoscope 6.13r1 software for all AFM applications and the 5.31r1 for STM measurements. In Figure 85 is a screenshot of the software during a measurement.

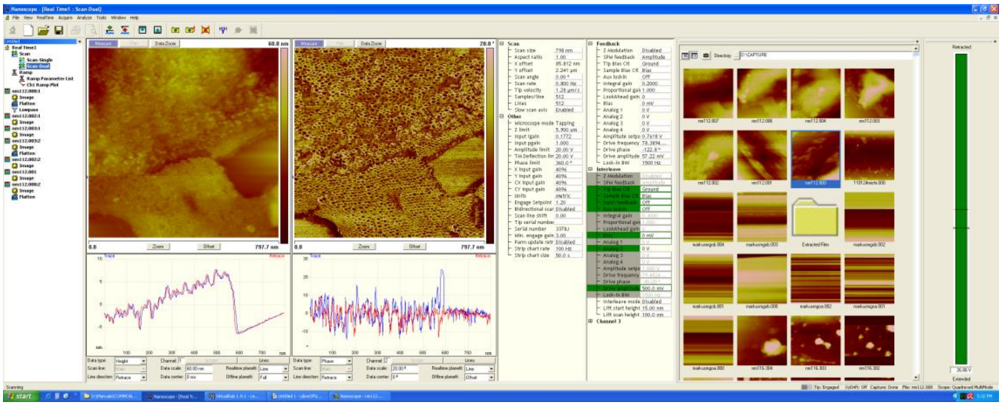

Figure 85 Nanoscope 6.13r1 software during a tapping mode measurement of nanoparticles.

The software has a realtime mode and an offline mode. In the offline mode image analysis with the build in analysis tool can be done.
For the STM measurements it is mandatory to use the 5.31r1 software as the STM head is connected to the universal bipotentiostat, which is only adressable from the 5.31r1 software. Actually the STM is just a subfunction of the SECPM mode and therefore the parameter names can be a little bit confusing.

The point and shoot mode

For the transport measurements the bias voltage has been ramped at certain spots on an image. In the point and shoot mode, an image is acquired first and then spots on that image can be marked for the ramping operation. The problem in an open loop system is the drift that happens between the ramping and the image acquisition. Therefore the positions are only approximately correct.

In Figure 86 the typical appearance of measured spots on the image opened in Nanoscope Analysis 1.4 is demonstrated. The spots can be switched on (red) and off (white) for further analysis.

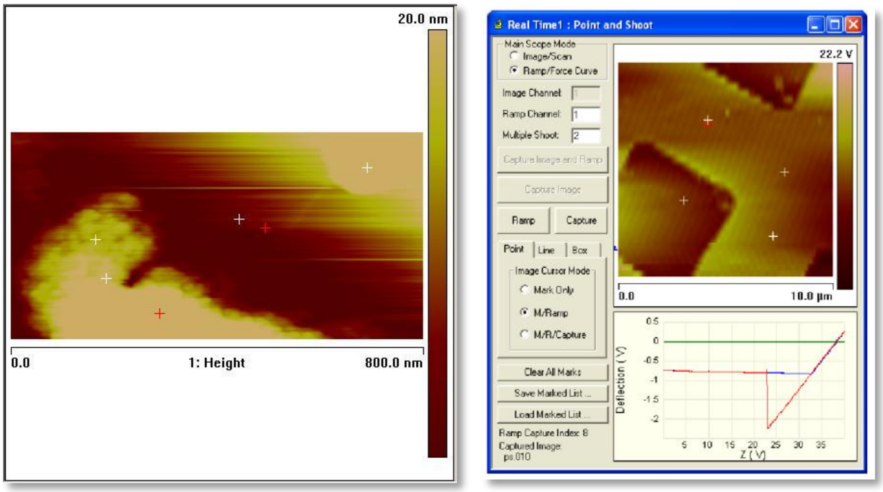

Main Scope Mode
○ Image/Scan
● Ramp/Force Curve

Image Channel: 1
Ramp Channel: 1
Multiple Shoot: 2

Image Cursor Mode
○ Mark Only
● M/Ramp
○ M/R/Capture

Ramp Capture Index: 8
Captured Image: ps.010

Figure 86 Image with marked spots for measurements. Curves could be acquired on the particles, close by the particles and on the substrate (On the left). On the right side is the point and shoot view (taken from the manual, courtesy of Bruker).

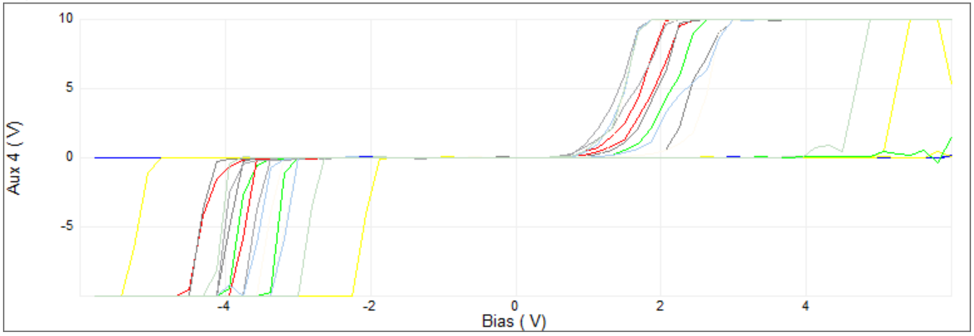

Figure 87 Obtained curves at different points on a particle cluster. Contact instabilities make high numbers of repetition of measurements necessary. The drift in the open loop system makes it obligatory to reduce the amount of measurements at one spot.

AFM images of molecules measured in Erlangen

Due to cooperation with Erlangen AFM measurements of single molecule magnets on the CoAu multilayer systems have been performed. The results correspond with my measurements.

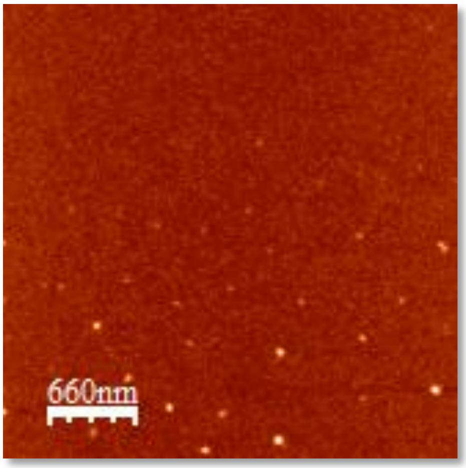

Figure 88 Survey of SMM measured on CoAu multilayer systems in Erlangen by M. Enzelberger.

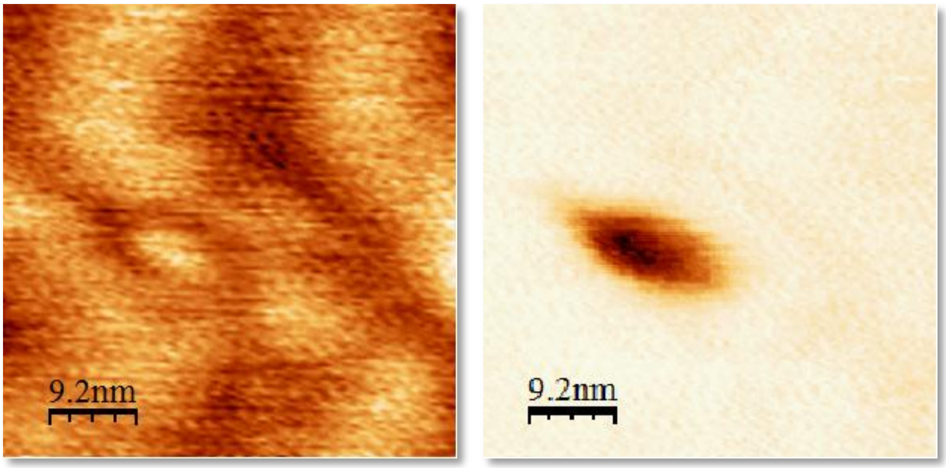

Figure 89 Close up on one entity with size of a single molecule. The same phase response as in the images on page 73 has been observed.

STM images of molecules?

Due to the difficulties to identify the molecules the here shown images give only a hint of how the molecules might look in STM images. The shape however does correspond with the AFM images, showing the same ellipsoidal form.

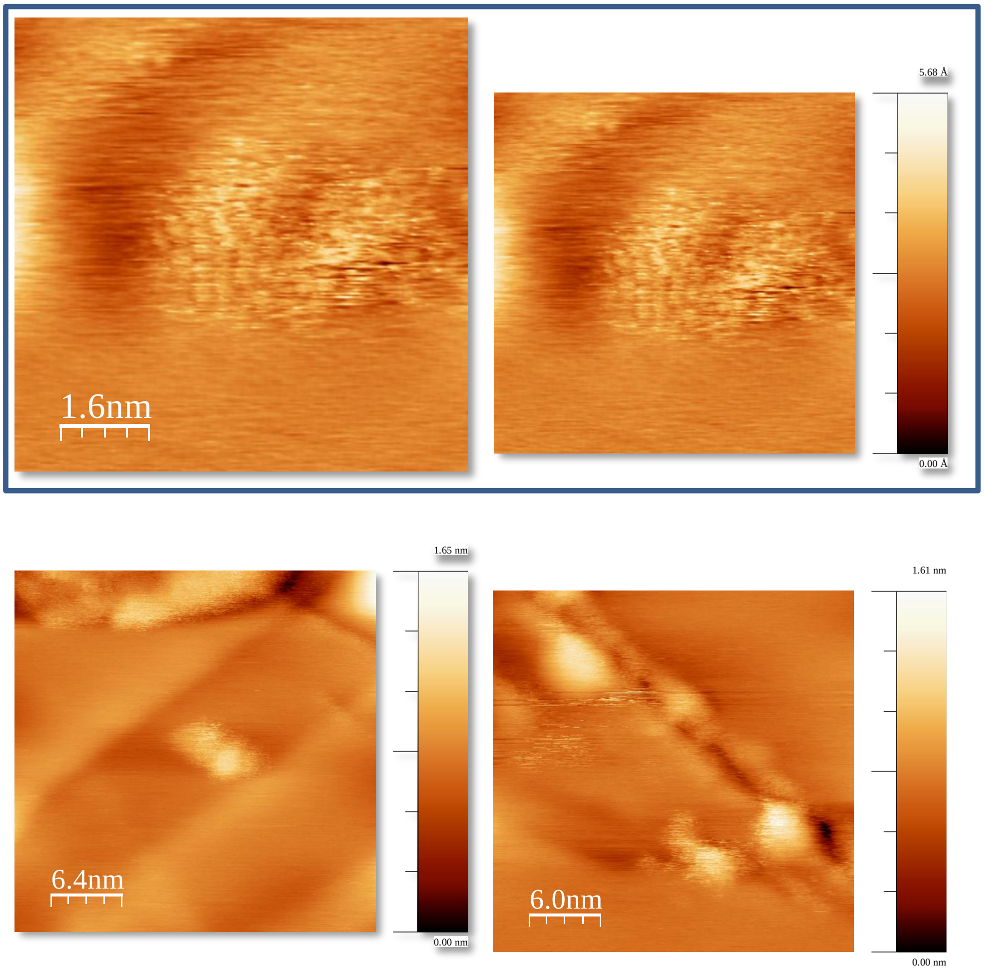

Figure 90 STM images of “molecules” on HOPG. The upper image is the topography image and its 3D representation. The lower images are just demonstrating that those entities can be found more than once.

Nanoparticles on edges

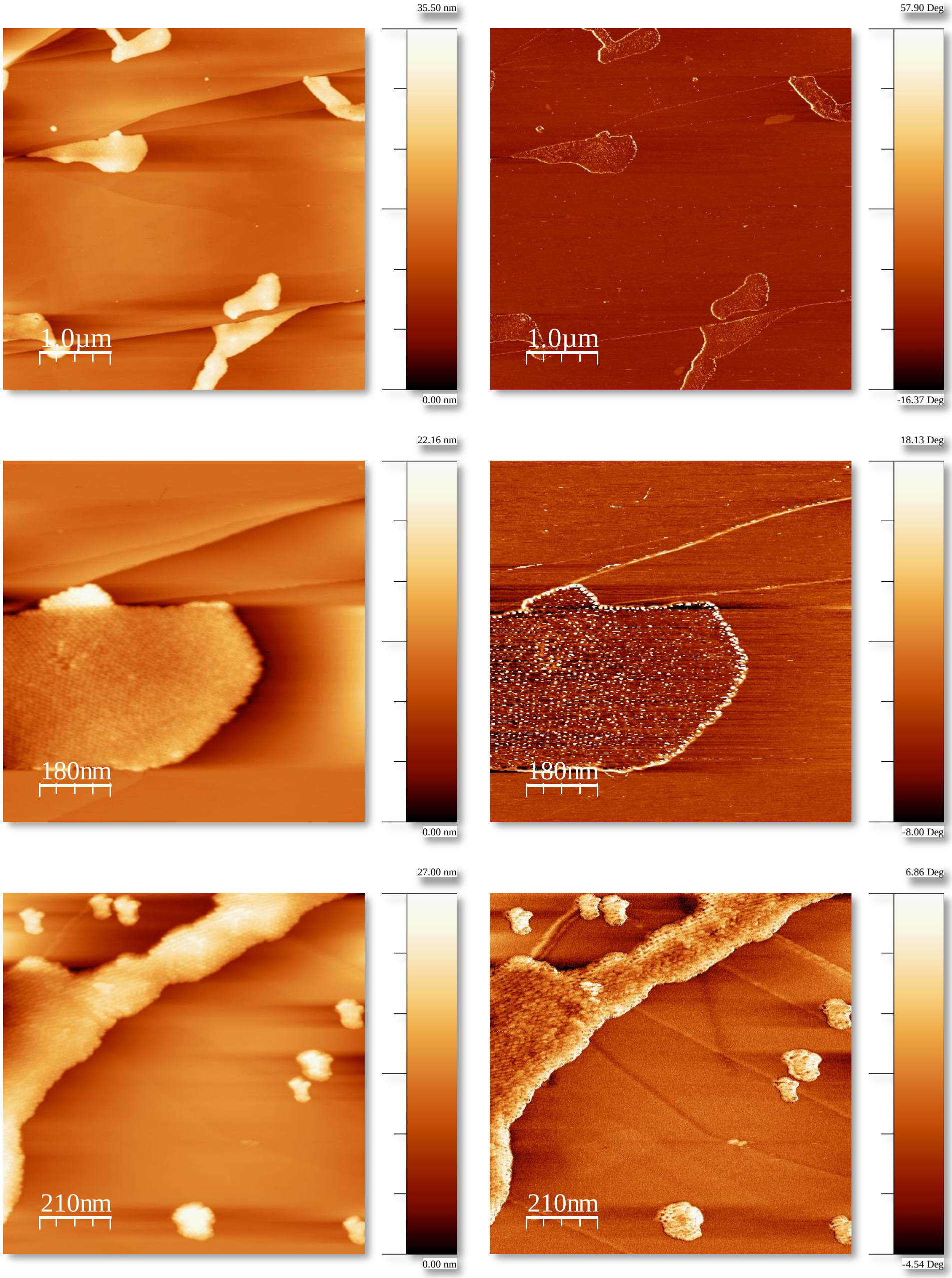

Figure 91 These are just some more images demonstrating how the clusters nulceate at or nearby HOPG plane edges.

Map of I-V curves

The following PowerPoint slides illustrate typical locations for the I-V curves.

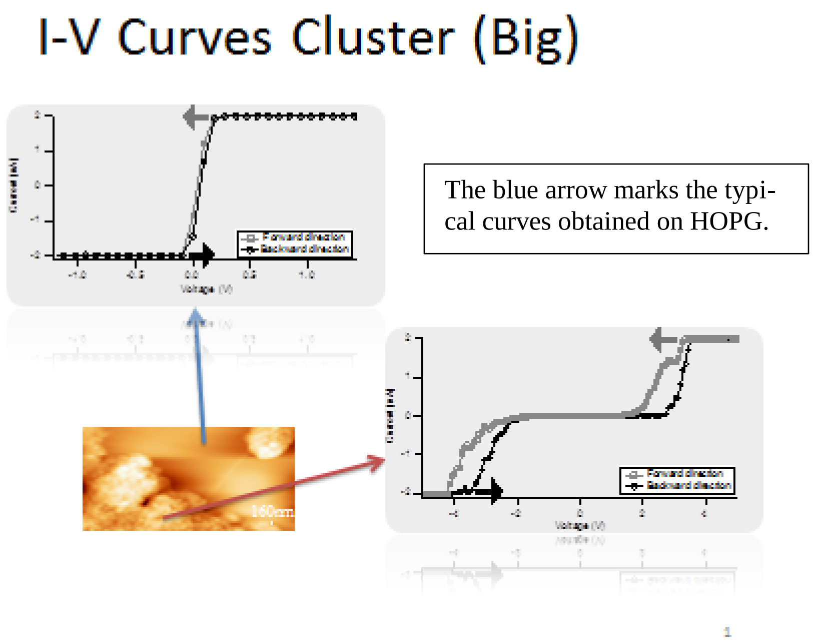

I-V Curves Cluster (Big)

The blue arrow marks the typical curves obtained on HOPG.

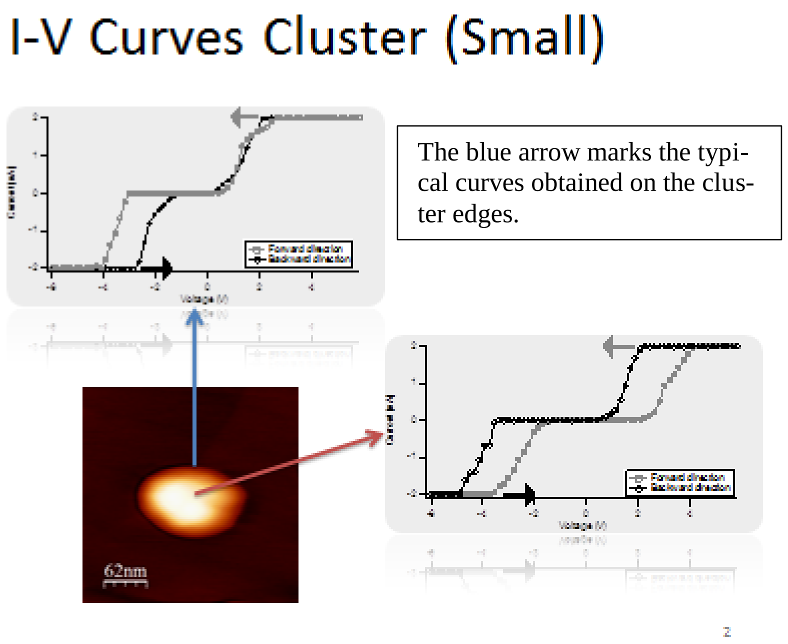

I-V Curves Cluster (Small)

The blue arrow marks the typical curves obtained on the cluster edges.

I-V Curves Single Particle

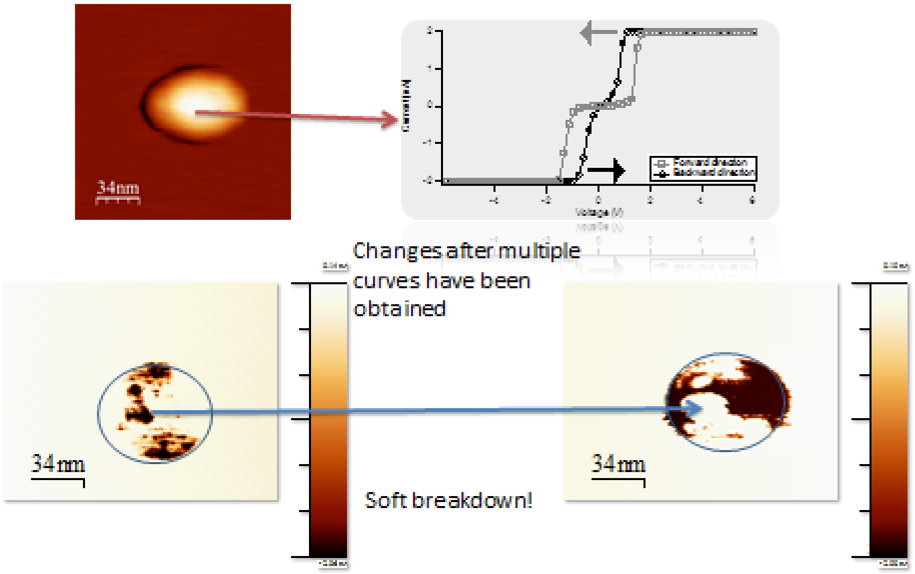

Changes after multiple curves have been obtained

Soft breakdown!

List Of Figures

Acknowledgements

I want to express my outmost gratitude to Prof. Dr. G. Reiss for the support and supervision.

Another great amount of gratitude I owe to Prof. Dr. A. Hütten for always having an open ear and for the supply with cobalt nanoparticles.

The support by Dr. K. Rott and the discussions had a great influence on my work and guided me through the last years. He also provided the SEM images in this work.

I also want to thank Dr. J. Schmalhorst for his critical mind and for the AES measurements (and a lot of good football games),

Prof. Dr. P. Müller (AFM and STM investigations) and Prof. Dr. Th. Glaser (for providing the SMMs) of the Forschergruppe for the cooperation,

PD Dr. A. Thomas for fruitful discussions concerning programming,

(now M. Sc.) J. P. Grote for the AGM measurements and the great cooperation while exploring the magnetic properties of the CoAu multilayer,

(now Dr.) M. Peter for developing uniform and monocrystaline nanoparticles,

N. Mill for the drop casting and cooking of nanoparticles and great support concerning chemical questions,

Dipl. Phys. M. Enzelberger for the AFM measurements in Erlangen and a lot of beer,

(now Dr.) J. Münchenberger for the great atmosphere and discussions in the office,

Dipl. Phys. S. Fabretti for discussions and tea,

Dipl. Phys. P. Hedwig for the long discussions about electronics, Linux, God and the world - the funny TI-Days, coffee breaks and teaching me some new things and views.

The rest of the D2 group for a good working atmosphere!

Finally I want to thank God that I was able to do this work and my family (especially my parents) and church for the great deal of support and prayers.